UC Berkeley
UC Berkeley Electronic Theses and Dissertations

Title

The Solvation Structure, Transport Properties and Reduction Behavior of Lithium-Ion Battery Electrolytes

Permalink

https://escholarship.org/uc/item/8c69j0p7

Author

Hou, Tingzheng

Publication Date

2021

Peer reviewed|Thesis/dissertation

The Solvation Structure, Transport Properties and Reduction Behavior of Lithium-Ion
Battery Electrolytes

by

Tingzheng Hou

A dissertation submitted in partial satisfaction of the

requirements for the degree of

Doctor of Philosophy

in

Engineering – Materials Science and Engineering

in the

Graduate Division

of the

University of California, Berkeley

Committee in charge:

Professor Kristin A. Persson, Chair
Professor Bryan D. McCloskey
Professor Mark Asta

Fall 2021

The Solvation Structure, Transport Properties and Reduction Behavior of Lithium-Ion
Battery Electrolytes

Abstract

The Solvation Structure, Transport Properties and Reduction Behavior of Lithium-Ion Battery Electrolytes

by

Tingzheng Hou

Doctor of Philosophy in Engineering – Materials Science and Engineering

University of California, Berkeley

Professor Kristin A. Persson, Chair

Novel cathode materials and anode materials emerge as promising candidates for realizing next-generation energy storage. Along with the innovation of electrode materials, electrolytes that enable Li^+ transport between electrodes during charge and discharge require to be redesigned as well. This is particularly important because the as-formed electrode-electrolyte interphase (SEI) is found crucial for the full cell operation. In Chapter 1, the components of conventional electrolytes and the formation mechanism of the SEI are briefly introduced. Moreover, some of the promising anode systems, i.e., Si anode and Li metal anode, are reviewed. Finally, approaches to stabilize the interphase of the anodes using novel liquid electrolytes and solid-state electrolytes (SSEs) are thoroughly discussed.

In order to obtain a fundamental understanding of the solvation structure, transport properties, and reduction behavior of electrolyte systems of LIBs, modeling and simulation techniques including classical molecular dynamics (MD) and quantum chemistry calculations are widely utilized. In Chapter 2, the related theory and methods for building a consistent theoretical framework for evaluating both commercial and novel battery electrolytes are introduced. First, the procedures for modeling an electrolyte system using molecular dynamics are thoroughly discussed based on Frenkel and Smit. Second, the analytical equations to obtain transport properties from molecular dynamics trajectories are derived. Finally, the methodologies of calculating reduction and solvation properties from quantum chemical calculations are briefly introduced.

Fluoroethylene carbonate (FEC) has been proposed as an effective electrolyte additive that enhances the stability and elasticity of the SEI. However, uncertainties still remain on the exact mechanism through which FEC alters the electrolyte decomposition and SEI formation process. In Chapter 3, the influence of FEC on a $LiPF_6$/ethylene carbonate (EC) electrolyte is investigated through classical MD, Fourier-transform infrared spectroscopy, and quantum chemical calculations. FEC is found to significantly modify the solvation structure and

reduction behavior of the electrolyte while being innocuous to transport properties. Even with limited 10% of FEC, the Li^+ solvation structure exhibits a notably higher contact-ion pair ratio than the parent EC electrolyte. Moreover, FEC itself, as a new fluorine-containing species, appears in 1/5 of the Li^+ solvation shells. The Li^+-coordinated FEC is found to reduce prior to EC and uncoordinated FEC which will passivate the anode surface at an early onset by forming LiF. The critical role of FEC in tailoring the Li^+ solvation structure and as-formed protective SEI composition provides mechanistic insight that will aid in the rational design of novel electrolytes.

Despite the extensive employment of binary/ternary mixed-carbonate electrolytes (MCEs) for Li-ion batteries, the role of each ingredient with regards to the solvation structure, transport properties, and reduction behavior is not fully understood. In Chapter 4, the Gen2 (1.2 M $LiPF_6$ in EC and ethyl methyl carbonate (EMC)) and EC-base (1.2 M $LiPF_6$ in EC) electrolytes, as well as their mixtures with 10 mol% FEC, are investigated by atomistic modeling and transport property measurements. Due to the mixing of cyclic and linear carbonates, the Gen2 electrolyte is found to have a 60% lower ion dissociation rate and a 44% faster Li^+ self-diffusion rate than the EC-base electrolyte, while the total ionic conductivities are similar. Moreover, we propose for the first time the anion–solvent exchange mechanism in MCEs with identified energetic and electrostatic origins. For electrolytes with additive, up to 25% FEC coordinates with Li^+, which exhibits a preferential reduction that helps passivate the anode and facilitates an improved SEI. The work provides a coherent computational framework for evaluating mixed electrolyte systems.

The novel intrinsically anionic Metal–Organic Frameworks (MOFs) with a superior ionic conduction performance has opened up a new possibility for the development of SSEs. Given the numerous materials space with almost unlimited possibilities of MOFs, it is important to develop a theoretical method that can predict the transport properties of SSEs based on MOFs. In Chapter 5, classical molecular dynamics, grand canonical Monte Carlo, and quantum chemistry are utilized to model the diffusion and ionic conduction phenomena of a novel MOF-688 material and its derivatives. The main ionic conduction mechanism is identified as solvent-assisted Li hopping by calculating the ionic conductivity using theories based on different levels of simplification. Moreover, the Li^+ distribution in the SSE is found to be highly correlated to the charge distribution on the POM cluster. A hypothetical non-interpenetrated MOF-688 derivative is proposed with improved ionic conduction performance, providing insights into the design rules of the novel type of SSEs.

To my family

Contents

List of Figures

List of Tables

Acknowledgments

First and foremost, I am grateful to my advisor, Professor Kristin Persson, for all her generous support and guidance. There were several times that I felt extremely frustrated during my Ph.D. life, for not making progress, for interpersonal conflicts, for the social isolation during the pandemic, and for the high pressure before major deadlines. I couldn't make it through without her kind understanding and helpful instructions. During the past five years from September 7, 2016 when I joined the Persson group, I learned a lot from her broad experience and meticulous attitude in materials modeling. She is a role model that lets me know what a great scientist should look like, and encourages me to pursue a possible future career as a scientific researcher.

I would like to thank my Dissertation Committee members, Professor Mark Asta and Professor Bryan McCloskey. I especially thank Professor Mark Asta for teaching me the basics of molecular dynamics simulations in the course MSE215.

I would like to thank my collaborators, Wentao Xu (许文韬), Dr. Guang Yang (杨光), Dr. Shuren Lin (林樹人), Dr. Jagjit Nanda, Professor Jie Yao, and Professor Omar Yaghi. They offered me full support from the experimental side that help complement my Ph.D. research.

I would like to thank every Persson group member. I especially thank Kara Fong, a great young scholar, for helping me implement theoretical calculations and for teaching me a lot of best practices in data processing and presenting scientific results. I would like to thank Dr. Julian Self, Eric Sivonxay, Dr. Rachel Woods-Robinson, Dr. Rebecca Stern, who entered the Persson group in the same year. Thank you for all the help, and thank you for fighting together! I would like to thank Dr. Nav Nidhi Rajput, for mentoring me during the first year of my Ph.D. I would like to thank Dr. Miao Liu (刘淼) for the generous advice and help during his time in the Persson group and throughout the years. I would like to thank Dr. Ryan Kingsbury, Dr. Matthew Horton, Dr. Shyam Dwaraknath, Dr. Brandon Wood, Dr. Sang-Won Park, Dr. Xiaohui Qu, Dr. Trevor Seguin, Dr. Samuel Blau, Dr. Mingjian Wen, Dr. Jimmy Shen, Dr. Joseph Montoya, and Dr. Jianli Cheng for the generous help.

I would like to thank my former advisor Professor Qiang Zhang (张强) at Tsinghua University for his continued help. I would like to thank my friends and also study partners at Berkeley, Dr. Jingyang Wang (王景阳), Dr. Zhengyan Lun (伦正言), Mengyu Gao (高梦雨), and Shouping Chen (陈寿平).

I would also like to thank my love, Lu (蒋璐), for all her support during my Ph.D. She has reminded me to practice self-care and maintain a healthy work-life balance. She is also a good partner in study and research. I am truly grateful to have met her here at Berkeley and to have her in my life.

Finally, I would like to thank my parents, Jinfeng Hou (侯进峰) and Jiying Shi (史继英). They made me what I am today with their infinite love and full financial support. They taught me how to be a good son, a good student, and a good man. Thank you, mom and dad!

Funding and Computational Resources Statement

Copyright Notice for Previously Published/Co-Authored Work

Chapter 1

Introduction

High capacity energy storage technology holds a decisive position in fulfilling the ever-increasing demands of portable electronic devices, electric vehicles, and smart grids for intermittent solar or wind power [1]. Conventional lithium-ion batteries (LIBs) with a composition of $LiCoO_2$/graphite, which has a theoretical energy density of 360 Wh kg^{-1}, cannot fully satisfy this requirement. To further increase the energy density, novel cathode materials (e.g., Cation-disordered rocksalt-type cathode materials [2, 3], sulfur/carbon composite cathode [4]) and anode materials (e.g., silicon anode [5], Li metal anode [6]) emerge as promising candidates for realizing next-generation energy storage. Along with the innovation of electrode materials, electrolytes that enable Li^+ transport between electrodes during charge and discharge require to be redesigned as well. This is particularly important because the as-formed electrode-electrolyte interphase is found crucial for the full cell operation. Therefore, the actual performance of an electrode material is largely dependent on the composition and intrinsic properties of the associated electrolyte. In this chapter, the components of conventional electrolytes and the formation mechanism of the electrode-electrolyte interphase are briefly introduced. Moreover, some of the promising anode systems, i.e., Si anode and Li metal anode, are reviewed. Finally, approaches to stabilize the interphase of the anodes using novel liquid electrolytes and solid-state electrolytes are thoroughly discussed.

1.1 Liquid electrolytes and the solid electrolyte interphase

The composition of the electrolytes for commercialized LIBs has been well identified [7]. Although the formulation differs between scenarios, the prototype employs a carbonate-based electrolyte with cyclic carbonates (e.g., ethylene carbonate (EC), and propylene carbonate (PC)), linear carbonates (e.g., ethyl methyl carbonate (EMC), diethyl carbonate (DEC), and dimethyl carbonate (DMC)) and lithium salts (e.g., $LiBF_4$, $LiPF_6$, and lithium bis(trifluoromethanesulfonyl)imide (LiTFSI)), as shown in Table 1.1 and Table 1.2. The cyclic carbonates with a high dielectric constant possess higher relative solvating ability [8].

Table 1.1 Common carbonate solvents.
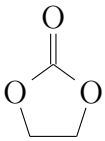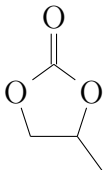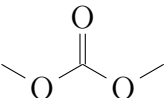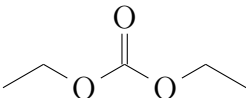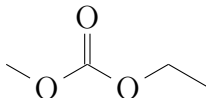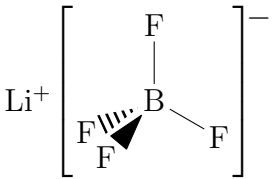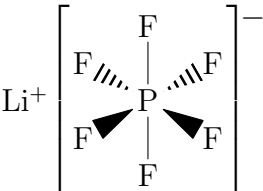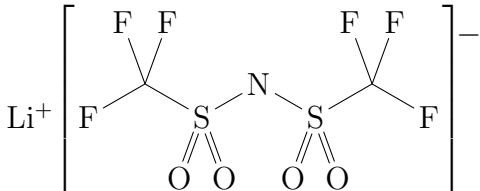
Cyclic carbonates		Linear carbonates		
EC	PC	DMC	DEC	EMC
High dielectric constant		Low viscosity Low melting point		

Table 1.2 Common salts.

LiBF$_4$	LiPF$_6$	LiTFSI
Electrochemical stability Ability to dissolve and dissociate		

The lithium salt cations and anions dissociate, fully or partially, and are solvated by the solvent molecules, which enables Li$^+$ transport. The linear carbonates serve to mitigate the viscosity and lower the melting point. Moreover, the reduction reactions of electrolytes crucially lead to the spontaneous formation of an electrically insulating and ionically conductive SEI between anode and electrolyte in the initial cycles [9]. Hence, the key descriptors for electrolyte performance lie in three major categories: the solvation behavior, the transport properties, and the electrochemical reduction/oxidation behavior.

To realize next-generation energy storage systems, there is a pressing need for functional, optimized electrolytes with excellent bulk stability and conductivity while exhibiting a suitable range of passivating reactions towards the chosen anode material [10, 11]. Mounting evidence points to the rational design of the bulk electrolyte solvation structure [12], including both majority as well as minority species, as a vehicle towards tailoring specific interfacial reactivity and reduction potentials of electrolyte components, which in turn contribute to the formation of a functional solid electrolyte interphase (SEI) layer.

An optimal SEI layer passivates the anode surface against further side reactions while facilitating Li-ion transport [13, 14]. Extensive previous work shows that a complicated

cascade of reduction reactions occurs during the first cycle, and that the initially formed SEI containing inorganic species, e.g. LiF and Li_2CO_3 [15, 16], as well as organic ones, e.g. lithium ethylene dicarbonates (LEDC) [17, 18], further evolves through a variety of aging processes [19–21] (hydrolysis, reaction between Li salt and intermediate decomposition products, and thermal decomposition, etc.) as well as continuous electrolyte reduction [22, 23]. The sequence of reactions and their aging depend both on the specific components and concentration, including additives and impurities, of the bulk electrolyte, and upon the specific anode material and its surface chemistry and structure. Hence, in principle, every anode material requires a differently tailored electrolyte, to achieve maximal compatibility—both electrochemically as well as mechanically.

1.2 Anode materials

Graphite-based materials have been constantly used as the anode active material for LIBs [24, 25]. With its high practical specific capacity of around 350 mAh/g (theoretical capacity of 372 mAh/g) and low and flat working potential (between 250 and 50 mV vs Li^+/Li), it is still by far the most commonly used commercial anode material for LIBs [24]. As shown in Figure 1.1, for graphite anode SEI, it is generally accepted that $LiPF_6$ precipitates in the form of LiF or Li_xPF_y after reduction. Carbonates from the electrolyte solvent precipitate with lithium ions in form of Li_2CO_3, lithium alkyl carbonate ($ROCO_2Li$), or other organic compounds. While LiF, Li_2O, Li_2CO_3, and other insoluble products remain on the graphite surfaces as components of SEI layers, some soluble products from solvent decomposition may diffuse back into the electrolyte. Most reduction processes take place between 0.8 V and 0.2 V vs Li/Li^+ on highly ordered graphite [26].

There is intense interest in developing new anode materials that store higher densities of lithium [27]. One of the most promising anode materials for future high energy density LIBs is Si, due to its high theoretical specific capacity (exceeding 4200 mAh g^{-1}) and low cost [5]. However, as shown in Figure 1.2. during the charging and discharging process, the Si anode must suffer large volume change during battery reactions, i.e., up to 280% volume expansion (increase) from Si to $Li_{15}Si_4$, compared with 13.2% volume expansion from C_6 to LiC_6 [28]. Conventional LIB electrolytes, such as $LiPF_6$ in cyclic EC and linear DMC and/or DEC [7, 29], form a non-passivating Si SEI that is unable to mitigate the cracking due to Si's large volume expansion and contraction during cycling. To improve the Si SEI, several approaches [30] have been explored, including nanoengineering (Figure 1.3) [31, 32], use of binders with tailored functionalities [33–35], as well as modified salts and electrolyte additives (Figure 1.4) [36, 37].

Lithium metal is regarded as another promising anode to further increase the energy density of batteries because of its high theoretical specific capacity (3860 mAh g^{-1}) and low reduction potential (-3.04 V vs. standard hydrogen electrode) [6]. However, uncontrollable lithium deposition during plating/stripping, generally emerging as dendritic and mossy lithium, induces cell failure and even thermal runaway causing fire/explosion events,
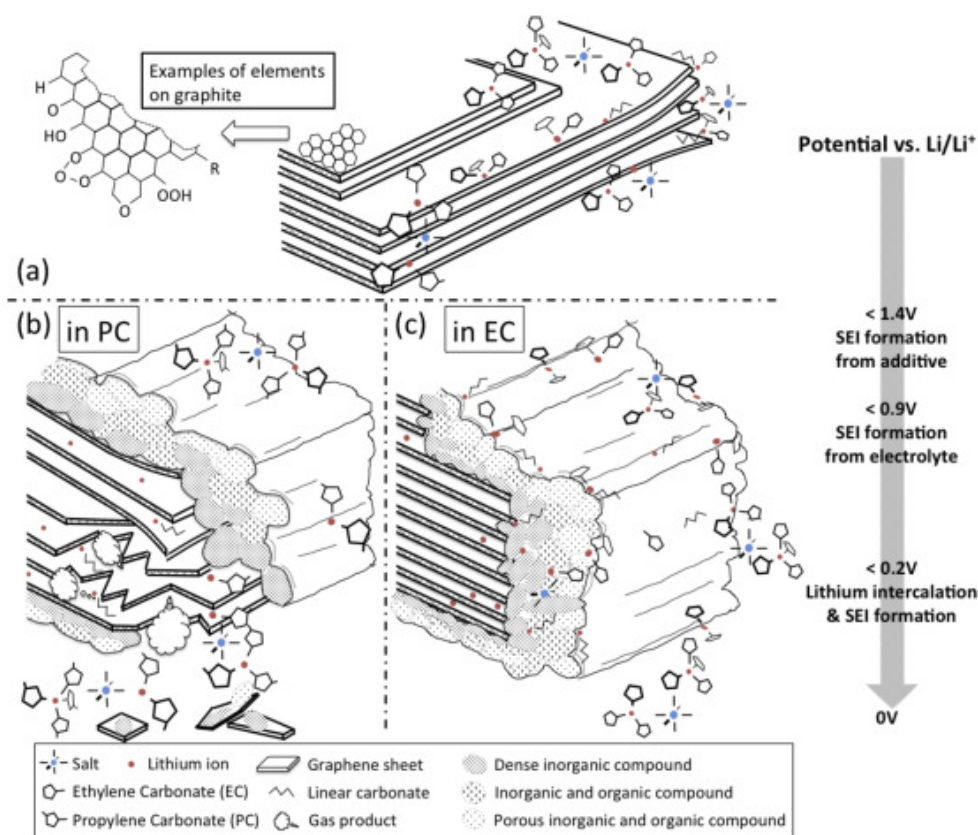
Figure 1.1 Schematic of the anode SEI formation process showing (a) graphene layers surrounded by electrolyte salts and solvents above 1.4 V vs. Li/Li$^+$, (b) propylene-carbonate (PC) intercalation with lithium ions into graphene layers resulting exfoliations below 0.9 V vs. Li/Li$^+$ and (c) stable SEI formation in EC-based electrolyte below 0.9 V vs. Li/Li$^+$; plane side with thinner SEI and edge side with thicker SEI. Copyright 2016 Elsevier, under the terms of the Creative Commons CC-BY license http://creativecommons.org/licenses/by/4.0/.

which plagues the utility of lithium metal anodes in practical applications [39]. Li dendrites are generally induced by inhomogeneous distributions of space charge, current density on the anode surface, and the crack of SEI. Much effort has been devoted to preventing the Li dendrite growth in a working battery [40]. Among these strategies, in situ formation of SEI with high uniformity and stability is one of the most effective and convenient routes due to its prominent impact and low cost, particularly in the industrial manufacture of batteries [29]. Many electrolyte modification approaches are employed to facilitate the in situ formation of a stable SEI layer, such as metal cation additives (Cs$^+$ and Rb$^+$) [41], fluoroethylene carbonate (FEC) additive [42], and highly concentrated electrolyte [43].

For both Si and Li metal anodes, FEC has been spotlighted as an effective electrolyte additive that significantly enhances the stability and elasticity of the as-formed SEI film [44].
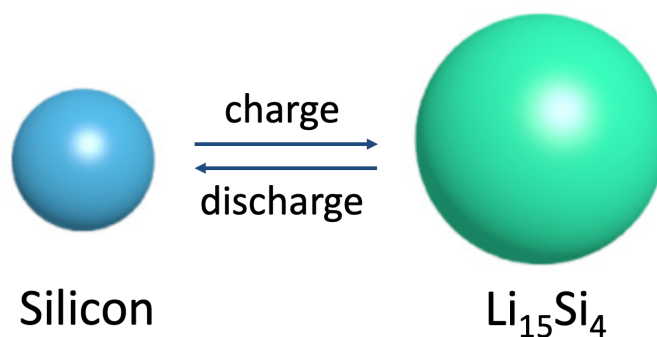
Figure 1.2 An illustration of the volume expansion during the charge and discharge process of Si anodes.

In the presence of FEC, which degrades at a higher reduction potential than both EC and DEC, a denser, more uniform, and conformal SEI is formed on both silicon anode and lithium metal anode [30, 42]. This SEI layer has been found to ameliorate the emergence of large cracks and suppress further decomposition of EC/DMC, leading to enhanced electrochemical performance, improved Coulombic efficiency, and uniform surface morphology of the anode. However, the exact mechanism through which additives alter the electrolyte decomposition and SEI formation process remains unclear. The detailed influence of the FEC additive on tailoring the bulk electrolyte properties and full cell electrolyte performance is discussed in Chapter 3 and Chapter 4.

1.3   The solid-state electrolyte

As mentioned in the previous section, the Li metal anode by definition has the highest theoretical energy density among any other anode materials of LIBs. However, the electronic and ionic conductive Li dendrite can penetrate the porous separator and make direct contact with the cathode, leading to the internal short circuit of the batteries [45]. Moreover, uneven precipitation of active materials will lead to their losing contact with the anode, forming electrochemically "dead" Li and causing permanent capacity loss. Even though novel electrolyte additives, such as FEC, can provide an improved cycling performance, potential risks of thermal runaway still exist, hindering the practical applications of lithium metal anodes. To seek a permanent solution to the challenge, one straightforward approach is substituting the conventional separator and liquid electrolyte design with high-mechanical-strength and dense solid-state electrolytes (SSEs). SSEs mainly fall into three categories: inorganic solid electrolytes, polymer solid electrolytes, and composite SSEs.

Among the recent advances of inorganic solid electrolytes, predominant types of materials include garnet-type SSE ($Li_7La_3Zr_2O_{12}$, LLZO) and its analogues, $Li_7P_3S_{11}$ (LPS) [46], and $Li_{1.4}Al_{0.4}Ti_{1.6}(PO_4)_3$ (LATP) [47]. Inorganic SSEs exhibit satisfactory ionic con-
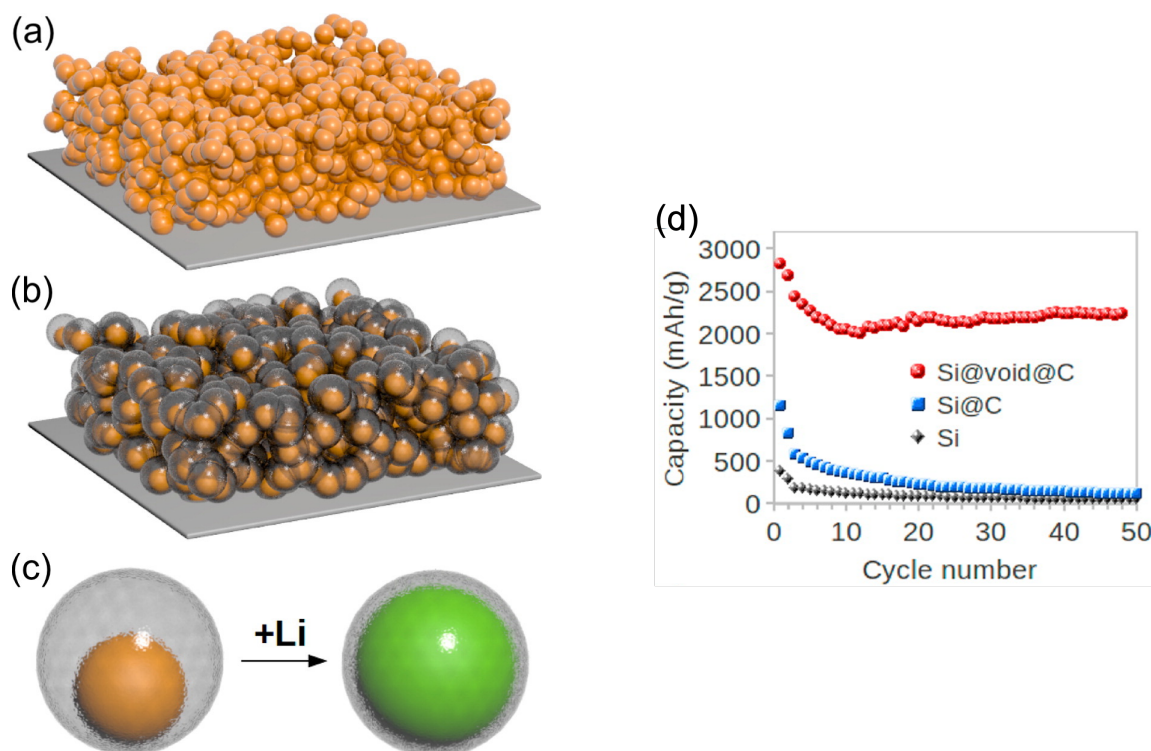
Figure 1.3 Schematic of the materials design and electrochemical cycling performance of a Yolk-Shell Nano-engineering Design for Si anode. (a) A conventional slurry coated SiNP electrode. SEI on the surface of the SiNPs ruptures and reforms upon each SiNP during cycling, which causes the excessive growth of SEI and failure of the battery. The expansion of each SiNP also disrupts the microstructure of the electrode. (b) A novel Si@void@C electrode. The void space between each SiNP and the carbon coating layer allows the Si to expand without rupturing the coating layer, which ensures that a stable and thin SEI layer forms on the outer surface of the carbon. Also, the volume change of the SiNPs is accommodated in the void space and does not change the microstructure of the electrode. (b) A magnified schematic of an individual Si@void@C particle showing that the SiNP expands without breaking the carbon coating or disrupting the SEI layer on the outer surface. (d) Galvanostatic cycling of different silicon nanostructures (PVDF binder). All samples were cycled at C/50 for the first cycle, C/20 for the second cycle, and C/10 for the later cycles. Adapted with permission from ref [38]. Copyright 2012 American Chemical Society.
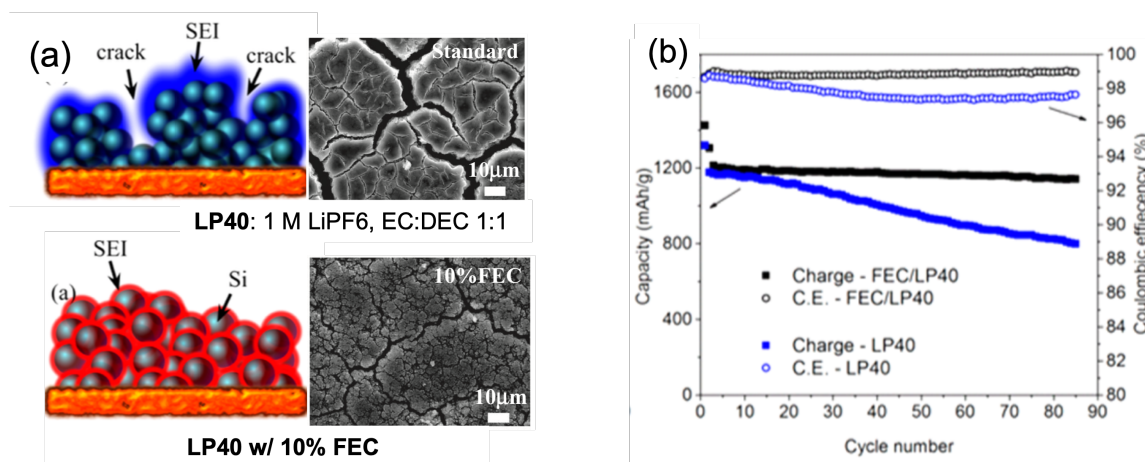
Figure 1.4 (a) Schematic representation and SEM images of SEI formation on a silicon anode which is long-time cycled with different electrolytes FEC/LP40 (a) and LP40 (b). The two SEI layers are different in composition and are highlighted with different colors. (b) Gravimetric capacities and Coulombic efficiencies of the Si/Li0 half-cells cycled between 0.12 and 0.9 V at 500 mA/g (Si) using FEC/LP40 (black) and LP40 (blue) electrolytes. The schematic representation and cycling performance adapted with permission from ref [30]. Copyright 2015 American Chemical Society. The SEM images are adapted from ref [36]. © The Electrochemical Society. The schematic representation and cycling performance are reproduced by permission of IOP Publishing Ltd. All rights reserved.

ductivity, mechanical properties, and excellent electrochemical stability against Li metal. Notably, some of them have ionic conductivity comparable to or even surpassing that of liquid electrolytes (1-10 mS cm^{-1}) [6]. However, a trade-off exists where high elastic modulus typically leads to poor surface adhesion and high interfacial resistance. To circumvent the challenge, remedy strategies have been explored including engineering an interfacial layer between lithium metal and SSEs [48], and surface treatment of SSE to reduce interfacial resistance and increase lithiophilicity [49].

Polymer solid electrolytes based on lithium salts in polymer matrices exhibit favorable interfacial contact with Li metal and low cost [45]. Nonetheless, the performance of polymer solid electrolytes is limited by low ionic conductivity [6], low lithium ion transference number [51], and unsatisfactory elastic modulus [52] compared with inorganic crystalline electrolytes. Continuous efforts have been made to further improve their mechanical/electrochemical stability and ionic conductivity, e.g., introducing mechanical reinforcement blocks [53], incorporating single-ion conductors that replace lithium salts [54], and double layer designs that balance the performance metrics [55, 56]. Recently, several composite SSE designs have been proposed that combine ceramic nanoparticles/nanowires with the polymer [57–60]. Zhao et al. [50] developed an anion-immobilized solid-state composite electrolyte (PLL) synthesized by a Garnet-type Al-doped $Li_{6.75}La_3Zr_{1.75}Ta_{0.25}O_{12}$, polyethylene oxide (PEO), and LiTFSI,
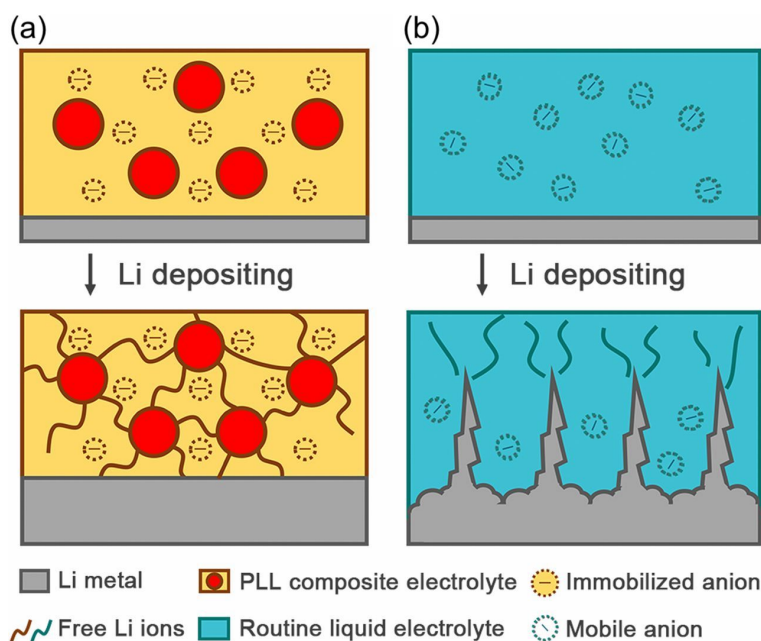
Figure 1.5 Schematic of the electrochemical deposition behavior of the Li metal anode with (a) the PLL solid electrolyte with immobilized anions and (b) the routine liquid electrolyte with mobile anions. Adapted with permission from ref [50]. Copyright 2017 National Academy of Sciences.

where $TFSI^-$ anions are effectively immobilized due to their interactions with ceramic particles and polymer matrix (Figure 1.5). As a result, a high transference number, low polarization, and uniform ion distribution are achieved. Nevertheless, even with improved Li dendrite suppression, interfacial adhesion, and transference number, the reported ionic conductivity of composite SSEs is still one to two orders of magnitude lower than that of liquids, which is insufficient to fulfill the demand for high energy density and high charging rate batteries. Alternatively, adding organic solvents into the solid polymer matrices is considered as a practical workaround to increase the ionic conductivity [61]. However, typical organic solvents (e.g., EC) that exhibit superior salt solvating ability will also lead to the solvation, swelling, or even dissolution of the polymer, which deprive its mechanical strength as a solid electrolyte.

Metal–organic frameworks (MOFs) and covalent organic frameworks (COFs) have been demonstrated to be promising substitutions of their polymer kindred as SSEs [62]. MOFs are crystalline materials that consist of metal centers connected by organic ligands [63]. The highly connected crystalline structure built from strong chemical bonds facilitates great resistance towards organic solvents. To introduce ionically conducting species into the framework, one approach is to use externally added salt where a certain portion of anions can be immobilized by coordinating with partial positively charged (δ^+) sites on the charge neutral frameworks. For example, Park et al. [64] and Wiers et al. [65] reported SSEs based on
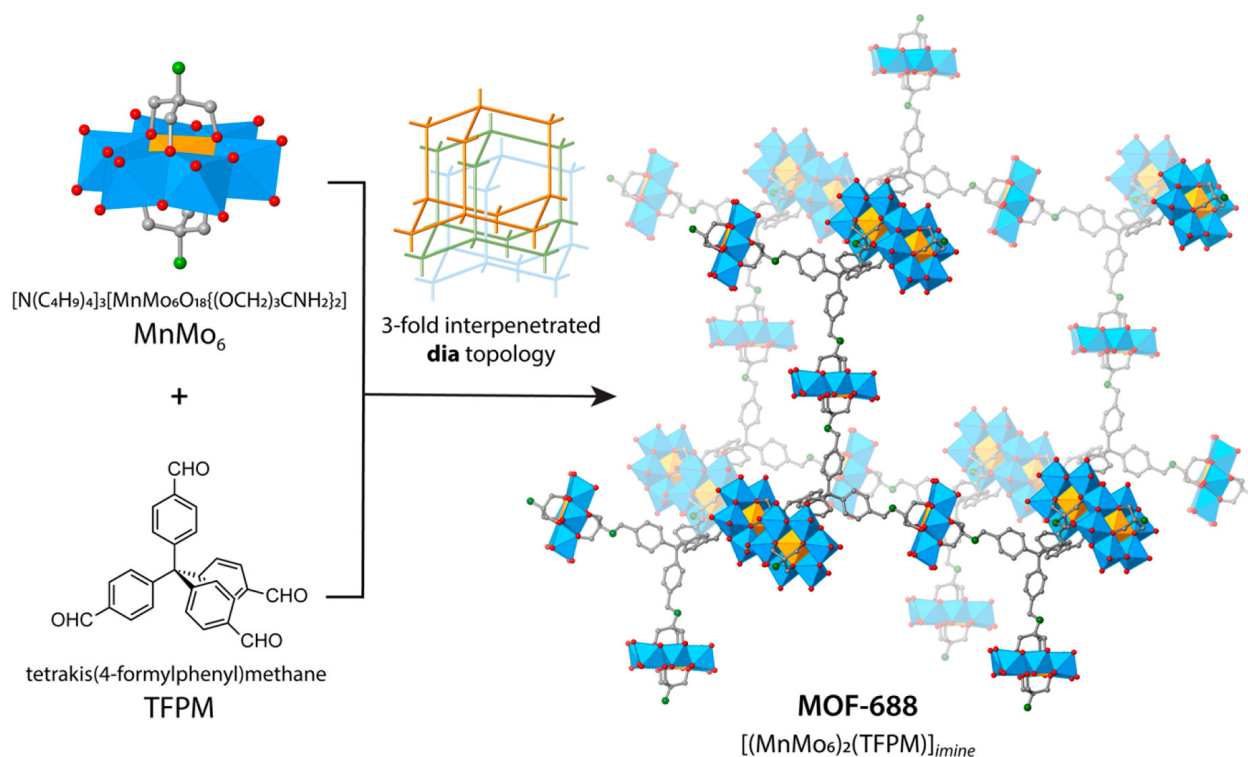
Figure 1.6 Synthetic Strategy and Structure Illustration of MOF-688. Reprinted with permission from ref [61]. Copyright 2019 American Chemical Society.

MOF materials MIT-20 and MOF-74. With the addition of $LiBF_4$ salt and solvents, the ionic conductivity is measured to be 4.8×10^{-4} (298 K) and 3.1×10^{-4} (300 K) mS cm^{-1}, respectively. However, the reported conductivity values may not reflect the intrinsic ionic conduction property of the bulk MOF materials because of the addition of excess liquid electrolyte. A more complicated approach is to construct frameworks by directly linking negatively charged building blocks. Conducting Li^+ can then be introduced as counterions. Therefore, to achieve a satisfactory ionic conduction behavior of Li^+, it is required to deliberately control the charge distribution as well as the total charge carried on the framework. Most recently, Xu et al. [61] synthesized an intrinsically anionic MOF material (MOF-688) by linking ditopic amino functionalized Anderson type polyoxometalate $[N-(C_4H_9)_4]_3[MnMo_6O_{18}(OCH_2)_3CNH_{22}]$ ($MnMo_6$) with 4-connected tetrahedral tetrakis(4-formylphenyl)methane (TFPM) building units through imine condensation (Figure 1.6). The framework has a diamond (**dia**) topology with a 3-fold interpenetrated structure. Each unit of $MnMo_6$ in the polyoxometalate cluster carries three negative charges which are balanced by three tetrabutylammonium (TBA^+) cations which are then exchanged by three Li^+. Using anhydrous PC as a solvent, the material exhibits a high ionic conductivity (4.0×10^{-4} at 298 K), a high lithium ion transference number ($t_{Li^+} = 0.87$), and a low interfacial resistance (353 Ω) against Li metal.

With MOF-688 as a novel and promising prototype SSE, there is a pressing need to understand its structural as well as transport characteristics regulating the Li^+ ionic conduction. The mechanism of how the 3D micropore mesh accommodates the Li^+ ions and solvent molecules that enable ionic conduction remains unclear, necessitating a dynamical analysis of the Li^+ solvation and diffusion mechanism. In Chapter 5, I will investigate the ionic conduction mechanism of the MOF-688 SSE using computational modeling methods. Moreover, possible pathways to improve the performance are also discussed.

Chapter 2

Theory and Simulation Methods for Modeling Electrolytes

In order to obtain a fundamental understanding of the solvation structure, transport properties, and reduction behavior of electrolyte systems of LIBs, modeling and simulation techniques including classical molecular dynamics (MD), ab initio molecular dynamics (AIMD), and quantum chemistry calculations are widely utilized. The typical simulation time in AIMD simulations (< 1 ns) is less than the residence time of a common lithium-anion/solvent pair [66, 67], and hence it may not capture the equilibrium state. Therefore, in this chapter, I will focus on the theory and methods of classical molecular dynamics and quantum chemistry for building a consistent theoretical framework for evaluating both commercial and novel battery electrolytes. First, the procedures for modeling an electrolyte system using molecular dynamics are thoroughly discussed based on Frenkel and Smit.[1] Second, the analytical equations to obtain transport properties from molecular dynamics trajectories are derived. Finally, the methodologies of calculating reduction and solvation properties from quantum chemical calculations are briefly introduced.

2.1   Molecular dynamics simulations

Molecular Dynamics (MD) simulation is a technique for computing the equilibrium thermodynamic properties and transport properties (in and out of equilibrium) of a classical many-body system. The timescale for traditional MD simulation is typically in a range of nanosecond to microsecond, which is suitable for obtaining the solvation structures and transport properties of electrolyte systems. In this section, an introduction to the fundamental theory and algorithm of the MD simulation for modeling electrolytes is given.

---

[1]Partly excerpted from Understanding Molecular Simulation, Second Edition, Daan Frenkel and Berend Smit, Chapter 3: Monte Carlo Simulations & Chapter 4: Molecular Dynamics Simulations & Chapter 6: Molecular Dynamics in Various Ensembles, Copyright 2002, with permission from Elsevier.

The simplest case: a mincrocanonical ensemble

In a simplest case electrolyte system, a set of N particles is defined. The Newton's equations of motion are numerically solved to update the position and velocity of the particles until the properties of the system no longer change with time. After equilibrium, an additional period of production run is performed to obtain the interested electrolyte properties. If we assume the system cannot exchange energy or particles with its environment, the simulation produces a trajectory that conserves the total energy. In other words, for fixed system energy (E), number of atoms (N), and volume (V), we are sampling a mincrocanonical ensemble (constant N, V, E) [68].

To initialize the simulation, non-overlapping positions and velocities (unified or randomized) are assigned to the N particles in the electrolyte system. The particle positions should be chosen compatible with the structure that we are aiming to simulate. For example, the distance between particles and the relative atomic positions within a molecule should be reasonably initialized so that they are close to the expected values under an equilibrium state. A cubic box (or cell) is typically employed.

Newton's equations of motion

The Newton's equations of motion governing the particle motion can be represented as follows [68]:

$$\frac{\mathrm{d}\mathbf{r}_i}{\mathrm{d}t} = \dot{\mathbf{r}}_i = \mathbf{v}_i = \frac{\mathbf{p}_i}{m_i}, \tag{2.1}$$

$$\frac{\mathrm{d}\mathbf{p}_i}{\mathrm{d}t} = \dot{\mathbf{p}}_i = m_i\dot{\mathbf{v}}_i = m_i\mathbf{a}_i = \mathbf{f}_i = -\frac{\partial}{\partial\mathbf{r}_i}u, \tag{2.2}$$

where $\mathbf{r}_i$, $\mathbf{v}_i$, $\mathbf{p}_i$, $\mathbf{a}_i$, m_i are the position, velocity, momentum, acceleration, and mass of particle i, $\mathbf{f}_i$ is the force applied to particle i, t is time, and u is the total energy. In total, equation 2.1 and 2.2 give 6N different coupled first-order equations describing the time evolution of 6N positions and momenta of the N particles.

Consider a simple pair-wise potential

$$u(\mathbf{r}_1, \mathbf{r}_1, \ldots \mathbf{r}_N) = \frac{1}{2}\sum_{ij} u(|\mathbf{r}_i - \mathbf{r}_j|) = \frac{1}{2}\sum_{ij} u(|\mathbf{r}_{ij}|). \tag{2.3}$$

The force can be expanded to

$$\mathbf{f}_i = -\frac{\partial}{\partial\mathbf{r}_i}u = \sum_{j\neq i}\mathbf{f}_{ij}(|\mathbf{r}_{ij}|), \tag{2.4}$$

where $\mathbf{f}_{ij}$ is the force on particle i due to particle j. The brute force computation of the equation will result in a computational cost of $\mathcal{O}(N^2)$.

Periodic boundary conditions

The periodic boundary conditions (PBCs) are usually employed to model an infinite bulk phase based on the N-particle system [69]. The box containing the N particles that we have initialized is called a primitive cell, and an infinite amount of the identical primitive cells would constitute a periodic lattice. In that case, a particle (i) will in principle interact with all other particles in the infinite periodic system, including the periodic image of its own. In reality, however, because many interatomic or intermolecular interactions will damp rapidly with distance (e.g., the Lennard-Jones potential), it is usually permissible to truncate such interactions beyond a certain cutoff without sacrificing the accuracy of the calculation. Thus, the total cost of the calculation can be limited. In the N-particle example, we use a cutoff at a distance r_c, where r_c is chosen to be less than half the diameter of the periodic box. Therefore, we can always limit the evaluation of intermolecular interactions between particle i and j to the interaction between i and the nearest periodic image of j. For a simple cubic box, the distance in any direction between i and the nearest image of j should always be less than box size/2. A practical method is to divide the simulation cell to multiple sub-cells each with a length of r_c. In that case, at each time step, the computational cost is $\mathcal{O}(N)$ for assigning particles into sub-cells, and the computational cost of computing forces resulted from neighbor particles only in neighboring cells is also $\mathcal{O}(N)$. The actual performance of the algorithm should also be dependent on the ratio of r_c/box size.

For long-range interactions, such as Coulombic and dipolar interactions, the idea of truncation of interactions does not work anymore. In such cases, the interactions with all periodic images should be taken into account explicitly. Common techniques for handling long-range interactions includes Ewald summation and particle-mesh-based techniques, which have computational costs of $\mathcal{O}(N^{\frac{3}{2}})$, $\mathcal{O}(N \ln N)$, respectively [70]. Therefore, a particle-particle/particle-mesh (PPPM) method is selected in this study to compute the Coulombic interactions.

Verlet algorithm

With the initialized velocities and the forces computed from the initialized positions, the velocities and positions can be updated by integrating Newton's equations of motion. Among all the algorithms have been designed to do this, the Verlet algorithm is known as one of the simplest and usually the best algorithm [68].

Starting with Newton's equations of motion, we perform Taylor series expansion of the coordinate of a particle around time t:

$$\mathbf{r}(t + \Delta t) = \mathbf{r}(t) + \dot{\mathbf{r}}(t)\Delta t + \frac{1}{2}\ddot{\mathbf{r}}(t)\Delta t^2 + \frac{1}{6}\dddot{\mathbf{r}}(t)\Delta t^3 + \mathcal{O}(\Delta t^4), \tag{2.5}$$

where $\dot{\mathbf{r}}(t) = \mathbf{v}(t)$, $\ddot{\mathbf{r}}(t) = \mathbf{a}(t) = \frac{\mathbf{f}(t)}{m}$. Then equation 2.5 becomes

$$\mathbf{r}(t + \Delta t) = \mathbf{r}(t) + \mathbf{v}(t)\Delta t + \frac{\mathbf{f}(t)}{2m}\Delta t^2 + \frac{1}{6}\dddot{\mathbf{r}}(t)\Delta t^3 + \mathcal{O}(\Delta t^4). \tag{2.6}$$

Similarly,
$$\mathbf{r}(t - \Delta t) = \mathbf{r}(t) - \mathbf{v}(t)\Delta t + \frac{\mathbf{f}(t)}{2m}\Delta t^2 - \frac{1}{6}\dddot{\mathbf{r}}(t)\Delta t^3 + \mathcal{O}(\Delta t^4). \tag{2.7}$$

Summing equation 2.6 and equation 2.7, we obtain

$$\mathbf{r}(t + \Delta t) + \mathbf{r}(t - \Delta t) = 2\mathbf{r}(t) + \frac{\mathbf{f}(t)}{m}\Delta t^2 + \mathcal{O}(\Delta t^4).$$

which yields:

$$\mathbf{r}(t + \Delta t) \approx 2\mathbf{r}(t) - \mathbf{r}(t - \Delta t) + \frac{\mathbf{f}(t)}{m}\Delta t^2. \tag{2.8}$$

The estimate of the new position contains an error that is of order Δt^4, where Δt is the time step of the MD simulation.

By subtracting equation 2.6 and equation 2.7, we obtain

$$\mathbf{r}(t + \Delta t) - \mathbf{r}(t - \Delta t) = 2\mathbf{v}(t)\Delta t + \mathcal{O}(\Delta t^3),$$

$$\mathbf{v}(t) = \frac{\mathbf{r}(t + \Delta t) - \mathbf{r}(t - \Delta t)}{2\Delta t} + \mathcal{O}(\Delta t^2). \tag{2.9}$$

This expression for the velocity is only accurate to order Δt^2. However, the position of the next time step is uncorrelated to these velocity changes. Therefore, the accuracy to order Δt^2 is acceptable. The updated velocities can be used to compute the kinetic energy of the system.

With the above-derived equations, the Verlet algorithm is simple to implement. It only requires the instantaneous $\mathbf{f}$ and $\mathbf{r}$, and $\mathbf{r}$ of the previous step. It has excellent global stability as a consequence of two features. First, because Newton's equations of motion are time-reversible, the Verlet and Verlet-derived algorithms also satisfy this property. In other words, reversing the velocities of the N particles should result in a trajectory that re-traces itself. In fact, many other algorithms are not time-reversible, even if the simulation is carried out with infinite numerical precision.

The second feature, which is more important, is called area preserving, also known as symplectic in mathematics. It is a subtle feature as a consequence of the equations of motion. For example, if we initialize the trajectory of the N particles on a particular energy hyperplane in phase space, $E = E_0$, the collection of the N particles can be used to define a $6N - 1$ dimensional area of the E hyperplane. If we let the trajectory evolve in time, the area it defines after some time t is expected to remain the same, since the area of the E_0 hyperplane does not change. Otherwise, the system has moved to another hyperplane $E \neq E_0$, and energy is not conserved, i.e., there is an energy drift. It is possible to check the area preserving feature of Verlet and Verlet-derived algorithm by computing a Jacobian of the coordinate and velocity updates for time steps.

Finally, it should be noted that even with a time-reversible algorithm, the actual numerical implementation, strictly speaking, is not truly time-reversible. The finite precision of floating-point arithmetic of computers will result in rounding errors. Therefore, a proper

number of significant figures should be specified. Moreover, when integrating the equations of motion, the length of each time step will also influence the behavior of the system dynamics. A large time step could kill the stability for purely numerical problems. Here, we use a simple harmonic oscillator to estimate a reasonable value of the time step Δt. Imagine two particles forming a harmonic oscillator with a frequency of $\omega = 10^{14}$ s^{-1} (corresponding to a wavenumber of 3333 cm^{-1} in atomic spectroscopy). Let the equilibrium distance between the two particles be r_0. If we suppose that the increment of motion in each step is $\Delta r \sim 0.1 r_0$ so as to be stable, then an appropriate Δt would be on the order of magnitude of $\Delta t \sim \frac{0.1}{\omega} \sim 10^{-15}$ s ~ 1 fs.

Property calculations

After equilibrium, a certain period of production run is performed so that the interested electrolyte properties can be extracted. The simplest quantities among these are the thermodynamic properties of the electrolyte system, such as the temperature T and the pressure P [68].

The temperature can be obtained by computing the average kinetic energy, given by

$$T = \frac{2\langle E_\mathrm{k}\rangle}{3Nk_\mathrm{B}} = \frac{2}{3Nk_\mathrm{B}}\left\langle \sum_{i=1}^{N} \frac{|\mathbf{p}_i|^2}{m_i} \right\rangle, \tag{2.10}$$

where E_k is the kinetic energy, k_B is the Boltzmann constant.

The average pressure P can be obtained by

$$\langle P \rangle = \frac{N}{V}k_B T + \frac{1}{3V}\left\langle \sum_{i<j} \mathbf{f}(\mathbf{r}_{ij}) \cdot \mathbf{r}_{ij} \right\rangle, \tag{2.11}$$

where the first term reflects the kinetic energy contribution if assuming no particle interactions (ideal gas), the second term accounts for the non-ideal particle interactions. It should be noted that this pressure expression is derived for a system at constant N, V, and T, which will be discussed in the following sections.

According to Onsager regression theory, the average regression of microscopic fluctuations in a system will obey the same laws as the corresponding macroscopic irreversible (non-equilibrium) process [71, 72]. Therefore, we can extract transport properties directly from the equilibrium MD trajectory. For example, the self-diffusion coefficients for each species in the MD simulation can be obtained by calculating the slope of the mean square displacement (MSD, $r^2(t)$) over time using the Stokes–Einstein relation [73].

Let's consider the diffusion of particles that are initially concentrated at the origin of our coordination frame

$$c(r, 0) = \delta(r), \tag{2.12}$$

where $c(r, 0)$ is the concentration at distance r with respect to the origin and at time $t = 0$, $\delta(r)$ is the Dirac delta function. The Fick's second law governing the relation between the

concentration and diffusion rate is

$$\frac{\partial c(r,t)}{\partial t} = D\nabla^2 c(r,t), \tag{2.13}$$

where D is the diffusion coefficient. The equation 2.12 and 2.13 yield:

$$c(r,t) = \frac{1}{(4\pi Dt)^{d/2}} \exp\left(-\frac{r^2}{4Dt}\right),$$

where d is the dimensionality of the system. Using the fact that

$$\int \mathrm{d}\mathbf{r}\, c(r,t) \equiv 1,$$

we obtain

$$\int \mathrm{d}\mathbf{r}\, c(r,t) r^2 \equiv \langle r^2(t) \rangle.$$

Multiplying equation 2.13 by r^2 and integrating over all space yields

$$\frac{\partial}{\partial t} \int \mathrm{d}\mathbf{r}\, c(r,t) r^2 = D \int \mathrm{d}\mathbf{r}\, r^2 \nabla^2 c(r,t). \tag{2.14}$$

The left side of the equation is equal to

$$\frac{\partial \langle r^2(t) \rangle}{\partial t}.$$

Therefore,

$$\begin{aligned}
\frac{\partial \langle r^2(t) \rangle}{\partial t} &= D \int \mathrm{d}\mathbf{r}\, r^2 \nabla^2 c(r,t) \\
&= D \int \mathrm{d}\mathbf{r}\, \boldsymbol{\nabla} \cdot (r^2 \boldsymbol{\nabla} c(r,t)) - D \int \mathrm{d}\mathbf{r}\, \boldsymbol{\nabla} r^2 \cdot \boldsymbol{\nabla} c(r,t) \\
&= D \int \mathrm{d}\mathbf{S}\, (r^2 \boldsymbol{\nabla} c(r,t)) - 2D \int \mathrm{d}\mathbf{r}\, \mathbf{r} \cdot \boldsymbol{\nabla} c(r,t) \\
&= 0 - 2D \int \mathrm{d}\mathbf{r}\, (\boldsymbol{\nabla} \cdot \mathbf{r} c(r,t)) + 2D \int \mathrm{d}\mathbf{r} (\boldsymbol{\nabla} \cdot \mathbf{r}) c(r,t) \\
&= 0 + 2dD \int \mathrm{d}\mathbf{r}\, c(r,t) \\
&= 2dD. \tag{2.15}
\end{aligned}$$

Equation 2.15 relates the diffusion coefficient D to the width of the derivative of the mean square displacement over which the particles have moved in a time interval t. The equilibrium diffusion of particles in the MD simulation follows the exact same rule as this irreversible

process. Hence, for every particle i, we measure the distance traveled in time t, $\Delta \mathbf{r}_i(t)^2$, and we plot the mean square of these distances as a function of time t [51]:

$$\langle r^2(t) \rangle = \frac{1}{N} \sum_{i=1}^{N} \Delta \mathbf{r}_i(t)^2 \approx \frac{1}{t_s - t + 1} \sum_{t_0=0}^{t_s-t} \frac{1}{N} \sum_{i=1}^{N} \left| \mathbf{r}_i(t) - \mathbf{r}_i(0) - [\mathbf{r}_{cm}(t) - \mathbf{r}_{cm}(0)] \right|^2, \quad (2.16)$$

where the angular brackets denote the average of the squared displacement over all particles and over all time origins, t_s is the number of time steps in the simulation, and t_0 are the different time origins, $\mathbf{r}_i(t)$ is the position vector of species i at time t, and $\mathbf{r}_{cm}(t)$ is the position of the center of mass of the entire system, which we include to correct for any drift in the center of mass of the simulation box. Thus, for a 3D system, the slope of the linear regime in the MSD is then calculated to obtain:

$$D = \frac{1}{6} \lim_{t \to \infty} \frac{\mathrm{d}}{\mathrm{d}t} \langle r^2(t) \rangle. \qquad (2.17)$$

Interestingly, the displacement of interested particles is simply the time integral of the velocity. The relation that expresses the diffusion coefficient directly in terms of the particle velocities is derived as follows [68].

For convenience, we consider only one Cartesian component of the mean-squared displacement, so that

$$2D = \lim_{t \to \infty} \frac{\partial}{\partial t} \langle x^2(t) \rangle. \qquad (2.18)$$

If we write $x(t)$ as the time integral of the x component of the tagged-particle velocity, we obtain

$$\langle x^2(t) \rangle = \left\langle \left(\int_0^t \mathrm{d}t' v_x(t') \right)^2 \right\rangle$$

$$= \int_0^t \int_0^t \mathrm{d}t' \mathrm{d}t'' \langle v_x(t') v_x(t'') \rangle$$

$$= 2 \int_0^t \int_0^{t'} \mathrm{d}t' \mathrm{d}t'' \langle v_x(t') v_x(t'') \rangle, \qquad (2.19)$$

where $\langle v_x(t') v_x(t'') \rangle$ is called the velocity autocorrelation function (VACF), which measures the correlation between the velocity of a particle at times t' and t''. The VACF is an equilibrium property of the system because it describes correlations between velocities at different times along an equilibrium trajectory. As equilibrium properties are invariant under a change of the time origin, the VACF depends only on the difference of t' and t''. Hence,

$$\langle v_x(t') v_x(t'') \rangle = \langle v_x(t - t'') v_x(0) \rangle. \qquad (2.20)$$

Combining equation 2.18, 2.19, 2.20, we obtain

$$2D = \lim_{t \to \infty} 2 \int_0^t \mathrm{d}t'' \langle v_x(t - t'') v_x(0) \rangle,$$

$$D = \int_0^\tau \mathrm{d}\tau \langle v_x(\tau) v_x(0) \rangle. \qquad (2.21)$$

So far, we have shown that the diffusion coefficient D can be also calculated by the integral of the VACF.

Based on the self-diffusion constants, for an electrolyte system with charged particles, the cation ionic transference number t_+ can be calculated from ratios of D according to the following equation if assuming a unit charge on both cations and anions [74]:

$$t_+ = \frac{D_+}{D_+ + D_-}. \tag{2.22}$$

The ionic conductivity can be related to the electrical current autocorrelation function (ECACF) via the following Green–Kubo relation [68]:

$$\sigma = \frac{1}{3k_B TV} \int_0^\infty \langle \mathbf{j}(t) \cdot \mathbf{j}(0) \rangle \mathrm{d}t, \tag{2.23}$$

where the electrical current $\mathbf{j}(t)$ is the electrical current given by

$$\mathbf{j}(t) = \sum_{i=1}^N q_i \mathbf{v}_i(t), \tag{2.24}$$

where $k_B T$ is the thermal energy, V is volume, q_i is the charge of species i, and $\mathbf{v}_i$ is the velocity of species i.

As with the self-diffusivity, the ionic conductivity can also be computed using the following formally equivalent Einstein expression [51]:

$$\sigma = \frac{1}{6k_B TV} \lim_{t \to \infty} \frac{\mathrm{d}}{\mathrm{d}t} \langle \sum_{i=1}^N \sum_{j=1}^N q_i q_j [\mathbf{r}_i(t) - \mathbf{r}_i(t)] \cdot [\mathbf{r}_i(t) - \mathbf{r}_i(t)] \rangle, \tag{2.25}$$

where $\mathbf{r}_i(t)$ is the coordinates of species i at time t. As is the case with diffusion coefficient calculations, a mathematically rigorous analysis of the conductivity requires the term enclosed in the angular brackets of equation 2.25 to be linear in time.

The residence times of ion pairs can be evaluated by computing the lifetime correlation function [75]:

$$P_{\alpha\beta}(t) = \langle H_{\alpha\beta}(t) \cdot H_{\alpha\beta}(0) \rangle, \tag{2.26}$$

where $H_{\alpha\beta}(t)$ is one if particles α and β are neighbors at time t and zero otherwise.

Thermostats

The previous sections introduce the MD simulation performed in a microcanonical ensemble with constant N, V, E, where the simulation only explores $\mathbf{r}_i$ and $\mathbf{p}_i$ in the phase space defined with a fixed total energy. However, a practical electrolyte system is in a phase space hyperplane defined by a fixed temperature rather than a fixed energy. Therefore, for

modeling an electrolyte system, a simulation in the canonical ensemble is often desired. The thermodynamic ensemble probability of the canonical ensemble is defined by [76]

$$\mathcal{P}(\mathbf{p}^N, \mathbf{r}^N) \propto \frac{e^{-\beta H(\mathbf{p}^N, \mathbf{r}^N)}}{Q(T, V, N)}, \tag{2.27}$$

where

$$Q(T, V, N) = \frac{1}{h^{3N} N!} \int e^{-\beta H(\mathbf{p}^N, \mathbf{r}^N)} \mathrm{d}\mathbf{r}^N \mathrm{d}\mathbf{p}^N, \tag{2.28}$$

where h is the Planck constant, β is the thermodynamic beta, defined as $\frac{1}{k_B T}$, $H(\mathbf{p}^N, \mathbf{r}^N)$ is the Hamiltonian of the system.

In order to achieve that, the algorithm should preserve the correct thermodynamics as well as preserve the physical properties that align with the equations of motion. Additional "thermostat" terms are included in the equations of motion to simulate the effect of a heat bath at temperature T. Here, two types of thermostats, Langevin [77] and Nosé–Hoover [78, 79], are briefly introduced.

The Langevin thermostat is most commonly used for implicit-solvent simulations. It includes the solvent viscous effect by modifying equations of motion with the addition of friction (damping) and random noise terms:

$$m_i \ddot{\mathbf{r}}_i = \mathbf{f}_i^c + \mathbf{f}_i^f + \mathbf{f}_i^r, \tag{2.29}$$

where

$$\mathbf{f}_i^c = -\frac{\partial u(\mathbf{r}^N)}{\partial \mathbf{r}_i},$$
$$\mathbf{f}_i^f = \gamma_i m_i \dot{\mathbf{r}}_i,$$
$$\mathbf{f}_i^r = \sqrt{2\gamma_i k_B T m_i} R_{Gauss},$$

where $\mathbf{f}_i^c$ is the conservative force due to a gradient in the potential energy surface, $\mathbf{f}_i^f$ is a frictional force due to the solvent, $\mathbf{f}_i^r$ is a random force due to stochastic collisions with the solvent which balances the viscous force to recover the proper canonical ensemble, γ_i is a friction coefficient, and R_{Gauss} is the probability density function of the Gaussian distribution. For spherical particles of radius a in a medium of viscosity of η,

$$\gamma_i \approx \frac{6\pi a \eta}{m_i}. \tag{2.30}$$

The random force $\mathbf{f}_i^r$ introduces a stochastic component to the numerical trajectories.

Nosé and Hoover developed a deterministic approach that does not involve stochastic changes. The equations of motion are modified with an additional friction force that is proportional to the velocity. A simplified representation of the modified is as follows:

$$m_i \ddot{\mathbf{r}}_i = \mathbf{f}_i^c - m_i \xi \mathbf{v}_i, \tag{2.31}$$

where ξ is a friction coefficient, Q is an effective "mass" associated with the imaginary heat reservoir which reflects how fast the system responds. The Nosé–Hoover thermostat allows one to rigorously generate a canonical ensemble through molecular dynamics with good repeatability, and hence is adopted for modeling the electrolyte systems.

Force field

For modeling an electrolyte system with molecules that both intermolecular (nonbonded) and intramolecular (bonded) interactions, a non-polarizable force field model is usually employed, which is defined by the following potential functions:

$$E_{\text{total}}(r^N) = E_{\text{bonds}} + E_{\text{angles}} + E_{\text{dihedrals}}(+E_{\text{impropers}}) + E_{\text{nonbonded}}, \qquad (2.32)$$

$$E_{\text{bonds}} = \sum_{\text{bonds}} K_r \left(r - r_0 \right)^2, \qquad (2.33)$$

$$E_{\text{angles}} = \sum_{\text{angles}} K_\theta \left(\theta - \theta_0 \right)^2, \qquad (2.34)$$

$$E_{\text{dihedrals}} = \sum_{\text{dihedrals}} V[1 + \cos(n\phi - d)], \qquad (2.35)$$

$$E_{\text{impropers}} = \sum_{\text{impropers}} V[1 + d\cos(n\phi)], \qquad (2.36)$$

$$E_{\text{nonbonded}} = \sum_{i>j} 4\epsilon_{ij} \left[\left(\frac{\sigma_{ij}}{r_{ij}} \right)^{12} - \left(\frac{\sigma_{ij}}{r_{ij}} \right)^6 \right] + \sum_{i>j} \frac{C q_i q_j}{\epsilon r_{ij}}, \qquad (2.37)$$

where combining rules $\epsilon_{ij} = \sqrt{\epsilon_{ii}\epsilon_{jj}}$ and $\sigma_{ij} = \frac{\sigma_{ii}+\sigma_{jj}}{2}$ are used. The bonded interactions (bonds, angles, dihedrals, and impropers) are modeled as harmonic functions and the non-bonded includes van der Waals interactions and Coulombic forces. The dihedral term accounts for the dihedral torsion of four consecutive bonded atoms, whereas the improper term accounts for the dihedral torsion of three atoms centered around a fourth atom.

In this study, unless otherwise indicated, the bonded and non-bonded parameters for liquid electrolyte solvents are obtained from the OPLS-AA force field (Optimized Potentials for Liquid Simulations All Atom) [80, 81]. The OPLS-AA force field is parameterized using input from both quantum chemistry and experimental properties of organic molecules and peptides. As described in the original OPLS-AA force field paper, the torsional parameters (including bonding and angular interactions) in OPLS-AA were determined by fitting to rotational energy profiles obtained from ab initio molecular orbital calculations at the RHF/6-31G*//RHF/6-31G* level for more than 50 organic molecules and ions. The quality of the fits was high with average errors for conformational energies of less than 0.2 kcal/mol and was in good agreement with experimental data. The force-field results for molecular structures are also demonstrated to closely match the ab initio predictions. The nonbonded

parameters were developed in conjunction with Monte Carlo statistical mechanics simulations by computing thermodynamic and structural properties for 34 pure organic liquids including alkanes, alkenes, alcohols, ethers, acetals, thiols, sulfides, disulfides, aldehydes, ketones, and amides. Average errors in comparison with experimental data are 2% for heats of vaporization and densities. Therefore, it is believed that the force field can effectively reproduce the interested properties of electrolyte systems. Further validations of the force field are provided in Appendix B.

2.2 Quantum chemical calculations

Reduction potential

The adiabatic reduction potentials for the representative solvation structures were calculated using the following function [82]:

$$E_{\text{adiabatic}} = -\frac{G_{\text{reduced}} - G_{\text{initial}} + \Delta G^o_{\text{solv}}(\text{reduced}) - \Delta G^o_{\text{solv}}(\text{initial})}{F} - 1.4\text{V}, \qquad (2.38)$$

where G_{reduced} and G_{initial} are the free energies of the reduced and initial complexes at 298.15 K in gas-phase, respectively; ΔG^o_{solv} are the corresponding free energies of solvation with both implicit and explicit solvents considered, and F is the Faraday constant. The zero-point energy (ZPE) corrections were considered in the calculation while the basis set superposition error (BSSE) energy was neglected [83]. A standard-state correction [84] was considered to account for the different concentrations of the non-solvated species, which resulted in the addition of a correction constant $RT \ln \frac{24.47}{M}$ to ΔG^o_{solv}, where R is the gas constant, T is temperature, 24.47 is the molar volume in liter for ideal gas under 1 atm and 298.15 K, and M is the effective concentration of the species that are free of Li solvation. Geometries were allowed to relax after the electron transfer. Subtraction of 1.4V accounts for the conversion from the absolute electrochemical scale to the commonly used Li/Li+ potential scale in order to compare predicted values with experimental data using the same reference electrode. An additional factor of 0.1-0.2 V for graphite intercalation or 0.3–0.4 V for Si anode Li insertion should be subtracted if the reference electrode is changed to these specific systems. The experimental reduction potentials are computed from the full cell differential capacity (dQ/dV) curve [85]. The cells using graphite anodes were reported to be charged to 3.5 V during the formation cycle. This full cell voltage is set to be 0 V with respect to the graphite anode. For example, if the reduction peak is at 3.2 V, then the reduction potential of the reduced species will be 0.3 V (vs graphite) or 0.45 V (vs Li/Li+).

Energy decomposition analysis

The energy decomposition analysis based on absolutely localized molecular orbitals within an implicit solvent model (ALMO-EDA(solv)) [86–88] partitions the total binding energy (E_{B})

of two clusters into contributions from permanent electrostatics (ELEC), Pauli repulsion (PAULI), dispersion (DISP), polarization (POL), and charge transfer (CT):

$$E_{\mathrm{B}}^{(\mathrm{s})} = \Delta E_{\mathrm{ELEC}}^{(\mathrm{s})} + \Delta E_{\mathrm{PAULI}}^{(\mathrm{s})} + \Delta E_{\mathrm{DISP}}^{(\mathrm{s})} + \Delta E_{\mathrm{POL}}^{(\mathrm{s})} + \Delta E_{\mathrm{CT}}^{(\mathrm{s})}, \tag{2.39}$$

where the superscript "(s)" indicates that the energetic terms are calculated with solvent taken into account. The electrostatic term could be further decomposed into

$$E_{\mathrm{ELEC}}^{(\mathrm{s})} = \Delta E_{\mathrm{ELEC}}^{(0)} + \Delta E_{\mathrm{SOL}}^{el}, \tag{2.40}$$

where $\Delta E_{\mathrm{ELEC}}^{(0)}$ term reflects the strength of the Coulomb interaction in vacuum, while $\Delta E_{\mathrm{SOL}}^{el}$ is the correction from solute–solvent electrostatic interaction, which is an unfavorable term as its net effect is to damp the attractive Coulomb interaction between clusters. Again, a standard-state correction term was added to account for the difference between the standard state in quantum chemical calculations ($1/24.47$ mol L^{-1}) to the standard state in solution (1 mol L^{-1}). Therefore, the electrostatic term is calculated by:

$$E_{\mathrm{ELEC}}^{(\mathrm{s})} = \Delta E_{\mathrm{ELEC}}^{(0)} + \Delta E_{\mathrm{SOL}}^{el} + RT \ln \frac{1}{24.47}. \tag{2.41}$$

Chapter 3

The Influence of Electrolyte Additives in Unary Cyclic Carbonate Electrolytes

Fluoroethylene carbonate (FEC) has been proposed as an effective electrolyte additive that enhances the stability and elasticity of the solid electrolyte interphase (SEI) of emerging Si and Li metal anodes. However, uncertainties still remain on the exact mechanism through which FEC alters the electrolyte decomposition and SEI formation process. In this chapter, the influence of FEC on $LiPF_6$/ethylene carbonate (EC) electrolytes for Si anodes is investigated through classical molecular dynamics, Fourier-transform infrared spectroscopy, and quantum chemical calculations. Albeit a minority species, FEC is found to significantly modify the solvation structure and reduction behavior of the electrolyte while being innocuous to transport properties. Even with limited 10% of FEC, the Li^+ solvation structure exhibits a notably higher contact-ion pair ratio (14%) than the parent EC electrolyte (6%). Moreover, FEC itself, as a new fluorine-containing species, appears in 1/5 of the Li^+ solvation shells. The Li^+-coordinated FEC is found to reduce prior to EC and uncoordinated FEC which will passivate the anode surface at an early onset (ca. 0.3 V higher than EC) by forming LiF. The critical role of FEC in tailoring the Li^+ solvation structure and as-formed protective SEI composition provides mechanistic insight that will aid in the rational design of novel electrolytes.

3.1 Introduction

To understand the composition and morphology of the Si SEI formed with FEC, extensive experiments using scanning transmission electron microscopy (STEM) [89], electron energy loss spectroscopy (EELS) [89], Fourier-transform infrared spectroscopy (FTIR) [36, 90], X-ray photoelectron spectroscopy (XPS) [5, 91], atomic force microscopy (AFM) [92, 93], hard X-ray photoelectron spectroscopy (HAXPES) [30, 94], nuclear magnetic resonance (NMR) [5,

95], differential electrochemical mass spectrometry (DEMS) [96], and time-of-flight secondary ion mass spectrometry (ToF-SIMS) [97], etc., have been undertaken. Lucht [36] and co-workers recommended a 10% FEC inclusion based on a combination of low impedance and high capacity retention due to the formation of an SEI which contains both a flexible polymer and high lithium salt content (LiF and Li_2CO_3). Subsequent studies found that, compared with a standard EC/DMC electrolyte, the use of 10% FEC additive modifies the organic SEI components derived from LEDC and soluble linear oligomers to soluble and insoluble crosslinked poly(ethylene oxide)-based polymers (such as lithium poly(vinylene carbonate)), which could better passivate the anode surface and resist volume expansion [5, 95, 98]. Meanwhile, FEC incurs increased formation of LiF, less formation of Li_2CO_3 and organic carbonate species resulting in an overall lower interfacial impedance of the Si anode [99]. The presence of fluoride species further leads to the etching of the native oxide surface layer, improving the surface region Li conductivity and lowering the interfacial resistance [13, 89]. Moreover, there is evidence that FEC influences the $LiPF_6$ decomposition reaction and may suppress further salt degradation after the initial cycles [30].

Numerous studies have endeavored to understand the reaction pathway and SEI formation mechanism through experiments [100] and multiscale computational simulations [101]. For example, experimental efforts have utilized Lithium Naphthalide (LiNap) as a one-electron reduction reagent [102, 103] to analyze the resulting solid precipitates and gas evolution. Through this technique, FEC was found to decompose into a range of products including HCO_2Li, $Li_2C_2O_4$, Li_2CO_3, and polymerized vinylene carbonate (VC), which supports a decomposition mechanism where FEC reduces to form VC and LiF, followed by subsequent VC reduction. Other complementary approaches include theoretical modeling the electrolyte [104], Si anode [105], and their interphase [106, 107]. Quantum chemical calculations confirm that defluorination reactions significantly increase the reduction potential of FEC [108]. Leung and Balbuena, et. al. have pioneered the ab-initio molecular dynamics (AIMD) simulation of EC and FEC on the surface of Si as well as lithiated Si ($LiSi_4$, $LiSi_2$, LiSi, and $Li_{13}Si_4$) [109–112] including the native oxide layer [105, 113], and proposed a series of possible decomposition mechanisms leading to LiF formation and polymerization. FEC is found to exhibit more diverse reaction pathways than the two-electron reduction of unsubstituted ethylene carbonate [26, 114, 115]. Both one- and two-electron reactions are feasible for the FEC reduction and result in a fluoride radical which in both cases contribute to the formation of LiF [112]. Also, it was found that radical species are responsible for the electron transfer that allows SEI layer growth once its thickness has evolved beyond the electron tunneling regime [106, 116, 117]. While several studies have focused on the reduction mechanisms of single FEC [118] and simplified solvation/interface models [112, 119], a thorough examination of the influence of FEC on the solvation structure of the electrolyte [120], and hence the reduction potentials of the associated majority as well as minority species whose populations are altered by FEC, has to our knowledge not been undertaken. For example, it has been widely assumed that FEC, exhibiting a lower donor number than EC, remains largely uncoordinated as an additive in LIB electrolyte formulations [121, 122]. However, even as a minority species, FEC may strongly influence the reduction potential and decom-

position mechanism of associated electrolyte components, and hence alter the onset as well as reaction sequence of the bulk electrolyte. One of the goals of this chapter is to investigate how FEC influences the solvation structure, which further determines the reduction reactions and the subsequent SEI formation process.

In this chapter, classical molecular dynamics (MD) simulations coupled with quantum chemical calculations are performed to describe the detailed solvation structure and reactivity of $LiPF_6$ in EC/FEC, as a function of FEC as well as salt concentration. The solvation structure, self-diffusion coefficient and other macroscopic properties of the EC/$LiPF_6$ electrolyte with or without FEC additive are obtained, and the reduction potentials of the majority as well as minority species are calculated. Spin density analysis was used to further elucidate the reduction behavior of the solvate complexes obtained from the MD simulation, and hence the role of FEC in the SEI formation reaction. Corresponding experimental FTIR measurements are used for validation and as a direct determination of the coordination number in comparison with the calculated solvation structure. This chapter aims to provide a deeper understanding of the subtle influence of the FEC additive on the bulk electrolyte and its constituents to aid in the future rational design of functional electrolytes for Si anodes.

3.2 Computational and experimental details

Classical molecular dynamics (MD)

MD simulations were performed using the Large Scale Atomic/Molecular Massively Parallel Simulator (LAMMPS) [123] code for electrolytes of 1.0/1.2 M $LiPF_6$ in EC or EC with 5/10 mol% FEC. Only EC (and FEC) molecules are considered here to simplify the model. 1,500 solvent molecules were used as bulk electrolytes. The number of salt molecules was adjusted via several test runs for 1 atm and 298 K equilibrium conditions to achieve the 1.0 M and 1.2 M concentrations. Specifically, the final number of salt molecules were 104 and 126 with equilibrated box volumes of 177.5 nm^3 and 180.2 nm^3, respectively. The molecules were initially packed randomly in a cubic box of size $54\times54\times54$ $Å^3$ periodic in the XYZ direction using PACKMOL [124] (Appendix Figure A.1). The initial configuration was minimized by a conjugated-gradient energy minimization scheme employing a convergence criterion of 1.0×10^{-4}. While the thermodynamic melting point for EC with 1M $LiPF_6$ is approximately 298 K [125], the kinetic liquid range limit may be lower [126], which allows a room temperature liquid state simulation. The systems were equilibrated for 2 ns in the isothermal-isobaric ensemble (constant NPT) using the Parrinello–Rahman barostat to maintain a pressure of 1 bar and a temperature of 298 K with a time constant of 1 ps. An annealing process was conducted to further guarantee that all systems are melted and to avoid local configuration confinement. All systems were heated from 298 K to 400 K for 1 ns, and maintained at 400 K for 1 ns, and subsequently annealed from 400 to 298 K in 1 ns. Finally, the production runs of 5 ns were conducted in the canonical ensemble (NVT) under Nosé-Hoover thermostats with a time constant of 1 ps at 298 K. The simulation time was

long enough to sample adequately the Fickian (diffusive) regime of all systems, which was justified by a 55 ns long run (Appendix Figure A.2).

The bonded and non-bonded parameters for EC and FEC were obtained from the Optimized Potentials for Liquid Simulations All Atom (OPLS-AA) force fields [80, 81], the PF_6^- anion from Lopes et al. [127], and the lithium cations from Jensen et al. [128] The partial atomic charges for all molecules were derived by first optimizing the geometry using Becke's three-parameter exchange function combined with the Lee–Yang–Parr correlation functional (B3LYP) [129] at the aug-cc-pvdz theory level using the Gaussian 16 [130] package and then fitting the electrostatic potential surface using the RESP method [131, 132]. Long-range electrostatic interactions were handled by the particle-particle particle-mesh (PPPM) solver with a grid spacing of 0.1 nm. A cutoff distance of 1.5 nm was used for electrostatic and 12–6 Lennard-Jones interactions. Moreover, each Li ion in the system is surrounded by at least one PF_6^- in the first solvation shell or second solvation shell according to the trajectories (Appendix Figure A.3). Hence, if we ignore the negligible amount of aggregates (AGG), all Li ions can be categorized into the contact ion pair (CIP) and solvation separated ion pair (SSIP). A Boltzmann factor was used to estimate the CIP formation free energy from the population difference of the CIP and SSIP structures.

$$\Delta_f G_{CIP} = -k_B T \ln \frac{p(CIP)}{p(SSIP)} \tag{3.1}$$

where p is the population for each species, $\Delta_f G_{CIP}$ is their relative free energy, k_B is the Boltzmann constant and T is the temperature. For NVT run under equilibrated pressure, the Helmholtz free energy (A) is approximately equal to the Gibbs free energy (G).

Quantum chemical calculations

Geometries of solvate complex were optimized from the initial structures observed in MD simulations to obtain their theoretical IR vibrations using Gaussian 16 at the B3LYP/6-31++G(d) level of theory [133]. The calculated IR data was then accumulated according to the composition ratio from the MD simulations to obtain the total spectra of each electrolyte. The adiabatic reduction potentials for the representative solvation structures were calculated with the method described in Chapter 2. A dielectric constant of 90 was adopted for the EC solvent as well as the EC/FEC mixture [134]. The spin density calculation of the reduced state structures was conducted using natural bond orbital (NBO) theory. The dipole moment calculation was conducted at the B3LYP/6-311++G(d,p) level of theory.

Fourier-transform infrared spectroscopy (FTIR)

The FTIR spectra for 1.0 M LiPF$_6$ in EC and 1.0 M LiPF$_6$ in EC with 10 wt% FEC were collected with a FTIR spectrometer (Bruker, ALPHA) using a diamond attenuated total reflection (ATR) accessory. Two pure solutions (EC and EC w/ 10 wt% FEC) were also tested as a comparison. Spectra were collected in the region from 4000 to 650 cm^{-1} with

128 scans and 2 cm^{-1} resolution in an argon-filled glovebox with O2 and H$_2$O < 0.1 ppm. Ethylene carbonate (EC, anhydrous, $\geq$ 99%), lithium hexafluorophosphate (LiPF$_6$, battery grade) and fluoroethylene carbonate (FEC, 99%) were purchased from BASF. All spectra were normalized via the stretching band of –CH$_2$ at 3000 cm^{-1}. This analysis is based upon the assumption that the infrared intensities of the uncoordinated and coordinated structures are equivalent after normalization (no scaling of the bands).

3.3   Solvation Structure

A sequential simulation for 1.0/1.2 M LiPF$_6$ in EC with 0/5/10% FEC was conducted to investigate the influence of FEC on the solvation structure of the LiPF$_6$/EC electrolyte. The population proportion of solvent molecule and anion in the first solvation shell of Li$^+$ is clearly altered after adding FEC, which is confirmed by the radial distribution function, g(r), and the corresponding integrals, N(r), of Li-X (X = O(EC), F(PF$_6^-$), Li, P(PF$_6^-$) for EC and X = O(EC), F(PF$_6^-$), O(FEC), P(PF$_6^-$), F(FEC) for EC w/ FEC) pairs as shown in Figure 3.1, Appendix Figure A.4, and Appendix Table A.1. The dominant peak of the Li-F pair at ca. 8 Å shown in Figure 3.1a suggests that for 1.0 M LiPF$_6$ in EC, most of the LiPF$_6$ salt forms solvent separated ion pairs (SSIP), while the contact ion pairs (CIP) present as minority species (Figure 3.2b). In addition, a trace amount (less than 1%) of aggregate solvates (AGG) were also observed during the simulation. By integrating the g(r) to 3.0 Å, the total coordination number (CN) for Li ion is obtained as shown in Figure 3.2a. Interestingly, while most of the first solvation shell is occupied by EC solvent molecules (5.84 out of 5.90) with a most probable distance of 2.08 Å to Li$^+$, the Li$^+$ solvation sheaths also present an average of 0.06 PF$_6^-$ anions, most of which form monodentate structures coordinated through a fluorine. The simulation produced a longer distance of 2.11 Å for the Li-F pair, illustrating that EC molecules take closer positions in solute complexes. The AGG species are rare, indicating an almost negligible number of Li ions that coordinate with more than one PF$_6^-$ anion. Hence, the corresponding CIP ratio is estimated as 6%, with a SSIP ratio of 94%, which agrees qualitatively with previous MD simulations [135], and is in agreement with common assumptions that LiPF$_6$ is a weakly coordinating salt compared to LiBF$_4$ and well dissociated in EC solutions [136].

Upon addition of 10% FEC into the LiPF$_6$/EC electrolyte, the solvation structure is evidently altered in several ways, primarily due to the weakened donor ability of FEC. Besides the similar solvation structures as shown in Figure 3.2b, other solute complex structures containing FEC were also observed in the snapshots of the MD simulation (Figure 3.2c). Intriguingly, it is the carbonyl O in FEC that binds with the Li ion rather than F, which means that the composition difference of the solvent molecule does not radically alter the binding behavior as compared with the parent EC molecule [122]. However, the average CN for Li-O(EC) pair decreases from 5.84 to 5.51, allowing for an average Li-O(FEC) pair contribution of 0.19 to the first solvation shell. A maximum in g(r) of 2.12 Å was observed for the Li-O(FEC) pair, suggesting a weaker interaction between Li-FEC as compared to
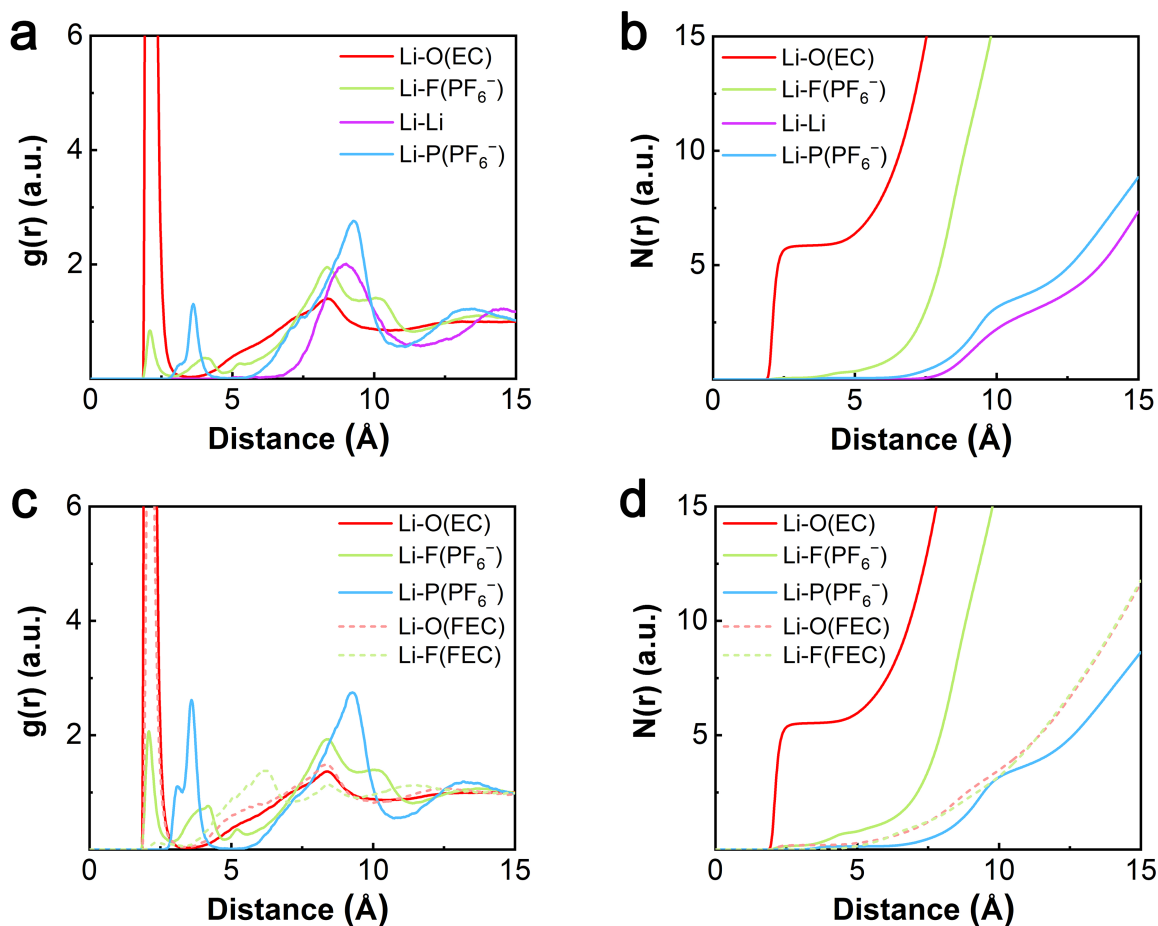
Figure 3.1 Calculated radial distribution functions, g(r), and the corresponding integrals, N(r), of Li-O(EC), Li-F(PF$_6^-$), Li-Li, Li-P(PF$_6^-$) pairs of (a) (b) 1.0 M LiPF$_6$ in EC, and Li-O(EC), Li-F(PF$_6^-$), Li-P(PF$_6^-$), Li-O(FEC), Li-F(FEC) pairs of (c) (d) 1.0 M LiPF$_6$ in EC with 10%mol FEC additive.

Li-EC. Notably, the CIP ratio doubles from 6% to 14%, which significantly changes the statistics of the SEI formation reaction precursors, indicating a prominent role of FEC, even as a minority species. Similar to the EC electrolyte, the simulation with FEC additive results in a same Li-EC distance. Yet, the Li-FEC distance is slightly farther away (2.12 Å) as compared to the Li-EC counterparts, which results in a 'looser' structuring of the first solvation shell. The EC electrolyte are known to promote salt dissociation due to its high dipole moment (5.64 Debye, calculated), as well as a high donor number. In contrast, FEC exhibits a lower dipole moment (4.97 Debye, calculated) which results in less dissociation of LiPF$_6$ and weakened donor ability (i.e. smaller CN of Li$^+$-solvent). This was further illustrated by inspecting the different charge population on the carbonyl oxygen of each molecule. Natural bond orbital analysis results in a charge on O(EC) of −0.66, while the

Table 3.1 The calculated coordination number of Li-X pairs, total coordination number, CIP ratio and corresponding contact ion pair (CIP) formation free energy $\Delta_f G_{CIP}$ of 1.0 M LiPF$_6$ in EC with 0/5/10% FEC and 1.2 M LiPF$_6$ in EC with 0/5/10% FEC.

Electrolyte	Coordination number					CIP ratio	$\Delta_f G_{CIP}$ (kcal/mol)
	O(EC)	O(FEC)	P(PF$_6^-$)	F(PF$_6^-$)	Total		
1.0M	5.84	-	0.06	0.07	5.90	6%	1.63
1.0M w/ 5%FEC	5.69	0.12	0.09	0.09	5.90	9%	1.37
1.0M w/ 10%FEC	5.51	0.19	0.14	0.17	5.85	14%	1.07
1.2M	5.71	-	0.12	0.20	5.84	12%	1.18
1.2M w/ 5%FEC	5.58	0.12	0.18	0.20	5.87	18%	0.90
1.2M w/ 10%FEC	5.41	0.23	0.18	0.23	5.82	18%	0.90

charge on O(FEC) is −0.62, indicating the weaker donor ability of FEC as compared to EC. If we compare all six simulated compositions listed in Figure 3.2a, it is obvious that a higher LiPF$_6$ concentration exhibits a higher CIP ratio. More importantly, when FEC is added to the system, a non-negligible percentage of the solute complexes are modified with fluorine-containing FEC that occupies the first solvation shell. The tendency for CIP formation can be represented by the free energy $\Delta_f G_{CIP}$ which is obtained through the CIP population, assuming a Boltzmann distribution of electrolyte species. Table 3.1 summarizes the results which show that higher salt concentration as well as the inclusion of FEC reduces the energy cost of contact ion pairing. Previous first-principles calculations reported a $\Delta_f G_{CIP}$ of 2.6 kcal mol^{-1} for the Li$^+$-(PC)$_4$ to Li$^+$-PF$_6^-$(PC)$_3$ conversion [137], which is approximately 1 kcal mol^{-1} higher than that of 1.0 M LiPF$_6$/EC obtained here from the CIP population. We speculate that the inclusion of explicit solvation effects beyond the first solvation shell as well as polarization effects not included in the current simulations may contribute to the difference between the two methodologies. In particular, the inclusion of 10% of FEC further reduces the solvating strength of the composite electrolyte, and allows for more CIPs, i.e. for PF$_6^-$ to directly contact/interact with Li$^+$. The coordination number for the Li-FEC pair increases to 0.2, which means that about 20% of the solvate structures on average now contain at least one FEC. We argue that this content change of the solute complex significantly changes the reduction potentials of the electrolyte constituents, which will be addressed further in the following sections. We also note that, with a higher temperature, the total coordination number of Li$^+$ is lower [138]. Therefore, tests of the electrolyte system under a sequential temperature of 330 K, 350 K, 400 K were performed to validate the results (Appendix Table A.2). It was found that, with higher temperature, the CN for Li$^+$-EC decreases from 5.84 (298 K) to 5.23 (400 K), and the population of Li$^+$-PF$_6^-$ CIPs increases from 6% (298 K) to 25% (400 K). This may be explained by the increase in random thermal motion of solvent molecules resulting in a decrease of the dielectric constant and weakened EC-Li (dipole-charge) interactions. Thus, the Li-PF$_6^-$ (charge-charge) interaction
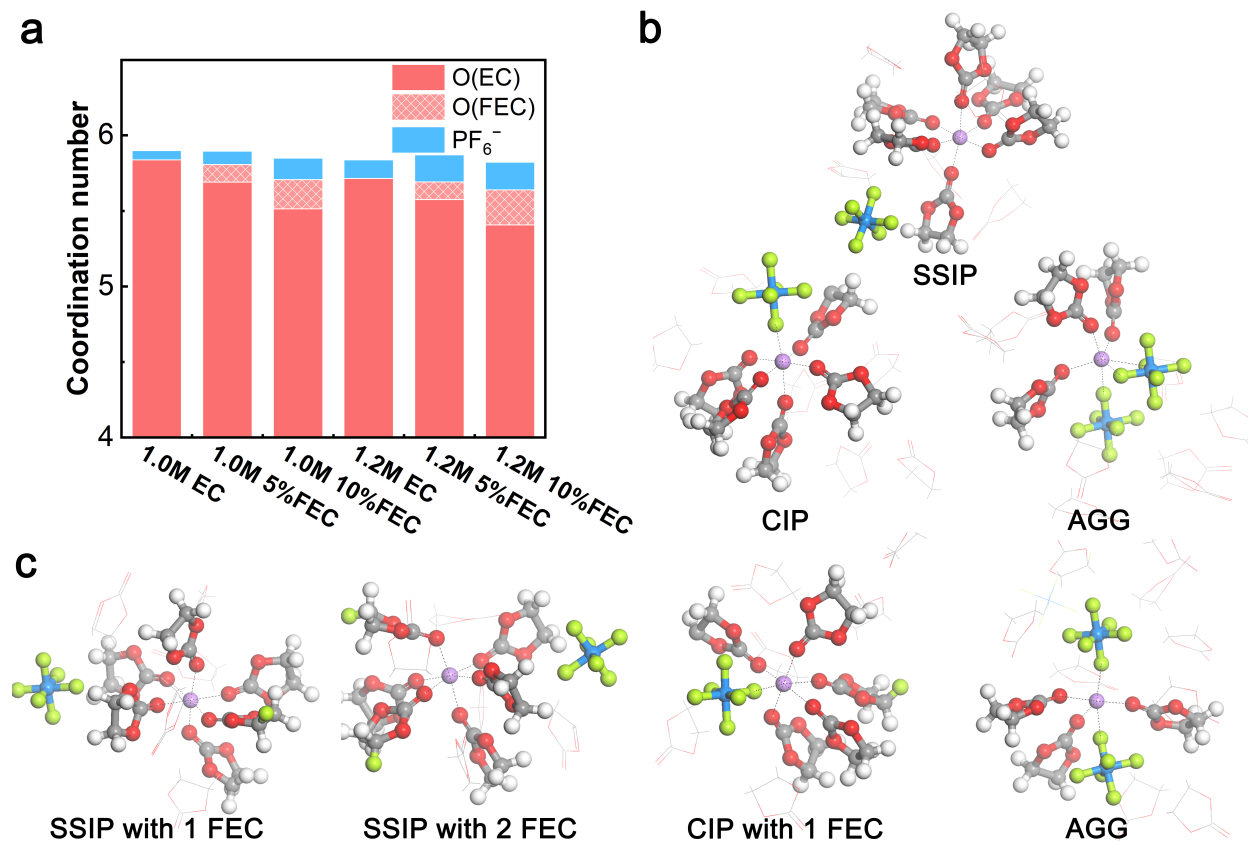
Figure 3.2 (a) The calculated total coordination number for Li^+ in 1.0 M $LiPF_6$ in EC with 0/5/10% FEC and 1.2 M $LiPF_6$ in EC with 0/5/10% FEC with specifying the contributions from EC, FEC, and PF_6^-. The representative solvation structures taken from MD simulation snapshots of (b) 1.0 M $LiPF_6$ in EC and (c) 1.0 M $LiPF_6$ in EC with 10% FEC. The carbon, hydrogen, oxygen, fluorine, phosphorus, and lithium elements are represented by grey, white, red, green, blue, and purple, respectively.

would be gradually favored with elevated T.

3.4   Transport Properties

Based on the mean square displacement (MSD) of each component during the simulation (Appendix Figure A.5), the self-diffusion coefficients and transference numbers were calculated and plotted along with the reference experimental results [139] in Figure 3.3. Both 1.0 M and 1.2 M simulation results indicate that the diffusion coefficients of all components within the EC electrolyte and EC/FEC mixture exhibit similar values (Figure 3.3a). The trends for the three components EC, PF_6^-, and Li^+ are in good agreement with the simulation results [138] obtained by a generalized AMBER force field (GAFF) [140] as well as the
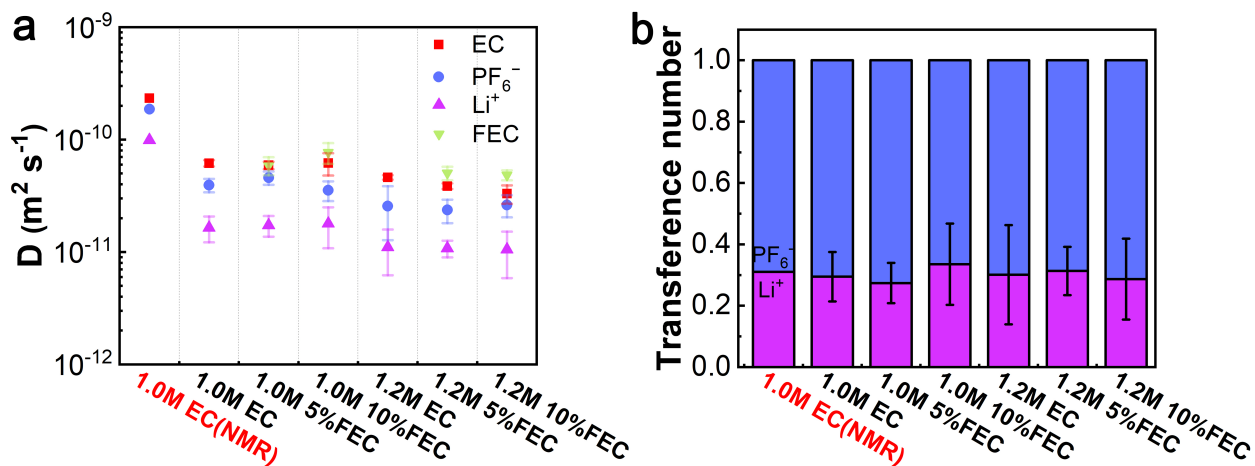
Figure 3.3 (a) Self-diffusion coefficients computed from MD simulations at 298 K as compared with NMR experiments (1.0 M LiPF$_6$ in EC) from Hayamizu et al. [139] (b) Transference numbers for Li$^+$ and PF$_6^-$ from MD simulations and NMR experiments from Hayamizu et al. [139] The error bars represent the standard deviation of the data collected every 1 ns during the 5 ns production runs.

trend from NMR results by Hayamizu et al. [139] such that solvent diffusivities are 2–5× larger than ion diffusivities. While all the simulations predict slower computed dynamics than the experimental results, the difference is within one order of magnitude (10^{-10}–10^{-11} m^2 s^{-1}.), illustrating that the classical MD simulation is adequately accurate to reproduce or predict the dynamical property trends of this system. It is noteworthy that, when FEC is added into the system, there is no significant variation of transport properties. EC and FEC exhibit almost the same diffusion coefficients within the numerical uncertainties and we surmise that the intermolecular interaction behaviors of EC and FEC are similar due to the common cyclic carbonyl structures with only one substituent. Hence, adding FEC does not directly affect the transport property of the electrolyte. On the other hand, FEC inclusion implicitly promotes the formation of CIPs while still remaining a minority species in the electrolyte. According to the Nernst–Einstein relation [141], an 8% CIP ratio increase from EC electrolyte to EC with 10% FEC will lead to approximately the same percentage (8%) decrease in Li$^+$ ionic conductivity. In contrast, the salt concentration clearly affects the ionic diffusivity, decreasing by an average of ca. 30% from 1.0 to 1.2 M, in agreement with previous studies [135]. As for the transference number, all the six electrolyte systems exhibit similar results and coincide well with the NMR experimental value of 0.35 [139]. Hence, both the self-diffusion coefficient and the transference number results demonstrate a weak dependence of transport properties on the FEC additive up to 10%, elucidating that FEC modifies the solvation structure without greatly affecting the ion transport ability.

3.5 FTIR Measurements

In order to verify the theoretical simulation results, we conducted FTIR measurements for a range of EC and EC/FEC electrolytes [142]. The peaks from the FTIR spectrum are deliberately deconvoluted to quantitatively estimate the population proportion of each electrolyte species. In parallel, we performed quantum chemical calculations to obtain the theoretical IR vibrational information for each solvation structure observed in the MD simulations. The calculated spectral profiles are further linearly combined using the population ratios obtained from MD simulations which result in predicted theoretical IR spectra. In general, there are four major characteristic peaks [143] that are shifted after the inclusion of FEC (Appendix Figure A.6): (1) the C=O stretching band at 1760–1800 cm^{-1}, (2) the C=O breathing band at 710–730 cm^{-1}, (3) the P–F stretching band at 840–880 cm^{-1}, as well as (4) the ring breathing band at 890–910 cm^{-1}. The C=O breathing vibrational band at 710–730 cm^{-1} can be used to distinguish the responses from different C=O binding states. Experimental peaks (Figure 3.4a and 3.4b) were designated as coordinated and uncoordinated based on the calculations as well as reference data [143], which provide detailed information of the solvation structure. First, we note that the experimental results are in good agreement with the calculated spectra (Figure 3.4c, 3.4d, and Appendix Figure A.7), and identical peaks are found in the spectra from both methods, despite small deviations in the absolute frequency values. For the EC electrolyte (Figure 3.4a), two peaks at 728 cm^{-1} and 715 cm^{-1} were identified as coordinated EC and uncoordinated EC, both accompanied by a small C–H deformation peak at 706 cm^{-1} [144]. By analyzing the measured peak area integrals, it was found that 38.1% of EC molecules are coordinated with Li$^+$, which corresponds to a CN of 5.13 for Li-EC. While the calculated CN (5.84) from MD simulations is slightly higher than the experimental result, notably, both approaches indicate a CN over 5 for the EC electrolyte system. When 10% of FEC is included, an additional peak arises at 738 cm^{-1}, corresponding to the coordinated FEC. Meanwhile, a free FEC breathing band at 729 cm^{-1} overlaps with the coordinated EC vibration band (Figure 3.4b), which makes it challenging to deconvolute the peaks and obtain the exact percentage of the coordinated EC and uncoordinated FEC. By comparing the peaks of the uncoordinated EC, we estimate an increase in uncoordinated EC area by 6.6% as compared to the 1 M LiPF$_6$ in the EC system, further supporting the decrease in CN of Li$^+$-EC with respect to the EC electrolyte. Additionally, the CN of FEC to Li$^+$ is directly calculated as 0.21 from the green area, which corresponds well with our previous calculation results (0.19) from the MD simulations.

In addition to the CN of solvents, the tendency for contact ion pairing was probed by analyzing the P–F bond stretching band. As shown in Figure 3.5, the peak at 838–840 cm^{-1} is identified as the response from uncoordinated PF$_6^-$, while the two peaks at 878 cm^{-1} and 834 cm^{-1} arise through Li$^+$-coordinated PF$_6^-$. In the EC electrolyte (Figure 3.5a), coordinated PF$_6^-$ contributes 6.4%, showing an excellent agreement with our simulated 6% CIP ratio. With the inclusion of FEC in the EC electrolyte (Figure 3.5b), an FEC ring deformation vibration band appears at 862 cm^{-1}, which complicates the integral area calculation. By comparing the area change of the uncoordinated peak (Appendix Figure
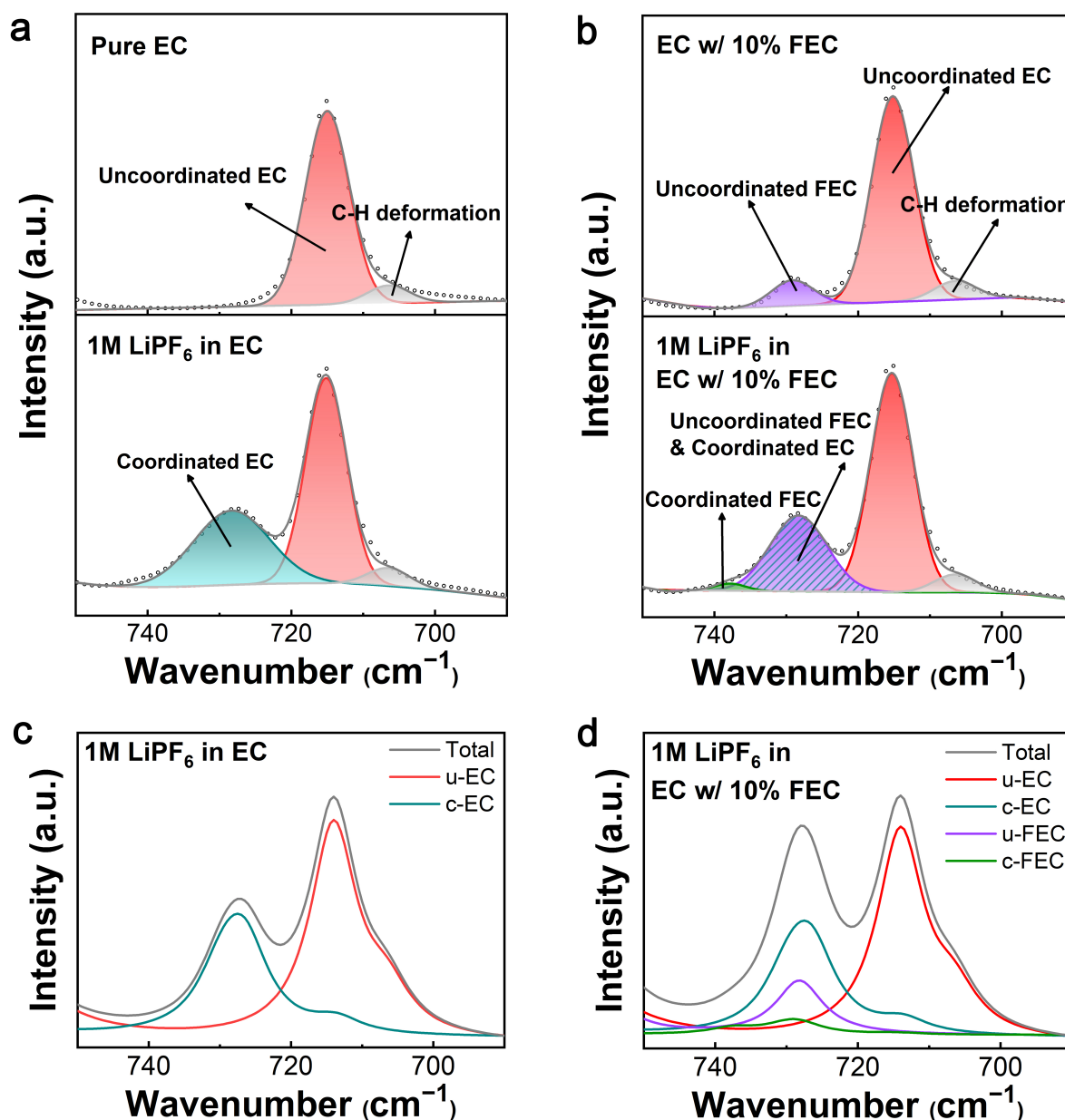
Figure 3.4 Measured FTIR spectra of the C=O breathing band of (a) pure EC and 1.0 M LiPF$_6$ in EC, and (b) EC with 10% FEC and 1.0 M LiPF$_6$ in EC with 10% FEC. (c–d) The corresponding calculated IR spectra in comparison with the experimental results. Red, cyan, purple, green, grey, and dark grey lines correspond to uncoordinated EC, EC coordinated with Li$^+$, uncoordinated FEC, FEC coordinated with Li$^+$, C–H deformation, and total spectrum, respectively. Scatter points denote the original FTIR data points.
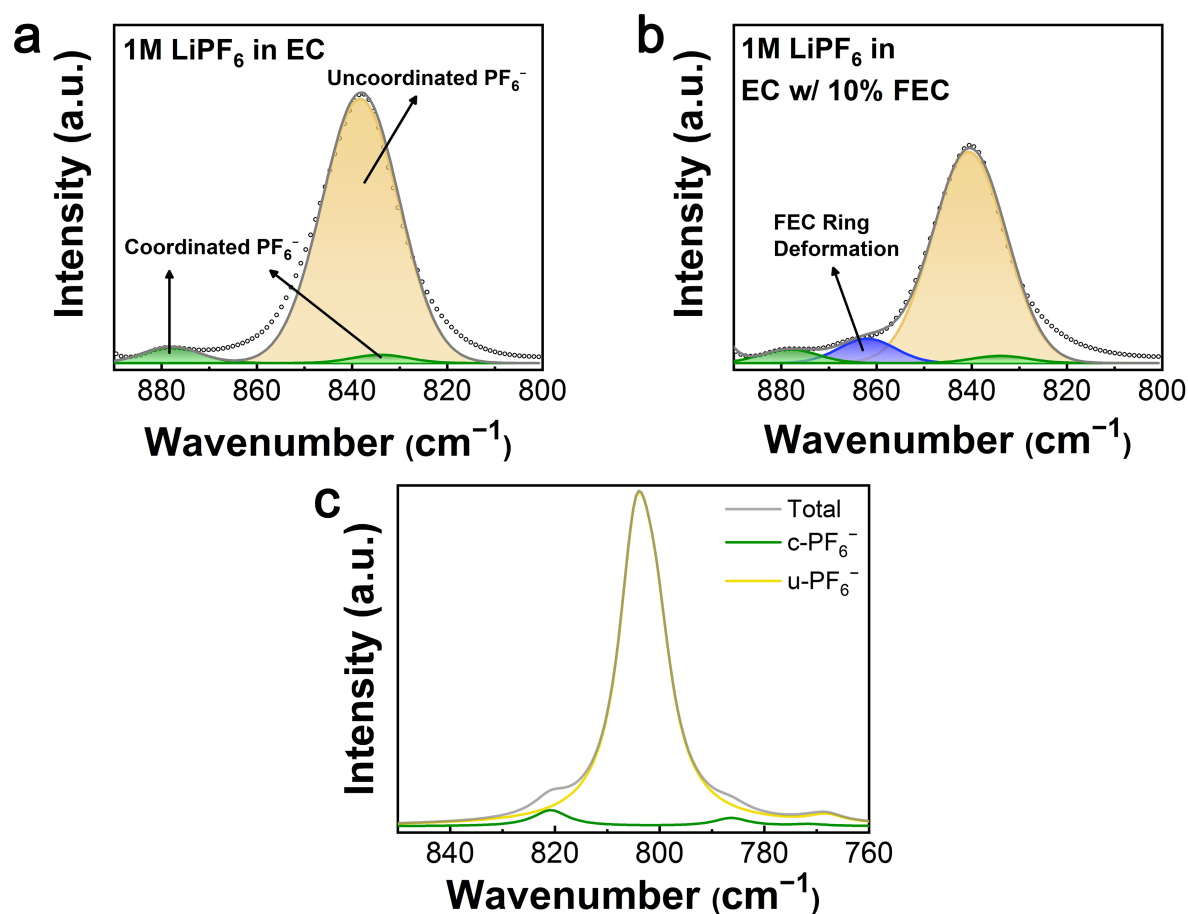
Figure 3.5 Measured FTIR spectra of the P–F bond stretching band of (a) 1.0 M LiPF$_6$ in EC, and (b) 1.0 M LiPF$_6$ in EC with 10% FEC. (c) The corresponding calculated IR spectra for 1.0 M LiPF$_6$ in EC in comparison with the experimental results. Yellow, green, blue, and dark grey lines correspond to uncoordinated PF$_6^-$, coordinated PF$_6^-$, FEC ring deformation, and total spectrum, respectively. Scatter points denote the original FTIR data points.

A.8), we estimate that approximately 15% of the total PF_6^- ions coordinate with Li^+ after adding FEC. In summary, both experimental and simulation results suggest that the CIP ratio, ca. 15%, and 14%, respectively, is increased under the influence of FEC additive.

The C=O bond stretching at 1790–1810 cm^{-1} is considered characteristic of the binding state of the carbonyl group [143]. However, an overtone peak of the ring breathing band appears at the same position in the same area (Appendix Figure A.9) [144–146]. While the C=O stretching vibration is here calculated to be a single band at 1808 cm^{-1} by first-principles, experimentally, it overlaps with the Fermi resonance of an overtone of the ring in-plane breathing band (893 cm^{-1}). When solvent molecules coordinate to Li^+, both these peaks are shifted, preventing further meaningful interpretation. As for the ring breathing band at 893 cm^{-1}, a sharp, blue-shifted signal at 904 cm^{-1} appears upon coordination (Appendix Figure A.10). The intensity of the shifted ring breathing band is significantly increased as compared to the original peak and hence prevents qualitative analysis. Consequently, due to these complexities, the C=O bond stretching and the ring breathing bands are disqualified for quantitative analysis of the solvation structure. In summary, the FTIR experiments and the MD simulations provide consistent solvation structure information. Both approaches demonstrate that the $LiPF_6$/EC electrolyte with or without FEC results in a Li^+ CN of 5–6. We note that while carbonate-based electrolytes are traditionally believed to exhibit majority species corresponding to tetrahedrally coordinated carbonyl oxygen atoms around Li^+ [138, 147, 148], the coordination number and solvation structure in these solvents systems are still under debate [148]. Recent results have reported a CN of 5–6 from two-dimensional infrared spectroscopy [149], ^{13}C NMR [137, 150], ^{17}O NMR [151], and MD simulation [135], in agreement with the results in this chapter. In contrast, several previous AIMD simulations [152–154] suggest tetrahedral Li^+-solvent coordination in the first coordination shell. However, we note that the typical simulation time in AIMD simulation (< 1 ns) is less than the residence time of a typical lithium-anion/solvent pair [66, 67] and hence it may not capture the equilibrium state. In addition, Borodin et al. [66] also reported a coordination number of 4 for 1 M $LiPF_6$/EC using a polarizable force fields model. However, a very high contact ion pair ratio of 80% was also observed in the simulation, contrasting the perception of $LiPF_6$ as a weakly coordinating salt [136].

Furthermore, our results conclusively suggest that adding FEC increases the CIP ratio while also adding another fluorine-containing species into the first solvation shell, without significantly impacting the transport properties of either Li^+ and PF_6^- ions. This minority FEC coordination with Li^+ is important, as the Li^+ solvate complex serves as a key precursor for electrode surface reduction reactions. The inclusion of FEC in the first solvation shell, even as a minority species, increases the reduction potential of FEC, due to its close proximity of Li^+, as compared to a freely solvated FEC. Hence, to further investigate the critical influence of FEC on the SEI formation process, through the solvation structure of the electrolyte, we performed first-principles calculations of the reduction potential of the solvate structures obtained from the MD simulations and analyzed their preliminary reduction products.

Table 3.2 The reduction potential vs $Li^+/Li(s)$ (i.e. subtract 1.4 V) of individual solvent molecules and solvate complexes, in Volt, where corr. denotes values after the aforementioned standard-state correction.

Structures	Reduction potential
$EC + e^- \rightarrow EC^-$	0.21 V
$FEC + e^- \rightarrow FEC^-$	0.59 V
$Li^+\text{-}EC + e^- \rightarrow Li^+\text{-}(EC)^-$	0.54 V
$Li^+\text{-}FEC + e^- \rightarrow Li^+\text{-}(FEC)^-$	0.90 V
$Li^+\text{-}(EC)_4 + e^- \rightarrow Li^+\text{-}(EC)_3(EC)^-$	0.49 V
$Li^+\text{-}(EC)_3(FEC) + e^- \rightarrow Li^+\text{-}(EC)_2(FEC)(EC)^-$	0.55 V
$Li^+\text{-}(EC)_3(FEC) + e^- \rightarrow Li^+\text{-}(EC)_3(FEC)^-$	0.91 V
$Li^+\text{-}(EC)_5 + e^- \rightarrow Li^+\text{-}(EC)_3(EC)^- + EC$	0.50 V (corr.)
$Li^+\text{-}(EC)_6 + e^- \rightarrow Li^+\text{-}(EC)_3(EC)^- + 2EC$	0.59 V (corr.)
$Li^+\text{-}(EC)_5(FEC) + e^- \rightarrow Li^+\text{-}(EC)_3(FEC)^- + 2EC$	0.81 V (corr.)
$Li^+\text{-}PF_6^- + e^- \rightarrow Li^+\text{-}F^- + PF_5^-$	spontaneous bond breaking
$Li^+\text{-}PF_6^-(EC) + e^- \rightarrow Li^+\text{-}PF_6^-(EC)^-$	0.59 V
$Li^+\text{-}PF_6^-(FEC) + e^- \rightarrow Li^+\text{-}PF_6^-(FEC)^-$	0.90 V
$Li^+\text{-}PF_6^-(EC)_5 + e^- \rightarrow Li^+\text{-}(EC)_3(EC)^- + PF_6^- + EC$	0.44 V (corr.)

3.6 Reduction Potentials

The reduction potentials of free EC and FEC, their corresponding Li^+(solvent) complexes, and $Li^+\text{-}PF_6^-$ (solvent) complexes were investigated at the B3LYP/6-31+g(d) level of theory (Table 3.2). To effectively compare with experimental results, the calculated potential values were convoluted with an arbitrary 0.1 V width concave triangular wave, and plotted together with the experimental differential capacity (dQ/dV) versus potential (V) profile (Figure 3.6) [155]. The reduction products after geometry optimization were further scrutinized through spin density analysis to elucidate the reduction reaction process (Figure 3.7). The free EC molecule exhibits a calculated reduction potential of 0.21 V, with most of the extra electron residing on the O=CO(O) moiety which consequently deforms out of plane. According to Natural Bond Orbital (NBO) analysis, the C atom hybridization state changes from $sp^{2.0}$ to $sp^{2.6}$ to accommodate the extra e^-. The coordinated EC exhibits an increased reduction potential of 0.44 V–0.59 V (within 0.15 V), as compared with the uncoordinated molecule, which contributes to a broadening of the reduction peaks in the differential capacity plot. The obtained reduction potential is in good agreement with the previously obtained value of 0.53 V by G4MP2 [118]. Furthermore, the electron density of the reduced coordinated EC resides in the same region (e.g., on the O=CO(O)) as compared to the uncoordinated reduced EC. (Figure 3.7c, h, i, k, and l). We find weak to little dependence of the reduction potential on the number of explicitly coordinating solvents [118, 156], e.g., the calculated corresponding reduction potentials are 0.50 V and 0.59 V for 5- and 6- fold structures (Fig-
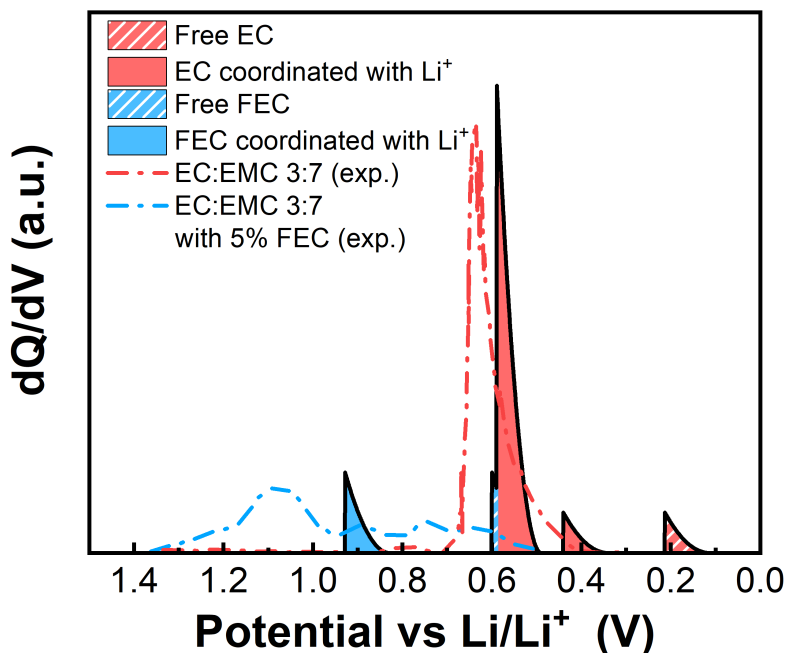
Figure 3.6 The calculated anticipated (solid line) and experimental (dash dotted line) differential capacity plots (dQ/dV vs. V) during the formation step of EC and FEC electrolyte. The computed profile is obtained by convoluting the calculated reduction potentials with a 0.1 V width concave triangular wave, the experimental one is reproduced from Xia, et al. [155] by removing the background.

ure 3.7k, and l), respectively. However, when Li$^+$ is in direct coordination with FEC, the predicted FEC reduction potential is obtained as 0.81-0.91 V, which is about 0.3 V higher than uncoordinated FEC. The calculated reduction potentials are in good agreement with the previous G4MP2 calculations (0.90 V) and measured values (1.0 V) [157]. If we compare the reduction behavior of EC-containing species and FEC-containing species, even the uncoordinated FEC exhibits an equal or higher reduction potential than all investigated EC species, indicating a preferential reduction for FEC vs EC—for both minority as well as majority species. While the optimized FEC reduction products (Figure 3.7b, d, j, and m) exhibit the same electron distributions as their EC counterparts, the stronger exothermic nature of the FEC reduction indicates that these FEC-derivative species are sufficiently metastable to decay through reactions other than the C–O bond ring-opening of EC [44]. This major mechanistic difference between the non-fluorinated and fluorinated carbonates allows for the recombination of fragments and intramolecular electron migration, facilitating the subsequent polymerization and LiF formation [44]. Previous DFT calculations have shown that the additional F fragments from FEC decomposition exhibit a "glue effect" by

strongly binding to Li atoms of multiple organic species and connecting them [122], leading to a more compact and stable SEI. The formation of Li^+-coordinated FEC species is especially important because, in their absence, there is no early onset FEC reduction. Indeed, uncoordinated FEC is predicted to reduce at a similar potential as Li^+ coordinated EC, which, as the majority solvent, will then dominate the SEI formation process. We also note that, as Li^+-coordinated FEC minority species are decomposing at higher potentials, the bulk equilibrium will shift to maintain the population, hence supplying the reaction.

The reduction of the Li^+-PF_6^- contact ion pair results in direct LiF formation. Upon geometry optimization, the PF_6^- structure is dynamically unstable, and the P–F bond spontaneously breaks to form PF_5^- and LiF (Figure 3.7e). However, the Li^+-PF_6^- ion pair decomposition is expected to yield a high reaction barrier at a potential larger than 0.5 V [158]. When explicit solvent molecules are considered in the contact ion pair model, the reduction of the complex results in the solvent reduction, elucidating that the decomposition of solvent molecules is preferred over that of the ion-paired PF_6^- (Figure 3.7f, g, and n), with similar reduction potential as SSIP structures. Thus, FEC will be reduced before other species considered here. The reduction of PF_6^- is not expected to occur except at very high overpotentials, possibly at the final stage of SEI formation [158]. Therefore, we suggest that FEC is the major contributor to the formation of the SEI LiF as compared to PF_6^-. It is also speculated that the decomposition of PF_6^- is related to H_2O contamination rather than electrochemical reactions [112]. The degradation mechanism for $LiPF_6$ was suggested to be [159]:

$$LiPF_6 \leftrightarrow LiF + PF_5$$
$$PF_5 + H_1O \rightarrow POF_2 + 2\ HF$$
$$ROCO_2Li,\ Li_2CO_3 + HF \rightarrow LiF + ROCO_2H,\ H_2CO_3$$
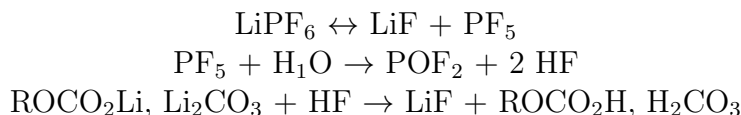
On one hand, a higher CIP ratio in the presence of FEC would facilitate the formation of LiF. The increased amount of Li^+-PF_6^- ion pairs would promote PF_5 formation and pronounced hydrolysis, and the as-formed HF would subsequently react with the SEI carbonate species, which are initial reduction products, to form LiF [160]. Even if the trace amount of water is ignored, FEC is prone to defluorination in the presence of a Lewis acid like PF_5, and subsequently generates F species [161]. Consequently, a greater amount of inorganic components in SEI, introduced by the sacrificial anion decomposition [43, 162] or FEC defluorination, is believed to result in improved Li^+ cation transport. However, excessive HF formation under elevated temperatures may also cause SEI destruction [161], such that the operating temperature of the FEC-containing electrolyte should be controlled to avoid detrimental effect. On the other hand, an early onset of FEC reduction allows for rapid passivation at a higher potential than EC which may limit PF_6^- reduction/decomposition. Therefore, the influence of FEC on PF_6^- decomposition is non-trivial to deconvolute. Future experimental and computational research, e.g. isotopic labeling, is recommended.

In summary, despite limited FEC concentration, we find that its presence significantly influences the properties of the electrolyte via three main mechanisms: (i) the Li^+-coordinated
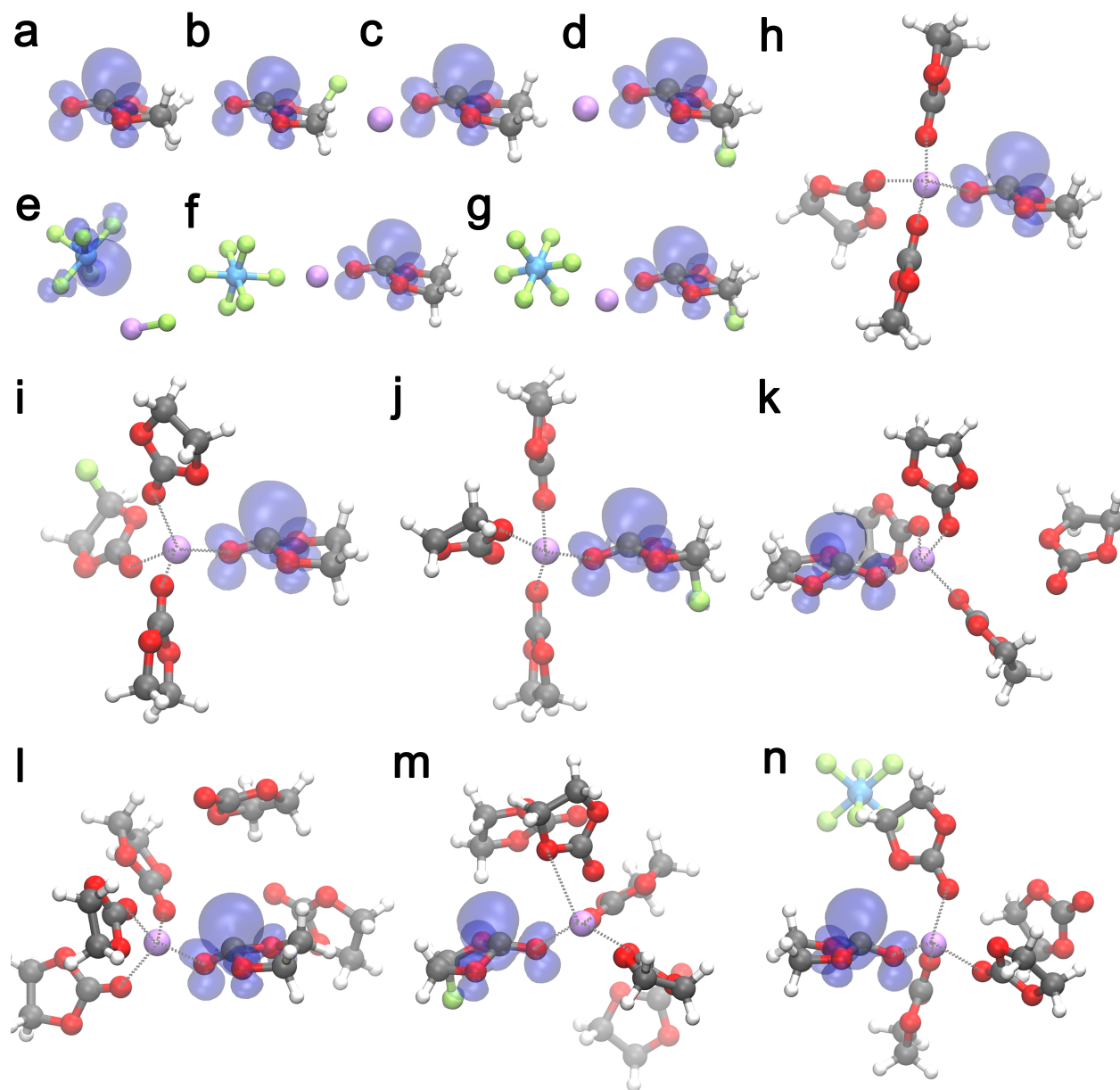
Figure 3.7 Geometries and spin density analysis of reduced solvent molecules (a) EC, (b) FEC, and solvate complexes (c) Li$^+$-EC, (d) Li$^+$-FEC, (e) Li$^+$-PF$_6^-$, (f) Li$^+$-PF$_6^-$(EC), (g) Li$^+$-PF$_6^-$(FEC), (h) Li$^+$-(EC)$_4$, (i) Li$^+$-(EC)$_3$(FEC) (EC reduction), (j) Li$^+$-(EC)$_3$(FEC) (FEC reduction), (k) Li$^+$-(EC)$_5$, (l) Li$^+$-(EC)$_6$, (m) Li$^+$-(EC)$_5$(FEC) (FEC reduction), and (n) Li$^+$-PF$_6^-$(EC)$_5$.

FEC exhibits higher reduction potential than corresponding coordinated EC species and uncoordinated FEC, and hence contributes to an early onset of anode SEI formation and passivation, and (ii) the preferred reduction of FEC introduces a higher ratio of LiF to the SEI as compared to the EC equivalent electrolyte, and lastly (iii) a higher CIP ratio may possibly lead to increased LiF formation. The exothermic nature of the FEC reduction also supports the reported reaction pathway of defluorination and subsequent polymerization. Therefore, the origin of the excellent performance of FEC containing electrolyte may be attributed to the higher reduction potential to enable early passivation [163], substituents that promote inorganic product formation [164], and metastable intermediates to facilitate alternative reaction pathways (such as polymerization) [44, 95].

3.7 Conclusions

The influence of FEC on $LiPF_6$/EC electrolytes is investigated through classical MD simulations, FTIR experiments and first-principles calculations. The calculated solvation structure corroborates well with the liquid structure information inferred by experiments. While select previous work advocates Li^+ coordination numbers closer to 4, both theoretical and experimental results presented here support a Li^+ solvent coordination number of 5–6 for 1.0/1.2 M $LiPF_6$/EC electrolytes, with or without FEC. However, reduction potentials are found to exhibit only weak dependence on the explicit number of coordinating solvents, such that 4-fold as well as 6-fold structures show similar values. Furthermore, while it is widely assumed that electrolyte additives remain largely uncoordinated in LIB electrolytes, we find that FEC, as a minority species, significantly modifies the solvation structure and reduction behavior of the electrolyte while being innocuous to the transport properties of the electrolyte. Even limited 5–10% addition of FEC results in a notably higher CIP ratio (14%, 1.0 M EC w/ 10% FEC) as compared to the parent EC electrolyte (6%, 1.0 M EC). FEC itself, as a fluorine-containing species, appears in the solvate complex, in 19% of the Li^+ first solvation shells (1.0 M EC w/ 10%FEC). We find that the Li^+-coordinated FEC is preferentially reduced at higher reduction potentials (about 0.3 V higher than corresponding EC clusters and uncoordinated FEC), which provides early onset SEI formation and passivation of the anode surface. Meanwhile, the as-formed reduction products of FEC include a higher ratio of LiF as compared to the EC equivalent electrolyte, and a higher CIP ratio due to FEC addition may further benefit LiF formation, leading to enhanced electrochemical performance. By elucidating the solvation structure of the FEC additive in $LiPF_6$/EC, and its effect on the reduction potentials of the composite electrolyte, we hope to improve our understanding of the SEI-formation and its subtle dependence on the detailed intermolecular interactions and resulting solvation structure of the electrolyte.

Chapter 4

The Modeling of Binary/Ternary Mixed-Carbonate Electrolytes

Despite the extensive employment of binary/ternary mixed-carbonate electrolytes (MCEs) for Li-ion batteries, the role of each ingredient with regards to the solvation structure, transport properties, and reduction behavior is not fully understood. In this chapter, the Gen2 (1.2 M $LiPF_6$ in ethylene carbonate (EC) and ethyl methyl carbonate (EMC)) and EC-base (1.2 M $LiPF_6$ in EC) electrolytes, as well as their mixtures with 10 mol% fluoroethylene carbonate (FEC), are investigated by atomistic modeling and transport property measurements. Due to the mixing of cyclic and linear carbonates, the Gen2 electrolyte is found to have a 60% lower ion dissociation rate and a 44% faster Li^+ self-diffusion rate than the EC-base electrolyte, while the total ionic conductivities are similar. Moreover, we propose for the first time the anion–solvent exchange mechanism in MCEs with identified energetic and electrostatic origins. For electrolytes with additive, up to 25% FEC coordinates with Li^+, which exhibits a preferential reduction that helps passivate the anode and facilitates an improved solid electrolyte interphase. The work provides a coherent computational framework for evaluating mixed electrolyte systems.

4.1 Introduction

As discussed in the first chapter, the key descriptors for electrolyte performance lie in three major categories: the solvation behavior, the transport properties, and the electrochemical reduction/oxidation behavior. Extensive efforts have been devoted to understanding the solvation and transport property of non-aqueous electrolytes. Instrumental measurements including infrared spectroscopy (IR) [149, 150, 165], and Raman [144, 166] have been utilized to determine the ion–solvent coordinating states. However, conventional spectroscopic methods are not without limitations for binary or ternary mixed-carbonate electrolytes (MCEs), since it is difficult to quantitatively deconvolute the overlapping peaks of different carbonate species, the overtone peaks, and the accompanied Fermi resonance effects, especially when

solvents share the same functional groups [8, 167]. In addition, because of the possible difference in spectroscopic sensitivity between the coordinated and uncoordinated states of solvent moieties, the scaling of peak area integrals is required to obtain the actual molar ratio of species [137], which could introduce additional error and hinders straightforward quantitative interpretation. Most recently, an internally referenced diffusion-ordered spectroscopy (IR-DOSY) technique has been introduced to determine the solvation state of individual solvents in binary electrolyte systems, which may help overcome the limitation of conventional vibrational spectroscopy [8, 168]. As an alternative approach, computational methods including ab-initio molecular dynamics (AIMD) [133, 169, 170] and classical molecular dynamics (MD) [148, 171–173] simulations have shown satisfying results in modeling the solvation and transport behaviors. In chapter 3 we have shown the MD simulations of 1.0 and 1.2 M LiPF$_6$ in EC, revealing detailed solvation structures of the single-solvent electrolyte where cations and anions are mostly dissociated and uncorrelated. As a result, the ionic conductivity can be directly estimated by the Nernst–Einstein (NE) equation with the assumption that ions are fully dissociated without any interactions [174]. However, in MCEs, the NE equation is not applicable because of significantly correlated ion motions [138, 175]. Despite the approximate treatment of the correlated term of conductivity proposed by Borodin et al. [66, 176, 177], the ionic conduction mechanism, including the contribution from multimeric species, of MCEs is not completely understood. Most recently, Fong et al. [51, 72] demonstrated a rigorous methodology for analyzing transport properties in electrolytes, including Green–Kubo (GK) relations for the total conductivity and transference number. This approach will be used herein to enable a comprehensive study of transport in MCEs.

The electrochemical reactivity of electrolytes determines the voltage window of batteries. More importantly, constructing a stable and efficient SEI intrinsically formed by electrolytes is among the most effective strategies to achieve superior cycling performance [178]. While EC has been long recognized as the major component that regulates the anode SEI [179–181], recent findings indicate that linear carbonates with a theoretically lower reduction potential could also facilitate the SEI formation [90]. Furthermore, with the intensive studies on emerging Li metal and Si anode materials, electrolyte additives as minor species (e.g. fluoroethylene carbonate (FEC)) are recruited in novel electrolyte design to enhance the strength and stability of the SEI film [5, 42]. Consequently, in order to understand the macroscopic electrochemical performance, a comprehensive molecular-level investigation of MCEs is of great significance to deconvolute the influence of individual species and identify possible synergetic effects.

In this chapter, a binary MCE, Gen2 electrolyte (1.2 M LiPF$_6$ in EC:EMC (w/w 3:7)), along with EC-base electrolyte (1.2 M LiPF$_6$ in EC), GenF electrolyte (Gen2 + 10 mol% FEC), and ECF electrolyte (EC + 10 mol% FEC), is investigated by the atomic-scale modeling and transport property measurements to decipher the different roles of anion, cyclic carbonate, linear carbonate, and additive. Detailed static and dynamic solvation structure information is obtained from MD simulations. Self-diffusion coefficients, ionic conductivity, and residence times are computed to characterize the transport properties. Using MD-obtained solvation structures as input, the electrostatic potential, solvent exchange energy,

and reduction potential calculations are conducted using quantum chemistry to fully depict the solvation structure and its influence on the reduction behavior of electrolytes. The quantitative atomistic modeling of MCEs provides new insights into conventional carbonate electrolytes and novel electrolyte design.

4.2 Computational and experimental details

Classical molecular dynamics (MD)

MD simulations were performed using LAMMPS (Large Scale Atomic/Molecular Massively Parallel Simulator) [123]. The bonded and non-bonded parameters for EC, EMC, and FEC were obtained from the OPLS-AA force fields (Optimized Potentials for Liquid Simulations All Atom) [80, 81], while those for PF_6^{-1} are taken from Lopes et al. [127] and Li^+ from Jensen et al. [128] The partial atomic charges were fitted using the RESP method [131, 132]. Long-range electrostatic interactions were handled by the particle-particle particle-mesh (PPPM) solver with a grid spacing of 0.1 nm. A cutoff distance of 1.5 nm was used for electrostatic and 12–6 Lennard-Jones interactions. The molecules were initially packed randomly in a cubic box using PACKMOL [124] (Appendix Figure B.1). The force field is further benchmarked against experimental properties and quantum chemistry (see Appendix B).

All simulation box consists of 1500 solvent molecules in EC-base (1500 EC), ECF (1350 EC, 150 FEC), Gen2 (504 EC, 996 EMC), and GenF (454 EC, 896 EMC, 150 FEC). A salt concentration of 1.2 M was made by adding 126 $LiPF_6$ into EC-base/ECF and 166 $LiPF_6$ into Gen2/GenF, respectively. The initial configuration was minimized by a conjugated-gradient energy minimization scheme employing a convergence criterion of 1.0×10^{-4}. The electrolytes were then equilibrated for 5 ns in the isothermal-isobaric ensemble (constant NPT) using the Parrinello–Rahman barostat to maintain a pressure of 1 bar and a temperature of 298 K with a time constant of 1 ps. An annealing process was conducted to further guarantee that all systems are melted and to avoid local configuration confinement. All systems were heated from 298 K to 400 K for 1 ns, and maintained at 400 K for 2 ns, and subsequently annealed from 400 to 298 K in 2 ns. Finally, production runs of 60 ns were conducted in the canonical ensemble (NVT) under Nosé-Hoover thermostats with a time constant of 1 ps at 298 K. The simulation time was long enough to sample adequately the Fickian (diffusive) regime of all systems as demonstrated in Chapter 3. At least four independent duplicate runs were performed for each electrolyte in order to estimate the statistical uncertainties.

The solvation structure and transport properties analysis of the MD trajectories utilizes the MDAnalysis [182] python package. The detailed population of species, and solvent-specific solvation numbers are listed in Appendix Table B.1, B.2. The simulations performed here all reached the linear regime as with the diffusion coefficient analysis above. Results from four representative simulations of the EC-base electrolyte are shown in Appendix Figure B.3 to demonstrate this linear behavior for both self-diffusion coefficients and ionic conductivities

calculation.

The neighbor distance cutoffs in the residence time calculation are 3 Å between Li^+ and the carbonyl O for Li^+-EC, Li^+-EMC, and Li^+-FEC pairs, and 5 Å between Li^+ and P for the Li^+- PF_6^- pair according to the first minimum of radial distribution functions in Chapter 3. The reported values and uncertainties of the total ionic conductivity, self-diffusion coefficient, residence time, population of solvation species, and solvent-specific coordination number are estimated by calculating the mean and standard deviation of the quantities obtained from the four independent 60 ns duplicates.

Quantum chemical calculations

The anion solvent exchange energy and electrostatic potential were calculated using B3LYP-D3(BJ)/6-311+g(d,p) [129, 183, 184]//B2PLYPD3/def2TZVP [185, 186] level of theory with implicit solvent model IEF-PCM(UFF,Acetone) [187, 188] in Gaussian 16 [130]. Quasi-harmonic entropy and enthalpy correction with a cutoff frequency of 100 cm^{-1} were applied as suggested by Grimme et al. [189] using the GoodVibes [190] program. For the electronic contributions, it is assumed that the first and higher excited states are entirely inaccessible. For the entropy contributions, it is assumed that the implicit solvent model together with explicit solvent molecules is sufficiently accurate for modeling the free energy change of a molecule from an ideal gas to a solution phase. The calculated free energy includes the entropy contributions resulting from the translational, electronic, rotational, and vibrational motion. A dielectric constant (ϵ) of 20.493 (Acetone) was adopted, which is similar to the reported value of 19.

The energy decomposition analysis based on absolutely localized molecular orbitals within an implicit solvent model (ALMO-EDA(solv)) [86–88] were performed using Q-Chem 5.2.0 [191], B3LYP-D3(BJ)/6-311+g(d,p) [129, 183, 184] level of theory, and an implicit solvent model IEF-PCM(UFF,ϵ=19.0) [187, 188].

Ionic conductivity measurement

Ionic conductivities of the four electrolytes were measured by Mettler Toledo SevenCompact Cond meter S230, which is equipped with a 4-electrode Pt conductivity probe (Mettler Toledo, InLab 710). The probe was calibrated with a standardized 12.88 mS cm^{-1} potassium chloride (KCl) solution (Mettler Toledo). After the successful calibration of the instrument, the ionic conductivities of the four electrolytes were measured in an Ar-filled glove box (O_2, H_2O < 0.1 ppm) at a temperature range of 29-35 °C, and corrected to 25 °C by a linear correction regime. The error of the conductivity meter and the linear correction is estimated as no more than 0.2 mS cm^{-1}. The amount of the salt and solvents used for the electrolyte preparation and the measured conductivities are shown in Appendix Table B.3, B.4.
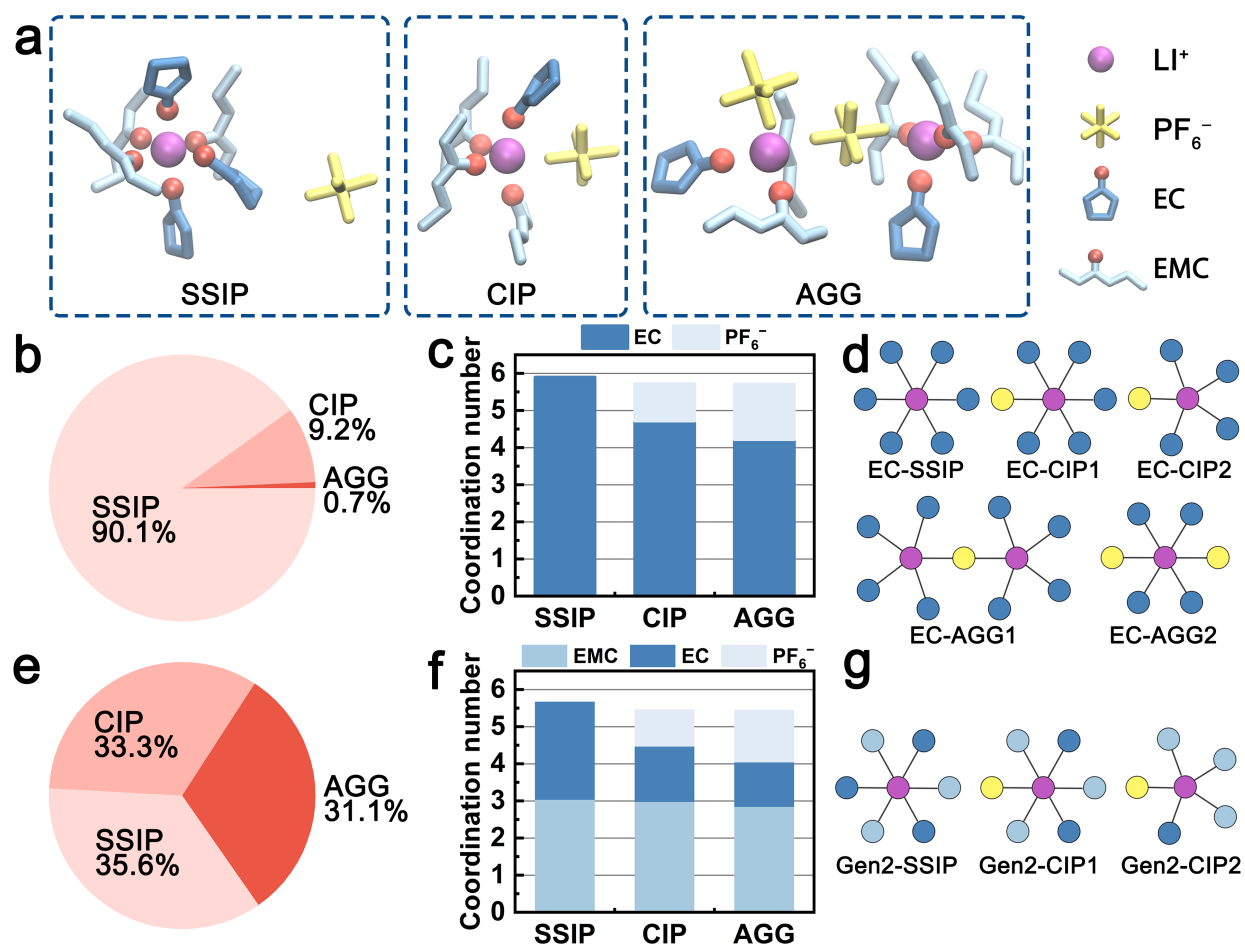
Figure 4.1 The solvation structure analysis of the EC-base and Gen2 electrolytes. (a) Three representative solvation structures of solvation separated ion pairs (SSIP), contact ion pairs (CIP), and aggregate (AGG) species in the Gen2 electrolyte. The light blue, dark blue, light yellow line representations denote the EMC, EC, and PF_6^- clusters, respectively. The purple and red ball representations denote Li ions and coordinating carbonyl O atoms, respectively. (b-d) The population, solvent-specific coordination number, and representative solvation structures of SSIP, CIP, and AGG species in the EC-base electrolyte. (e-g) The population, solvent-specific coordination number, and representative solvation structures of SSIP, CIP, and AGG species in the Gen2 electrolyte.

4.3 Solvation structure of the Gen2 and EC-base electrolytes

The solvation structures obtained from the MD simulations are categorized into three species, i.e., solvent-separated ion pairs (SSIP), contact ion pairs (CIP), and aggregates (AGG). Figure 4.1a shows examples of the three species in the Gen2 electrolyte that are extracted

from MD trajectories. For all the three species, both EC and EMC are observed in the first solvation shell and coordinate with Li^+ ions via the carbonyl oxygen. Figure 4.1b and e quantitatively compare the ratios of the three species in the EC-base and Gen2 electrolytes. In the EC-base electrolyte, the majority (90.1%) of Li^+ are dissociated (SSIP), while in the Gen2 electrolyte, a much smaller proportion (35.6%) of SSIP species was observed, with CIP and AGG species contributing 33.3% and 31.3%, respectively. The low ion dissociation rate of the Gen2 electrolyte agrees well with previous experimental results using conductivity measurement [139] and FTIR spectroscopy [165], as well as simulation results using non-polarizable [173] and polarizable force field [66]. This can be attributed to the reduced permittivity of the Gen2 electrolyte as a result of mixing EC ($\epsilon = 90$) and EMC ($\epsilon = 2.96$) [7]. Using nodes and vertices expression, we plotted the 2D topology graphs of the majority solvation structures observed in the EC-base and Gen2 electrolyte, as presented in Figure 4.1d, g, and Appendix Figure B.2. It should be noted that, while the EC-base electrolyte has a much higher SSIP ratio than the Gen2 electrolyte, more than half of AGG in the Gen2 electrolyte are charged species (19% out of 31%), which narrows the population gap of ionically conductive species between the EC-base and Gen2 electrolyte. However, the bulky and sluggish AGG species are expected to diffuse slower and cannot transport Li^+ as efficiently as SSIP species [8].

The coordination numbers in the two electrolytes are systematically analyzed. In average, the total solvent coordination number in the Gen2 electrolyte is 4.7, with 1.8 EC and 2.9 EMC, corresponding to an EC:EMC relative solvating power (X) of 1.59, which is the ratio between the coordination percentage of EC and the coordination percentage of EMC [168]. The result is in excellent agreement with the IR-DOSY experiments reporting a solvent coordination number of 4.64 and an EC:EMC relative solvating power of 1.42 in 1:4:4 (molar ratio) $LiPF_6$:EC:EMC electrolyte [8]. Furthermore, we have computed the detailed solvent-specific coordination numbers for the three species (Figure 4.1c, f). For both the EC-base and Gen2 electrolyte, the total number of coordinating solvent molecules decreases from about 6 to 4 when Li^+ ions are engaged in higher degrees of ion association (SSIP to AGG). Notably, in the Gen2 electrolyte, only the coordination number of EC decreases (from 2.6 to 1.2 with an increased degree of ion association) when PF_6^- enters the solvation sheath while that of EMC is preserved (about 3). This trend is confirmed by anion–solvent exchange free energy calculations (Table 4.1; Appendix Figure B.5). Three exchange reactions from a SSIP species (3 EC and 3 EMC) to CIP species with varying number of EC and EMC were calculated using MD obtained structures. The reaction replacing a Li^+-coordinated EC with a PF_6^- exhibits the largest free energy gain, while the reaction replacing a Li^+-coordinated EMC with a PF_6^- is energetically unfavored, which is in good agreement with the MD statistics. Therefore, the EC molecules are preferentially desolvated when Li^+ coordinates with PF_6^-. To fully understand the different exchange mechanisms of EC and EMC, we rationalize the phenomena in terms of electrostatic repulsion in the following sections.

Table 4.1 Anion–solvent exchange free energy from SSIP to CIP.

Anion–solvent exchange reaction	ΔG (kJ mol^{-1})
Li^+-$(EMC)_3(EC)_3 + PF_6^- \rightarrow Li^+$-$(EMC)_3(EC)_2PF_6^- + EC$	-9.5
Li^+-$(EMC)_3(EC)_3 + PF_6^- + EMC \rightarrow Li^+$-$(EMC)_4(EC)_1PF_6^- + 2EC$	-6.7
Li^+-$(EMC)_3(EC)_3 + PF_6^- \rightarrow Li^+$-$(EMC)_2(EC)_3PF_6^- + EMC$	1.7

4.4 Anion–solvent exchange mechanism

Analogous to the nucleophilic substitution reactions, the "exit-entry" type and "entry-exit" type are considered two hypothetic mechanisms when the PF_6^- exchanges with solvent molecule (Figure 4.2a). The anion and solvent molecule exchange with the "exit-entry" type mechanism following two steps: (1) the leaving solvent/anion separates with the Li^+ (exit), (2) the incoming anion/solvent coordinates with the Li^+ (entry); and vice versa for the "entry-exit" type. In order to reveal the exchange mechanism, the coordination numbers of EC and EMC before and after each CIP–SSIP transition event (set as 0 ps) are extracted from the trajectories and averaged over all such events (Figure 4.2b). When PF_6^- exits the first solvation shell (upper panel), the solvation structure changes from CIP to SSIP. The average EC coordination number with Li^+ is above 2.1 before the transition, which is higher than the bulk average of all CIP species (1.5). This indicates that PF_6^- is more probable to leave the solvation shell when more EC molecules are coordinated. After PF_6^- separates with Li^+ ions at 0 ps, the coordination numbers of both EC and EMC gradually increase to the bulk average of SSIP in about 100-200 ps, suggesting that the exchange is predominantly an "exit-entry" type. Likewise, when PF_6^- enters the solvation sheath (lower panel), the solvation structure changes from SSIP to CIP. The coordination number of EC as well as the total coordination number before the event is about 0.6 lower than the bulk average of SSIP. The coordination number of EC drops even further from -100 ps to 0 ps. This indicates that PF_6^- preferentially associates with Li^+ ions that have less EC coordinated and a "vacant" coordination site. Subsequently, the coordination numbers of both EC and EMC remain almost unchanged after the PF_6^- coordination. Therefore, the "exit-entry" type mechanism is expected to dictate the anion–solvent exchange in both directions. To the best of our knowledge, this has not been previously reported.

To further visualize the anion–solvent exchange process, a 400 ps long trajectory in the Gen2 electrolyte with an EC–PF_6^- exchange event is exhibited as an example in Figure 4.2c-f. At time 150 ps, the central Li^+ coordinates with the highlighted EC solvent. Next, the EC molecule starts to leave the Li^+ solvation shell, and an undercoordinated Li^+ solvation structure is captured at 180 ps. Subsequently, the PF_6^- enters the solvation shell to coordinate with Li^+, and a CIP structure is formed at 210 ps. The duration of the sampled exchange event is less than 100 ps, which agrees with the observation in the lower panel of Figure 4.2b.

The electrostatic repulsion, arising from the high dipole moment of EC and the negative
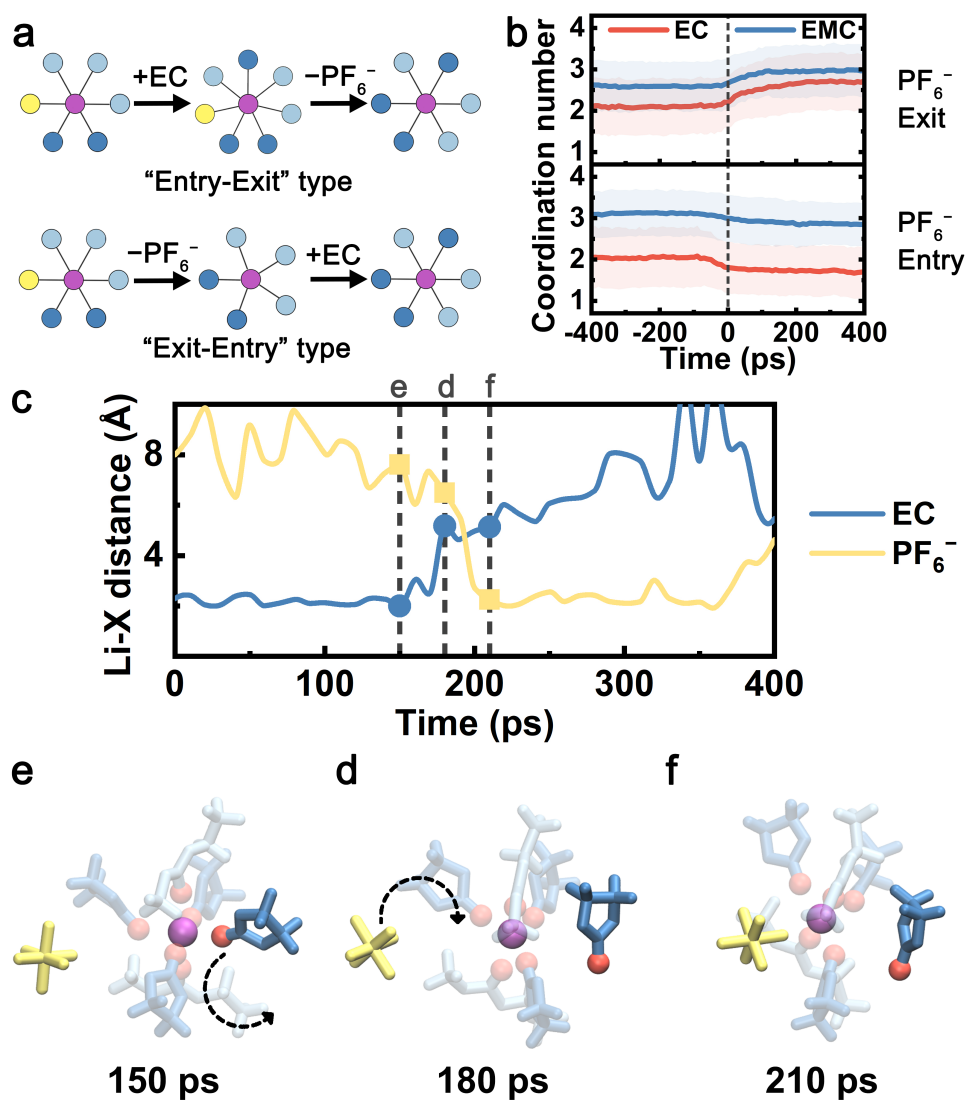
Figure 4.2 The anion–solvent exchange mechanism. (a) Node graph representations of two types of anion–solvent exchange mechanism, the "entry-exit" type and "exit-entry" type. (b) The coordination numbers of EC and EMC as a function of time before and after each "PF_6^- exit" or "PF_6^- entry" event. The time of each event happens is set as 0 ps, and the coordination numbers are averaged over all such events. The light-colored area denotes the extent of standard deviation. (c-f) Sample trajectory of EC–PF_6^- exchange in the Gen2 electrolyte. (c) Li^+–X (X = carbonyl O in EC or F in PF_6^-) distance as a function of time. The snapshots of the sampled Li^+ solvation shell at (d) 150 ps, (e) 180 ps, and (f) 210 ps of the time slice. The color scheme is the same as Figure 4.1a. The non-exchanging coordinated molecules are set as transparent for clarity.
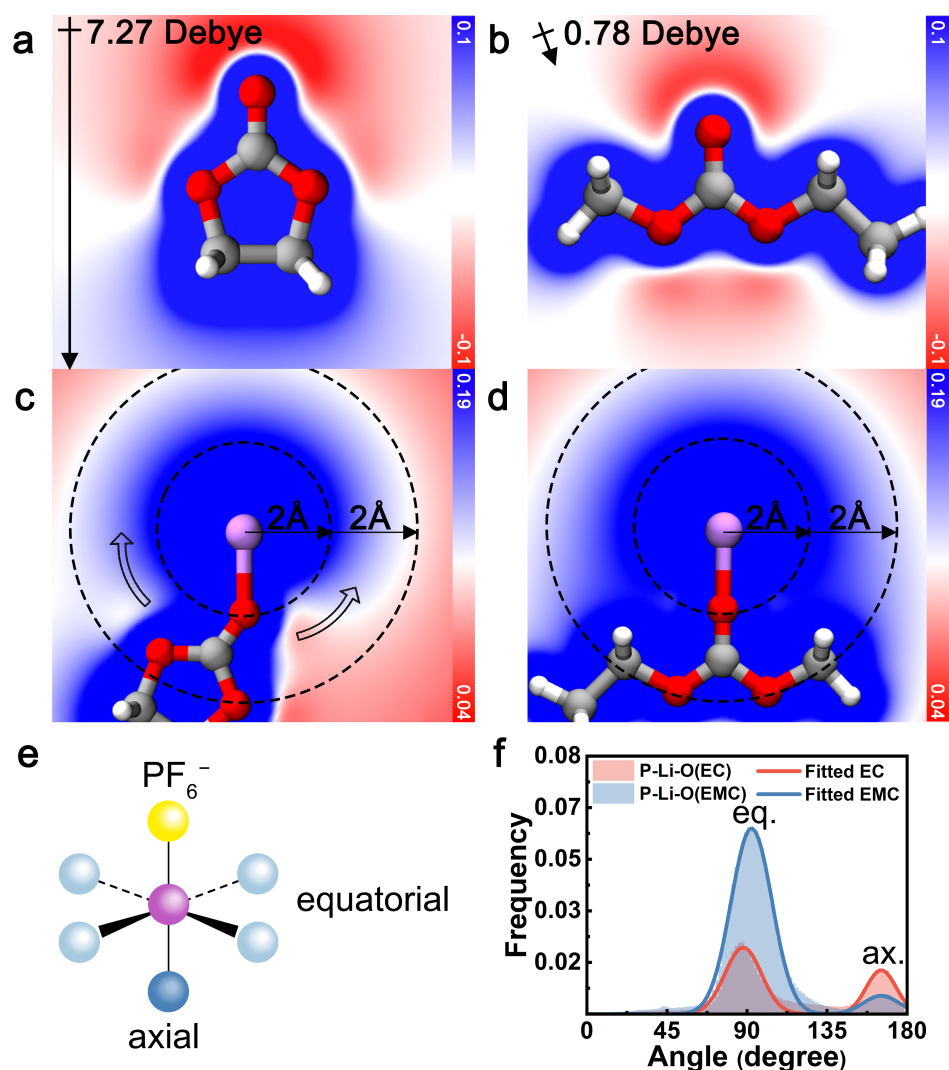
Figure 4.3 The electrostatic potential contour maps of (a) EC, (b) EMC, (c) Li$^+$ coordinated EC ([Li$^+$EC]), and (d) Li$^+$ coordinated EMC ([Li$^+$EMC]) calculated using quantum chemistry. The slice is across the carbonyl plane. Red, blue and white colors represent the least positive (or most negative), most positive, and intermediate electrostatic potential, respectively. The color bar shows the values of the electrostatic potential in volts. The directions and magnitudes of the net molecular dipole moments are shown for EC and EMC. The connections between atoms represent chemical bonding or Li$^+$ coordination. (e) An illustration of the octahedral coordination of Li$^+$ with equatorial (eq.) and axial (ax.) coordination sites with respect to PF$_6^-$ (yellow ball). The light blue and dark blue balls indicate the preferential sites for EMC and EC, respectively. (f) The calculated and fitted angle distribution of P-Li-O (P = P in PF$_6^-$, O = carbonyl O in EC and EMC) of CIP species.

charge of PF_6^- is identified as the origin of the exclusive relationship between EC and PF_6^-. As a measure of the interaction between charge and dipole, electrostatic potential analysis was conducted with contour maps across the carbonyl plane. As illustrated in Figure 4.3a, b, uncoordinated EC exhibits a large molecular polarization (7.27 Debye, calculated) while the dipole of EMC is mostly canceled out (0.78 Debye, calculated). When EC coordinates with Li^+ ([Li^+EC], Figure 4.3c), a gradient of electrostatic potential is yielded along the circumference direction around Li^+ (hollow arrow). In contrast, the electrostatic potential around EMC-coordinated Li^+ ([Li^+EMC]) is almost evenly distributed and more positive at the same radial distance (Figure 4.3d). A more negative electrostatic potential near [Li^+EC] indicates greater relative electrostatic repulsion between EC and PF_6^-, compared to [Li^+EMC]. To quantify this electrostatic interaction, we performed energy decomposition analysis based on absolutely localized molecular orbitals within an implicit solvent model (ALMO-EDA(solv)) [87] on the binding energy of [Li^+EC]$\ldots PF_6^-$ (E_{b1}) and [Li^+EMC]$\ldots$[PF_6^-] (E_{b2}), respectively (Appendix Figure B.7; ellipsis denotes the binding of two clusters). The difference in the attractive terms between E_{b1} and E_{b2} is found to be 63% contributed by the electrostatic interaction. (Appendix Figure B.8). This dominancy of the electrostatic term verifies the arguments that the exclusive relationship between EC and PF_6^- mainly originates from electrostatic repulsion. Interestingly, the repulsive interaction even regulates the angular distribution of coordinating species as manifested in MD trajectories (Figure 4.3e, f). Considering a model octahedral CIP solvation structure with four equatorial coordination sites and one axial coordination site with respect to PF_6^-, in an unbiased situation, the likelihood ratio of solvent molecules occupying the two types of sites is 4:1. By fitting the distribution of angle P-Li-O (P = P in PF_6^-, O = carbonyl O in EC and EMC) of CIP species with a binormal distribution, we observe a clear trend that the axial site is favored by EC, whereas EMC exhibits a higher probability for occupying the equatorial sites. The trend is consistent with the repulsive electrostatic interaction between EC and PF_6^- as elucidated by the quantum chemistry calculations. Note that PF_6^- can be either monodentate or bidentate, which leads to a deviation from 180° for the axial binding site.

The impact of the anion–solvent exchange mechanism on the electrochemical performance of electrolytes is two-fold. First, the exchange mechanism is likely to impact the SEI formation. When the electrolyte reacts with the anode surface to form the SEI, the reaction products depend on the starting reactants as well as their immediate solvation environment. The preferential substitution between EC and PF_6^- anion indicates a lower fraction of EC in solvation structures where Li^+ coordinates with PF_6^-. Meanwhile, for this small fraction of EC in CIPs and AGGs, it is likely that EC and PF_6^- are separated by a larger angle. In contrast, positively charged SSIPs contain more EC than the bulk average, which preferentially move to the anode surface due to electrostatic and concentration gradients. Therefore, the EC–PF_6^- exchange influences both the neighbor distance between EC and PF_6^- within a solvation structure as well as the distribution of solvation species near the anode surface, which in turn impacts the composition of starting reactants, the environment of intermediate fragments, and ultimately the final products of SEI formation reactions.

Secondly, the exchange mechanism enhances our understanding of salt dissociation and
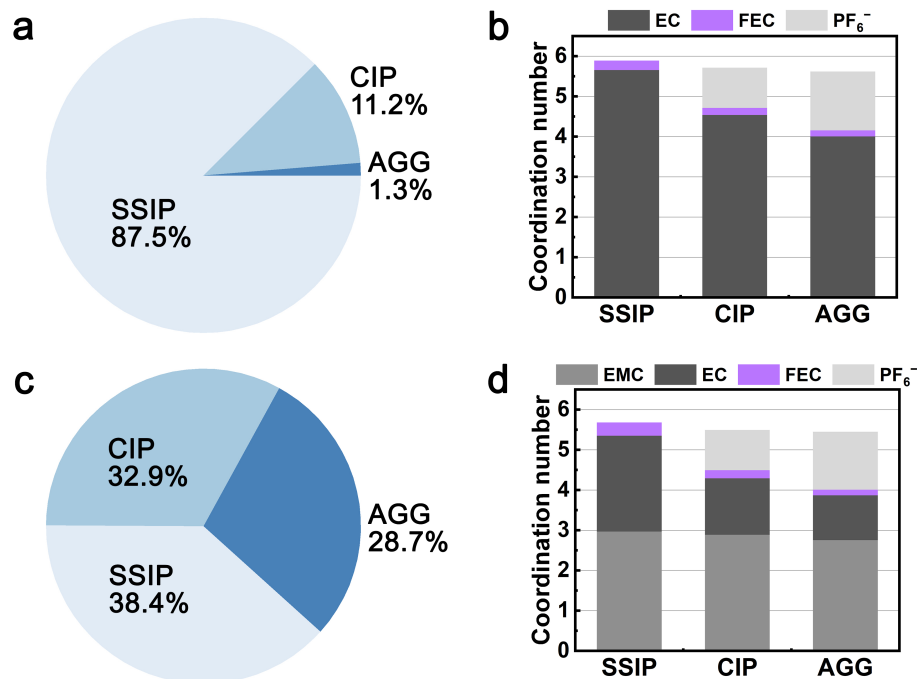
Figure 4.4 The population and species-specific coordination number of SSIP, CIP, and AGG in (a-b) the ECF electrolyte and (c-d) the GenF electrolyte.

ionic conduction phenomena. With the "exit-entry" mechanism, a free PF_6^- does not coordinate with Li^+ until an EC molecule exits the SSIP. Thus, the rate of ion pair formation is governed by the relatively long residence time of EC molecules in the Li^+ solvation shell (6.4 ns as calculated in section 4.6). In contrast, in the "entry-exit" mechanism PF_6^- may directly attack the solvation shell of an SSIP and associate with Li^+, similar to a nucleophilic S_N2 reaction. This identified mechanism may thus be significant in promoting the long-lived presence of SSIPs, which screen the electrostatic interaction between Li^+ and PF_6^- and enable uncorrelated cation and anion flux.

4.5 Solvation structure of the GenF and ECF electrolytes

The influence of the electrolyte additive on the solvation structure of electrolytes was studied. Two model electrolytes (ECF and GenF electrolyte) are created by adding 10 mol% of FEC to the EC-base and Gen2 electrolyte. As shown in Figure 4.4a, c, comparing with the EC-base and Gen2 electrolytes, the ECF and GenF electrolytes exhibit similar population distributions, despite that the SSIP ratio in the GenF electrolyte is slightly higher than that of Gen2. Likewise, in terms of the anion–solvent exchange behavior, electrolytes with
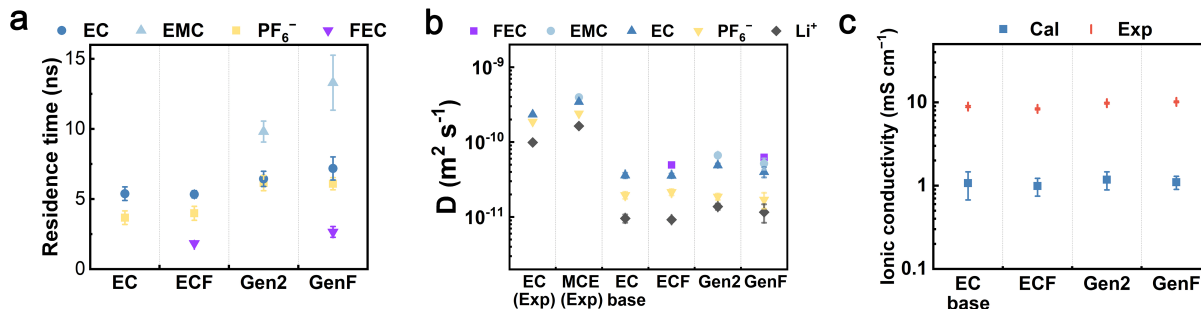
Figure 4.5 Transport properties of the EC-base, ECF, Gen2, and GenF electrolytes. The residence times (τ_{ij}) of EC-Li$^+$, EMC-Li$^+$, FEC-Li$_+$, and PF$_6^-$-Li$^+$ pairs in the EC-base, ECF, Gen2, and GenF electrolytes. (b) The calculated self-diffusion coefficients of electrolyte species (EC, EMC, FEC, PF$_6^-$, and Li$^+$) in the EC-base, ECF, Gen2, and GenF electrolytes. Experimental values for EC (1 M LiPF$_6$ in EC), and MCE (1 M LiPF$_6$ in EC:DEC 1:2 (mol.)) at 298 K are taken from the literature [139]. (c) The experimental (Exp) and calculated (Cal) ionic conductivity at 298 K.

FEC exhibit a similar trend as their base electrolytes (Figure 4.4b, d). The average Li$^+$ coordination number with EMC remains about 3 for all the species, while the FEC coordination number to Li$^+$ decreases along with EC when forming CIP and AGG in the GenF electrolyte. We hypothesize that the large dipole moment of FEC (6.44 Debye, calculated), which is comparable with that of the structurally analogous EC, is responsible for a similar repulsive interaction with PF$_6^-$ as compared to EC. Moreover, fluorination is reported to cause large decreases in the solvating ability of fluorinated carbonate [8]. On average, FEC exhibits a coordination number of 0.23 in both ECF and GenF electrolytes, corresponding to an EC:FEC molar ratio and an EC:EMC:FEC molar ratio of 24:1 and 7:12:1 in the solvation shell. This less than 10% of FEC in the Li$^+$ first solvation shell signifies its weaker solvating ability, compared to EC and EMC, consistent with experimental observations [8, 192]. However, the fact that still a considerable portion (23%, if assuming single FEC coordination) of Li$^+$ are coordinated with at least one FEC, is crucial for the reduction behavior of electrolytes with the FEC additive, as discussed below.

4.6 Transport properties

To evaluate the properties of the four model electrolytes, we consider not only the coordination environments but also the transport properties governing the Li$^+$ diffusion and ionic conduction. In order to quantify the average time length of ion association, the residence times (τ_{ij}) of Li$^+$-EC, Li$^+$-EMC, Li$^+$-FEC, and Li$^+$-PF$_6^-$ in the four model electrolytes were computed by fitting the pair lifetime correlation function (Figure 4.5a). The residence times of Li$^+$-solvent pairs decrease in the order of EMC, EC, and FEC. A similar trend was found in previous theoretical calculations that DMC exhibits a longer residence time over EC with

respect to Li$^+$ [171]. Notably, the fitted RESP partial charges on the carbonyl oxygen of each solvent molecule decrease in the same order. We surmise that the partial charge of the coordinating atom rather than the donor number of the coordinating solvent is the decisive factor of the kinetic barrier of desolvation, which further determines the residence times. The residence times of Li$^+$-PF$_6^-$ in the Gen2 and GenF electrolytes are about 6 ns while those in EC and ECF electrolytes are less than 4 ns. The trend indicates that the Li$^+$-PF$_6^-$ pair coordinates with each other for a longer period of time in the presence of linear carbonates. Therefore, our solvation structure and residence time analysis have demonstrated that, with linear carbonates, the coordinated species (CIP and AGG) are more favored both spatially and temporally.

Furthermore, the self-diffusion coefficients were calculated using the slope of the mean square displacement (MSD) and compared to experiments (Figure 4.5b; Appendix Figure B.3a). In contrast to the EC-base and ECF electrolytes, MCEs (the Gen2 and GenF electrolytes) exhibit a greater self-diffusion coefficient for all species, as linear carbonates are less viscous. While it is well-known that the non-polarizable force field employed here underestimates the diffusivity, the calculated self-diffusion coefficients are in fair agreement with the experimental trends [139]. It should be noted that scaling the point charges in non-polarizable force fields is an effective approach to account for the electronic polarizations that screen solvent–ion and ion–ion interactions [175, 193, 194]. For a mixed carbonate electrolyte (e.g., Gen2), MD simulations using a non-polarizable force field can obtain a similar diffusivity and ionic conductivity as experiments by scaling the default ionic charges (± 1) of Li$^+$ and PF$_6^-$ with a factor of 0.8, as demonstrated in a recent work [195]. A less used approach is to scale the point charge of solvent molecules to modulate the solvent polarity [153, 196].

Thus far, we have shown that MCEs exhibit a higher diffusivity, while the EC-base and ECF electrolytes exhibit a higher ion dissociation rate and a higher ratio of ionic conducting species.

Based on the above understanding of the ion solvation and diffusion, the ionic conductivities were rigorously computed using GK relations and experimentally measured using a conductivity meter, as shown in Figure 4.5c, Appendix Figure B.3b. All four electrolytes exhibit similar calculated ionic conductivity values, within an order of magnitude. Interestingly, the significantly higher salt association of the Gen2 electrolyte does not lead to significantly lower ionic conductivity, which is attributed to the improved viscosity and self-diffusion properties. This trend is consistent with our experimentally obtained values (9.8 mS cm^{-1} for Gen2, 8.9 mS cm^{-1} for EC-base). In contrast, conventional ionic conductivity calculations using the Nernst–Einstein equation overestimate the ionic conductivity of the Gen2 and GenF electrolyte by more than 40% (Appendix Figure B.9). Hence, for highly associated mixed carbonate electrolytes, a rigorous calculation using Green–Kubo relations is important for obtaining a correct trend of the ionic conductivity. Notably, the inclusion of linear carbonates is essential for the practical operation of batteries at low temperature [7]. Furthermore, as shown in Figure 4.5b, the addition of 10% FEC slightly decreases the self-diffusion coefficients of other species, due to the high viscosity of FEC (4.1 cP, 298 K),

Table 4.2 The calculated (Cal) and experimentally (Exp) measured reduction potentials vs $Li^+/Li(s)$ of Li^+ coordinated solvents, in Volt. The parentheses with a minor sign denote the reduced molecule.

Reduction reaction	Potential (V vs Li^+/Li)	
	Cal	Exp
Li^+-EMC $+ e^- \rightarrow Li^+$-(EMC)$^-$	0.45	0.45 [157]
Li^+-EC $+ e^- \rightarrow Li^+$-(EC)$^-$	0.62	0.75 [155]
Li^+-(EC)$_3$(EMC)$_3$ $+ e^- \rightarrow Li^+$-(EC)$^-$(EC)$_2$(EMC)$_3$	0.64	
Li^+-FEC $+ e^- \rightarrow Li^+$-(FEC)$^-$	0.97	1.1 [199]
Li^+-(EC)$_2$(EMC)$_3$(FEC) $+ e^- \rightarrow Li^+$-(EC)$_2$(EMC)$_3$(FEC)$^-$	0.99	

as compared with EC (1.9 cP, 313 K) and EMC (0.65 cP, 298 K) [134, 197]. As a result, the ionic conductivity of the ECF is slightly lower than that of the EC-base electrolyte for both experimental and calculated results. In contrast, the ionic conductivities of the Gen2 and GenF electrolytes are almost equal, on account of the slightly higher SSIP ratio in the GenF electrolyte that helps compensate for the decrease in diffusivity. The observation agrees with previous experimental results that the ionic conductivity of 1 M LiPF$_6$ 1:1:3 (vol.%) EC/PC/EMC remains similar when adding 2 vol% FEC at room temperature [198].

4.7 Reduction behavior of each solvent ingredient

Given that the reduction reactions of electrolytes regulate the anode SEI formation and further influence the cycling performance of batteries, the reduction behavior of electrolytes was investigated by quantum chemical calculations. The initial step of reduction reactions and the corresponding reduction potentials of single EC, EMC, and FEC coordinated Li$^+$ structures, as well as two full solvation structures obtained from the MD trajectory, were computed and compared to experiments (Table 4.2; Appendix Figure B.6). The reduction potential decreases with the order of FEC, EC, and EMC, in agreement with the reported experimental results [155, 157, 199] and previous theoretical calculations [118]. Even as an additive (10%), FEC coordinates with Li$^+$ (Figure 4.4) and exhibits a high reduction potential (0.3 V higher than EC). Thus, FEC will be preferentially reduced in the early SEI formation using ECF and GenF in full cells, setting the stage for further SEI formation reactions, aging, and anode passivation [163]. Moreover, FEC is expected to improve the SEI composition, through increased production of LiF and oligomeric components derived by FEC reduction [44, 100]. Even though the additive may slightly affect the conductivity as discussed above, the overall effect of FEC additive is beneficial for the cycling performance and capacity retention, especially for Li metal anode [42] and Si anode applications [5]. Furthermore, as noted by Horowitz et al. [200] and Shi et al. [90], for reduction reactions

specifically at the electrolyte–electrode interface, the interaction of the solvated species with the electrodes is another important factor governing the reduction behavior of electrolytes.

The interaction between solvated species with Li metal and silicon anodes is especially sensitive to the surface conditions of the specific materials. The electrochemical and mechanical evolution of the Li metal surface is a highly complex, out-of-equilibrium reaction cascade, where the resulting composite surface film can reduce electronic charge transfer to the electrolyte [201], and its inorganic components including Li_2O, Li_2CO_3, LiOH, Li_2S, and LiF, along with organic components depending on manufacturing and storage conditions are all believed to influence the SEI layer composition and functionality [201, 202]. Similarly, almost all silicon surfaces exhibit a native oxide or sub-oxide layer that reacts irreversibly during the initial electrochemical cycles [203]. While the reduction of linear carbonate is believed to be fully suppressed by EC on graphite anode [26, 204], in situ spectroscopic experiments have shown evidence of preferential reduction of linear carbonates (e.g., DMC) on the native silicon oxide film of non-lithiated silicon anode [90]. Balbuena et al. [110, 112] have found that the reduction mechanism of EC and FEC is highly dependent on the surface termination of the Si surface, as well as the degree of lithiation of the surface. Moreover, it is reported that FEC exhibits a higher affinity towards the silicon surface than EC, and forms an ordered, up-right orientation, which may promote SEI formation and Li diffusion [145, 146]. Most recently, artificial surface coating with the appropriate binder [205], oxide layer [206], and Mg metal [207] have been used to alter the interfacial interactions and reactions between the Si anode and electrolytes for achieving a stable SEI that minimizes side reactions and sustains efficient cycling. Finally, water contamination has been reported to cause detrimental parasitic reactions that affect the formation, evolution, and properties of the SEI [208]. In addition, the hydrolysis of $LiPF_6$ creates hydrofluoric acid, leading to a pitted and inhomogeneous SEI structure [209]. Therefore, we note the importance of considering specific surface conditions as well as possible impurities when investigating the interfacial reactions between anodes and electrolytes.

4.8 Conclusions

In summary, the solvation structure, transport properties, and reduction behavior of four prototype electrolytes (EC-base, ECF, Gen2, and GenF) was investigated using classical MD simulations, quantum chemistry, and transport property measurements. While the $LiPF_6$ salt in the EC-base electrolyte is mostly dissociated, the Gen2 electrolytes exhibit a much higher degree of ion association (>30% CIP, >30% AGG). Interestingly, and non-intuitively, in the Gen2 electrolyte, the coordination number of EC with Li^+ decreases when PF_6^- enters the first solvation shell. We here identify electrostatic repulsion between the highly polarizable EC and the negative charged anion PF_6^-, as responsible for the phenomenon. We also reveal an anion–solvent exchange mechanism as an "entry-exit" type, providing a dynamic perspective of ion transport in electrolytes. Furthermore, in contrast to the EC-base electrolyte, the Gen2 electrolyte exhibits greater self-diffusion coefficients, due to the lower

viscosity of the linear carbonates. Therefore, although the Gen2 electrolyte exhibits more aggregates and bulky conductive species, the overall ionic conductivities of the Gen2 and EC-base electrolyte are very similar, as verified by experimental measurements. A considerable portion of the FEC additive in the ECF and GenF electrolyte is found to coordinate with Li^+ in the first solvation shell, with minor impact on the transport properties. Finally, the reduction potentials of Li^+ coordinated solvent molecules are found to decrease in the order of FEC, EC, and EMC. The preferential reduction of the FEC additive is deemed beneficial for the early onset passivation of the anode surface and facilitates an improved composition of SEI. We believe our modeling of mixed carbonate electrolytes elucidates the atomistic origin of energy-storage relevant properties of this class of commercially relevant battery electrolytes, and provides a paradigm of computational property evaluation in novel electrolyte design.

Chapter 5

The Modeling of Novel Solid-State Electrolytes Based on Metal–Organic Frameworks

5.1   Introduction

The novel intrinsically anionic Metal–Organic Frameworks (MOFs) with a superior ionic conduction performance has opened up a new possibility for the development of Solid-State Electrolytes (SSEs). As introduced in Chapter 1, similar to the concept of polyelectrolytes, solvent-infused MOFs was demonstrated to exhibit superior ionic conductivity, high Li^+ transference number, and low interfacial resistance, but with three dimensional pore system and highly connected crystalline structure compared to polymers. Given the vast materials space that results from linking inorganic nodes and organic ligands [210], it is important to develop theoretical methods that can predict the transport properties of MOFs to support the experimental synthesis, characterization, and testing efforts. Classical molecular dynamics simulations have shown excellent results in modeling the solvation and transport properties of traditional liquid electrolytes [195, 211] as well as diffusion and adsorption properties of MOFs [212, 213]. The universal force field (UFF) [214] is frequently used to describe the interaction of guest molecules within the MOFs, where the non-bonded interactions are described by a Lennard-Jones potential and Coulombic interactions. However, because the chemical environment of MOFs is very different from those considered in the development of UFF, the generic atomic partial charges in UFF cannot fully reflect the local Coulombic electrostatics of MOFs, especially for the intrinsically anionic MOFs, such as MOF-688, where the local charge distribution plays a crucial role for ionic conduction. In this chapter, we substitute the default atomic partial charges of UFF using RESP charges [131, 132] fitted by accurate quantum chemistry calculations, which is reported to effectively reproduce the local electrostatics [211].

This chapter aims to develop a very first theoretical model for evaluating the ionic con-

duction mechanism of MOF-based SSEs and suggest guidance for possible improvements. MOFs with two types of center metal ions, MOF-688(Mn) and MOF-688(Al) are considered. Classical molecular dynamics in conjunction with the grand canonical Monte Carlo method [215] are utilized to model the corresponding diffusion and ionic conduction phenomena in the two materials. The ionic conductivity is calculated using equations based on different levels of approximation of the ion diffusion behavior and compared with experimental results, from which the main ionic conduction mechanism is identified. Detailed static and dynamic solvation structure information is obtained to help interpret the Li^+ motion with a high spatial and temporal resolution. Moreover, the relationship between the charge distribution on the charged polyoxometalates (POMs, building blocks of the MOF-688) and the Li^+ distribution in the SSE is visualized to fully elucidate the Li^+ conduction behavior. Finally, a rationally designed MOF-688(one-fold) material is proposed that is expected to achieve nearly 10 times better performance than the MOF-688.

5.2   The conduction mechanism of MOF-688

Molecular dynamics (MD) and grand canonical Monte Carlo (GCMC) simulations were carried out with the LAMMPS (Large Scale Atomic/Molecular Massively Parallel Simulator) software package [123]. The topology of MOF-688, obtained from single crystal X-ray diffraction (SXRD), was used as the initial structure to build a supercell containing 12 POM clusters, denoted as MOF-688(Mn). In parallel, a MOF-688(Al) structure where Mn^{3+} is substituted by Al^{3+} was built to investigate the influence of the POM center metal ion on the ionic conduction. The nonpolarizable UFF [214] was utilized to parameterize the bonded and van der Waals interactions. Partial charges of the intrinsically anionic frameworks were fitted from first principles with B3LYP/6-31+G(d,p)//B3LYP/aug-cc-pvdz [129, 216, 217] level of theory for the organic linker and oxygen, manganese in the POM cluster, and B3LYP/LANL2TZ(f)//B3LYP/LANL2TZ(f) [218, 219] level of theory for molybdenum in the POM cluster, respectively. The fitted partial charges and the unit charge of Li^+ (+1) were then scaled by a factor of $\epsilon = 0.6$ to account for the fact that solvent–ion and ion–ion interactions are typically overestimated in nonpolarizable force fields [175, 193, 194]. Hybrid GCMC and MD simulations were performed to insert the propylene carbonate (PC) solvent into the pores of the MOF by exchanging molecules with an imaginary reservoir of PC. After at least 200 ns equilibration, the POM:PC ratio converged to 16:170. The obtained PC-infused structure was then equilibrated for 2 ns in the isothermal-isobaric ensemble (T = 298 K, P = 1 bar) using the Parrinello–Rahman barostat followed with an annealing process. Finally, 50 ns production runs within the canonical ensemble (NVT) under a Nosé-Hoover thermostat were performed to obtain the Li^+ transport properties. Independent duplicate production runs were undertaken for both the MOF-688(Mn) and MOF-688(Al), and statistics of the three duplicates were collected.

By analyzing the MD trajectories over a few tens of nanoseconds, we observe three different types of Li^+ motion as schematically visualized in Figure 5.1: (1) Li^+ hopping on
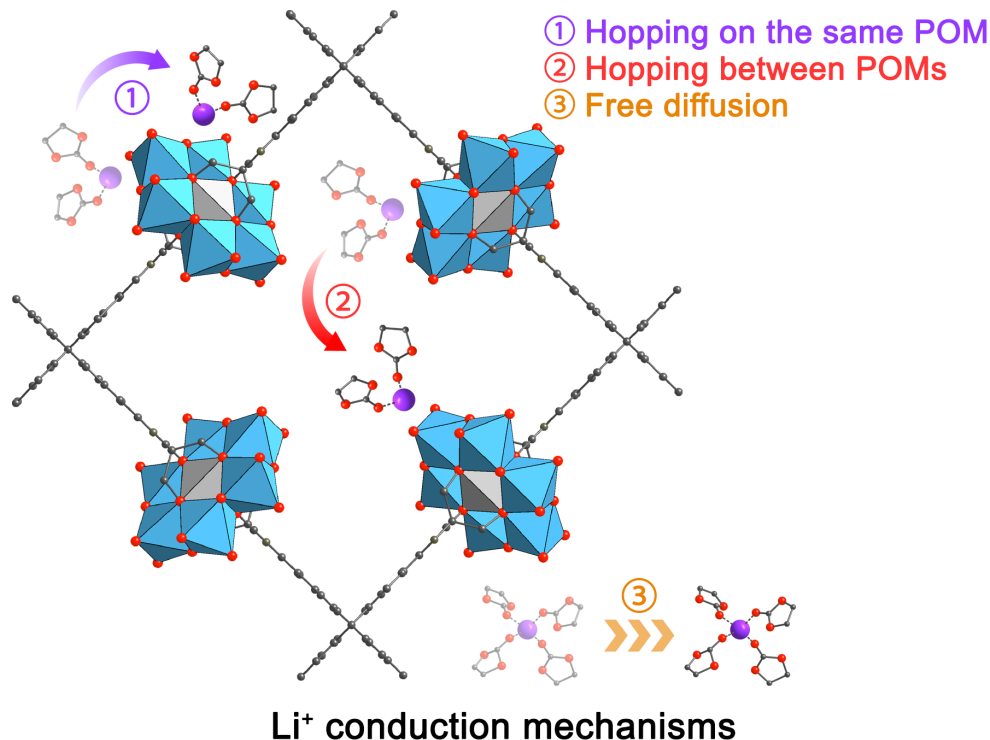
Figure 5.1 Three possible mechanisms of Li$^+$ motion in the MOF-688 based SSE.

the same POM cluster, which corresponds to the hopping event when Li$^+$ jumps from one binding site (outmost O atoms on the POM cluster) to another; (2) Li$^+$ hopping between POM clusters when Li leaves the binding site of a POM cluster and binds to another POM cluster; and (3) freely solvated Li$^+$ diffusion, where the Li$^+$ is only coordinated by the PC solvent and forms solvent-separated Li$^+$ that can freely diffuse in the bulk solvent.

To identify the ionic conduction mechanism of the two model materials, MOF-688(Al) and MOF-688(Mn), we calculate the ionic conductivity using different levels of approximation. First, we rigorously compute the conductivity using the Green–Kubo (GK) relations:

$$\sigma_{GK} = \frac{1}{6k_BTV} \lim_{t\to\infty} \frac{\mathrm{d}}{\mathrm{d}t} \langle \sum_{i=1}^{N} \sum_{j=1}^{N} q_iq_j[\mathbf{r}_i(t) - \mathbf{r}_i(t)] \cdot [\mathbf{r}_i(t) - \mathbf{r}_i(t)] \rangle, \qquad (5.1)$$

where F is the Faraday constant, k_B is the Boltzmann constant, T is temperature, V is the cell volume, q_i is the charge of species i, $\mathbf{r}_i(t)$ is the coordinates of species i at time t. The calculated conductivity of MOF-688(Mn) at 298 K (Figure 5.2c) and as a function of temperature (Appendix Figure C.1) show excellent agreement with the experimental value [61], validating that the molecular model is reasonable for quantitatively studying transport phenomena of MOF-based SSEs. Moreover, MOF-688(Al) exhibits a slightly lower ionic conductivity than MOF-688(Mn), however, the difference is within the error range. This observation indicates that changing the type of center metal ions is unlikely to efficiently
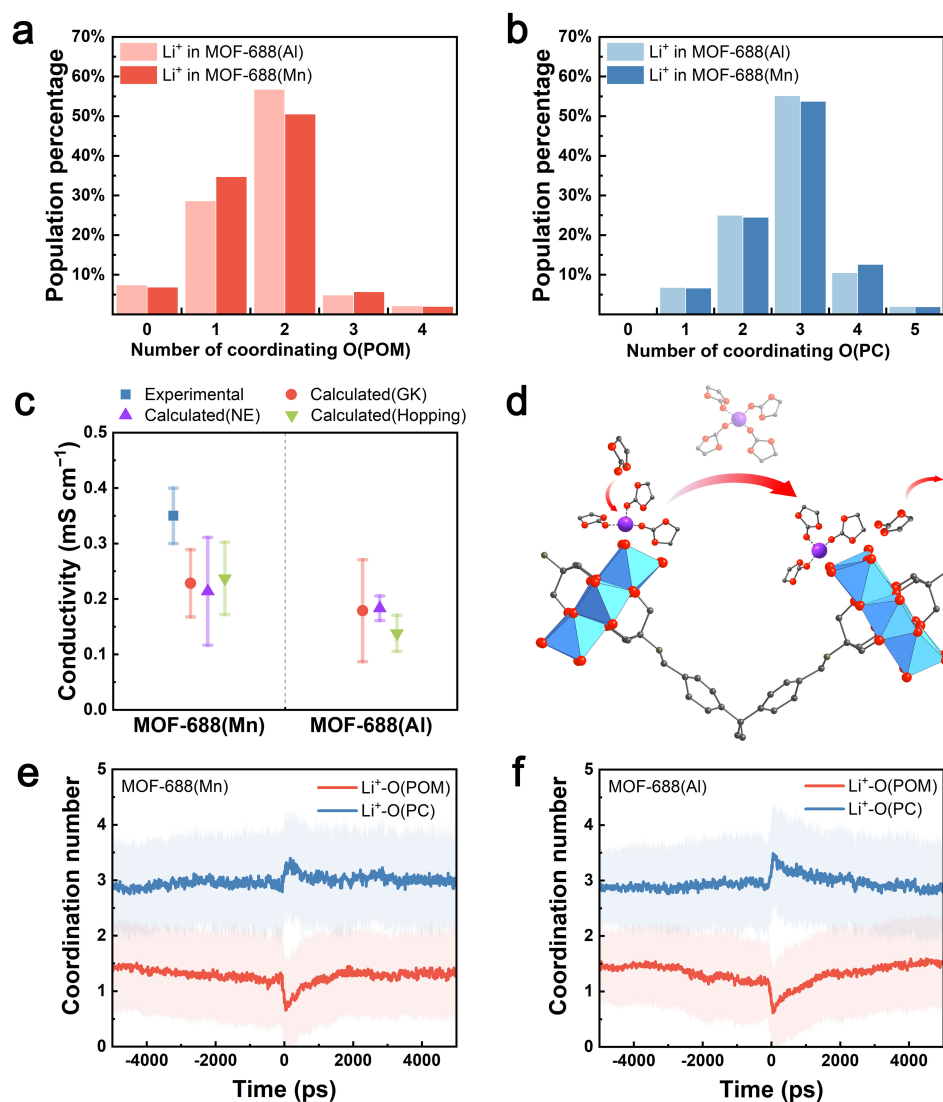
Figure 5.2 The conduction mechanism of MOF-688. The coordination number of (a) Li^+-O(POM), and (b) Li^+-O(PC) in MOF-688(Al) and MOF-688(Mn). (c) The ionic conductivities of MOF-688(Al) and MOF-688(Mn) from experimental measurements [61], and theoretical calculation using Green–Kubo relations (GK), Nearst–Einstein relations (NE), and simple hopping model (hopping). (d) An illustration of the solvent-assisted hopping between POM clusters. The evolution of the coordination number of Li^+-O(POM) and Li^+-O(PC) before and after hopping events in (e) MOF-688(Al) and (f) MOF-688(Mn). The time of each hopping event happens is set as 0 ps. The coordination number profile is averaged over all hopping events in each simulation. The light-colored area denotes the extent of standard deviation.

tune the ion conduction performance. Further analysis of MD trajectories suggests that the minor difference between the two model materials may be attributed to a slightly weaker interaction between Li$^+$ and the POM cluster in the MOF-688(Mn) (Figure 5.2a and 5.2b). With a slightly smaller fitted atomic charge on the outmost O atom of the POM cluster (O(POM)) in MOF-688(Mn), a higher percentage of Li$^+$ ions in MOF-688(Mn) are found to coordinate to one O(POM) than that in MOF-688(Al). Meanwhile, more Li$^+$ ions in MOF-688(Mn) are coordinated by 4 PC solvent molecules than in MOF-688(Al). This trend suggests that the Li$^+$ in MOF-688(Mn) has a slightly weaker interaction with O(POM), and is better solvated by PC. We note that in both MOF-688(Mn) and MOF-688(Al), only 7% Li$^+$ ions are freely solvated, demonstrating that, at any given time, most Li$^+$ ions are tethered to the framework. It is further found that the self-diffusion coefficients of tethered and freely solvated Li$^+$ are similar. Hence, the diffusion of freely solvated Li$^+$ is excluded from the major conduction mechanism.

Next, we calculate the ionic conductivity by assuming that the ionic conduction is mostly contributed to the uncorrelated (self) diffusion of Li$^+$, and the intrinsically anionic frameworks are treated as fixed. With the assumption, ionic conduction can be related to the diffusion coefficient using the Nernst–Einstein equation (NE) from the diffusivity of Li$^+$:

$$\sigma_{NE} = \frac{F^2}{RT}(c_+ q_+{}^2 D_+ + c_- q_-{}^2 D_-) = \frac{F^2}{RT}c_+ D_+, \tag{5.2}$$

where σ_{NE} is the ionic conductivity, c_+ and c_- are the bulk molar concentrations of the cation and anion, q_+ and q_- are the charge of the cation and anion, and D_+ and D_- are the self-diffusion coefficients of the cation and anion. D_- is assumed to be 0. D_+ for Li$^+$ can be obtained by calculating the slope of the mean square displacement (MSD, $\mathbf{r}^2(t)$) over time using the Stokes–Einstein relation [73]:

$$D_+ = \frac{1}{6}\lim_{t\to\infty}\frac{\mathrm{d}}{\mathrm{d}t}\langle\mathbf{r}^2(t)\rangle, \tag{5.3}$$

where $\mathbf{r}(t)$ is the position vector of Li$^+$ at time t. The computed NE conductivity is in fair agreement with the GK conductivity. Hence, we argue that the underlying assumption arguably holds that the conductivity is mostly contributed by the self-diffusion of Li$^+$, in agreement with the reported high transference number of MOF-688 ($t_{Li+} = 0.87$).

Finally, we calculate the ionic conductivity with a simple hopping model. The uncorrelated individual ion hops can be described by a random-walk model [220]. The hopping diffusion coefficient D under the theoretical framework of random walk can be expressed as

$$D = \frac{\Gamma a^2}{b} \tag{5.4}$$

where Γ is the hopping frequency of successful jumps, a is the hopping distance between two neighboring binding sites of Li$^+$, and b is a geometry factor of 2, 4, or 6 for one-, two-, or three-dimensional diffusion, respectively. Li$^+$ within a given cutoff distance of the anionic framework is considered tethered. The cutoff distance is chosen as half of the

averaged distance between the centers neighboring POM clusters. Using the cutoff distance as a criterion, a successful hop is defined as one Li^+ moves beyond the cutoff distance of a previously tethered POM cluster and binds to another POM cluster. The hopping distance was obtained by averaging the distance between neighboring binding sites in hopping events. Thus, the diffusion coefficient can be estimated based on the hopping frequency and hopping distance. Incorporating the hopping diffusion coefficient into equation 5.2, we obtain the hopping conductivity. While the calculation utilizes a very simple model, it yields fair agreement with the other two models, suggesting that Li^+ hopping between POM clusters dominates the Li^+ diffusion.

The evolution of the Li^+ solvation sheath during Li^+ hopping further reveals the solvent effect on the process. By inspecting the averaged coordination numbers of O(PC) and O(POM) before and after each hopping event (set as 0 ps), we observe discrete changes of the coordination numbers of both O(PC) and O(POM) (Figure 5.2e and 5.2f). During hopping, the Li^+ exhibits a decrease in the O(POM) coordination number where the Li^+ no longer binds to the previous binding sites and has not reestablished binding with another POM cluster. Simultaneously, the average coordination number of PC increases from 3 to 3.5 for both MOF-688(Mn) and MOF-688(Al) overlaid with a standard deviation of ± 0.8. The direct involvement of the excess PC suggests that the main mechanism of the Li^+ ionic conduction is the solvent-assisted hopping between POM clusters (Figure 5.2d). In the following 500-1000 ps after hopping, as Li^+ ions are gradually tethered to the framework and the excess PC leaves the Li^+ solvation sheath, the coordination numbers of O(PC) and O(POM) are restored to the bulk average. The short residence time of the excess PC indicates that the PC molecule plays an assisting role rather than facilitating solvent-separated Li^+ solvation structures that freely diffuse in the bulk solvent.

5.3 The relation between the charge distribution and Li^+ density

As aforementioned, we note that tuning the local charge distribution on the POM cluster can tailor the interaction between Li^+ and the framework, which may help modify the Li^+ motion behavior. However, changing the center metal ion from Mn^{3+} to Al^{3+} was found not effective in altering the total ionic conductivity of the material. Therefore, there is a need to further examine the influence of changing the center metal ion on the charge distribution at the POM surface. Here, we calculated the electrostatic potential surface of the MOF-688(Mn) (Figure 5.3a and 5.3b) and MOF-688(Al) (Appendix Figure C.2 and C.3) POM clusters using quantum chemistry as a measure of the strength of the Coulombic interaction between the POM cluster and Li^+. The electrostatic potential distribution of MOF-688(Mn) is almost identical to that of MOF-688(Al), indicating that the influence of changing the center metal ion with the same charge to the POM surface charge distribution is minor. The surface area with the lowest electrostatic potential is of particular interest.
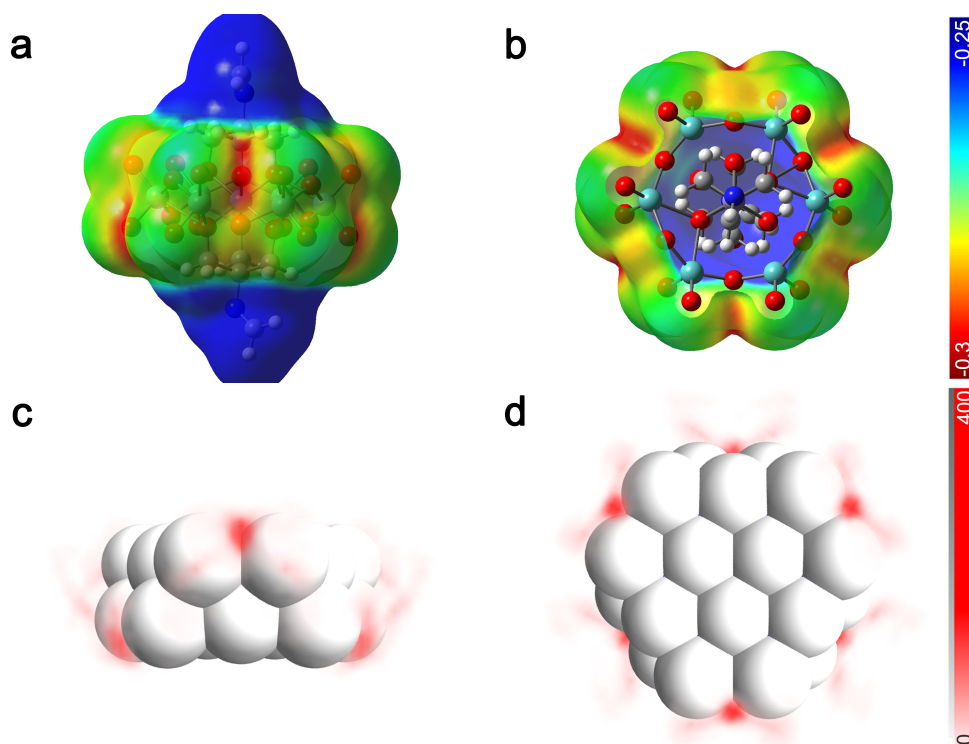
Figure 5.3 The charge and Li$^+$ distribution on the MOF-688(Mn) POM surface. (a) Front and (b) top view of the electrostatic potential (ESP) surface of the MOF-688(Mn) POM cluster. The color bar shows the values of the electrostatic potential in volts. (c) Front and (d) top view of the Li$^+$ density plot on the MOF-688(Mn) POM surface. White balls denote the O atoms of the POM cluster. The color bar shows the transparency and Li$^+$ number count from 100,000 randomly sampled coordinates during the MD simulation. The density plot uses a 8 Å × 8 Å × 5 Å mesh with each mesh division 0.2 Å equally spaced.

The sites between the neighboring regions of two MoO$_4$ moieties exhibit the most negative electrostatic potential. To validate if a lower electrostatic potential leads to a stronger interaction with Li$^+$, the Li$^+$ density distribution around the MOF-688(Mn) POM cluster was computed and plotted. Figure 5.3c and 5.3d show that the spatial distribution of Li$^+$ coincides well with the electrostatic potential distribution. Remarkably, the site with the lowest electrostatic potential exhibits the highest Li$^+$ density, suggesting that Li$^+$ is more likely to bind to sites with a lower electrostatic potential. The trend also indicates that the electrostatic term is dominant in the interaction between Li and the POM cluster, which further determines the most probable binding sites of Li. In addition, Li$^+$ can occasionally be monodentately-coordinated by one O as observed in the density plot.

The revealed correlation between the charge distribution and Li$^+$ distribution has important implications for the rational design of MOF-based SSEs. With a larger amount of charge immobilized on the intrinsically anionic frameworks, more Li$^+$ can be incorporated
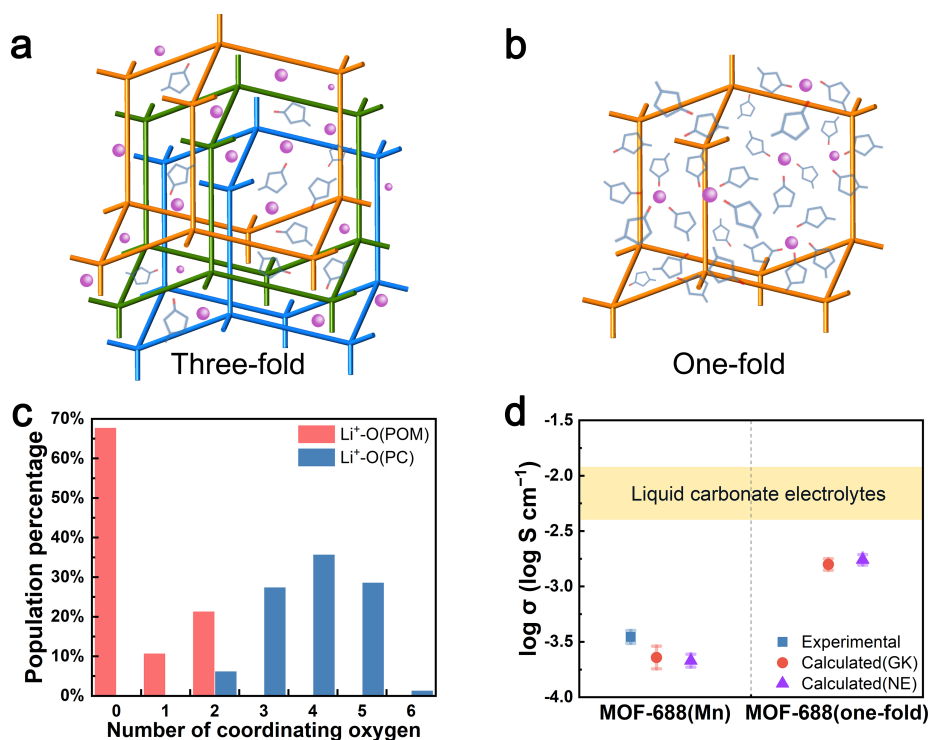
Figure 5.4 One-fold MOF-688 design. (a) An illustration of the realized MOF-688 solid-state electrolyte material with a three-fold interpenetrated structure. (b) An illustration of the proposed MOF-688(one-fold) solid-state electrolyte material with a one-fold inter-penetrated structure. (c) The coordination number of Li^+-O(POM), and Li^+-O(PC) in MOF-688(one-fold). (d) A comparison of the ionic conductivities of MOF-688(Mn), MOF-688(one-fold), and liquid carbonate electrolytes. The yellow area shows the lower and upper bound of the ionic conductivity of conventional liquid carbonate electrolytes.

into the SSE, providing more ionic conductive species. However, as charge density increases, the total ionic strength significantly increases. As a result, the limited amount of PC in pores cannot fully screen the electrostatic interaction between Li and POM, which may lead to severe aggregation between Li and the framework, decreasing the Li^+ mobility and ionic conductivity. In addition, we surmise that more distributed local charges on the POM cluster are expected to facilitate a weak binding with Li^+ and to enhance Li^+ motion. If the excess charge on the POM cluster is too localized, the framework may exhibit stronger confinement of Li^+, thereby impeding the Li^+ transport.

5.4 Novel one-fold MOF-688 design

While the framework electrostatics is crucial to the Li^+ distribution, we note that the solvent is another important factor regulating the Coulombic interaction. In the MOF-based SSE,

the solvent participates in the Li^+ solvation, dissociating Li^+ from the intrinsically anionic frameworks, and making Li^+ motion less correlated to the frameworks due to electrostatic screening [221]. To further understand the influence of the solvent content and pore volume on the ionic conduction, it is necessary to quantitatively measure the amount of PC and its ratio to the amount of Li^+. The apparent Li^+ concentration in MOF-688(Mn) is computed to be 2.03 mol L^{-1}. By considering the Li:PC ratio (1:3.54), the effective concentration that measures the Li concentration in the pore volume is estimated to be > 2.6 mol L^{-1} [222]. The high Li:PC ratio and the high effective concentration suggest a very high ionic strength in the material bulk phase. This low content of PC is mainly due to the limited pore volume resulted from the highly interpenetrated frameworks (Figure 5.4a). Interpenetration is a fundamental entanglement of MOFs, where two or more independent networks coexist in the same lattice [223]. The presence of such interpenetrating networks greatly reduces the pore size and thus the available space for solvents within the MOFs [224]. Therefore, we propose that decreasing the degree of interpenetration may be an effective approach to increase the pore volume and hence the amount of available PC solvent in the pores, thereby decrease the viscosity and ionic strength. To corroborate the hypothetical design, we modeled a MOF-688(one-fold) structure (Figure 5.4b) which is a non-interpenetrated derivative of MOF-688(Mn) with a one-fold structure. After the same GCMC equilibration process, a Li:PC ratio of 1:14.8 is obtained. The apparent and effective Li^+ concentrations are both 0.7 mol L^{-1}, similar to the common 1.0 mol L^{-1} concentration of conventional liquid electrolytes. Further analysis of the solvation structure reveals that more than 60% Li^+ ions are fully solvated by PC. The boost in solvent-separated Li^+ is especially favorable for the uncorrelated Li^+ diffusion in electrolytes [211]. Using the same methods, the GK and NE conductivities of MOF-688(one-fold) are calculated to be 1.58 mS cm^{-1} and 1.74 mS cm^{-1}, respectively. The theoretical prediction is nearly one order of magnitude higher than the conductivity of the state-of-art MOF-688(Mn) and approaches the lower bound of the conductivity range of conventional liquid electrolytes. Furthermore, the introduction of more PC leads to a different conduction mechanism of the hypothetical MOF-688(one-fold) from that of MOF-688(Mn). The specific contributions from the tethered and freely solvated Li^+ to the total ionic conductivity were calculated using the NE equation and the self-diffusion coefficients of the Li^+ in the two states. The obtained values are 0.71 and 1.24 mS cm^{-1} for tethered and freely solvated Li^+, respectively. Therefore, despite the minor discrepancy of their sum to the total NE conductivity due to different statistical treatment, the ionic conduction in MOF-688(one-fold) can be mainly attributed to the freely solvated Li^+ diffusion, facilitating a different ionic conduction mechanism with significantly improved performance. To actually synthesize MOF-688(one-fold) which has a much larger pore size than MOF-688(Mn), a very large (at least larger than TBA^+) and appropriately matching template cation is needed to aid the self-assembly of the organic and inorganic building blocks. We envision that screening methods based on first-principles calculations [225] and machine learning [226] may help identify suitable template candidates.

5.5   Conclusions

To summarize, we have investigated the ionic conduction mechanism of MOF-688 and its derivatives using classical molecular dynamics, grand canonical Monte Carlo, and quantum chemistry. The main ionic conduction mechanism is identified as solvent-assisted Li hopping by measuring the ionic conductivity using theories based on different levels of transport theory approximations. The Li^+ distribution in the SSE is found to be highly correlated to the charge distribution on the POM cluster. A hypothetical non-interpenetrated MOF-688 derivative with an increased pore volume exhibits a significant improvement in ionic conductivity than the original MOF-688, providing insights into the design rules of the novel type of SSEs based on intrinsically anionic MOFs.

Bibliography

1. Hou, T.-Z., Peng, H.-J., Huang, J.-Q., Zhang, Q. & Li, B. The formation of strong-couple interactions between nitrogen-doped graphene and sulfur/lithium (poly)sulfides in lithium-sulfur batteries. *2D Materials* **2,** 014011 (2015).

2. Clément, R. J., Lun, Z. & Ceder, G. Cation-disordered rocksalt transition metal oxides and oxyfluorides for high energy lithium-ion cathodes. *Energy & Environmental Science* **13,** 345–373 (2 2020).

3. Lun, Z., Ouyang, B., Kwon, D.-H., Ha, Y., Foley, E. E., Huang, T.-Y., Cai, Z., Kim, H., Balasubramanian, M., Sun, Y., Huang, J., Tian, Y., Kim, H., McCloskey, B. D., Yang, W., Clément, R. J., Ji, H. & Ceder, G. Cation-disordered rocksalt-type high-entropy cathodes for Li-ion batteries. *Nature Materials* **20,** 214–221 (2020).

4. Manthiram, A., Fu, Y., Chung, S.-H., Zu, C. & Su, Y.-S. Rechargeable Lithium–Sulfur Batteries. *Chemical Reviews* **114,** 11751–11787 (2014).

5. Chen, X., Li, X., Mei, D., Feng, J., Hu, M. Y., Hu, J., Engelhard, M., Zheng, J., Xu, W., Xiao, J., Liu, J. & Zhang, J.-G. Reduction Mechanism of Fluoroethylene Carbonate for Stable Solid-Electrolyte Interphase Film on Silicon Anode. *ChemSusChem* **7,** 549–554 (2014).

6. Lin, D., Liu, Y. & Cui, Y. Reviving the lithium metal anode for high-energy batteries. *Nature Nanotechnology* **12,** 194–206 (2017).

7. Xu, K. Nonaqueous Liquid Electrolytes for Lithium-Based Rechargeable Batteries. *Chemical Reviews* **104,** 4303–4418 (2004).

8. Su, C.-C., He, M., Amine, R., Rojas, T., Cheng, L., Ngo, A. T. & Amine, K. Solvating power series of electrolyte solvents for lithium batteries. *Energy & Environmental Science* **12,** 1249–1254 (2019).

9. Cheng, X. B., Zhang, R., Zhao, C. Z. & Zhang, Q. Toward Safe Lithium Metal Anode in Rechargeable Batteries: A Review. *Chemical Reviews* **117,** 10403–10473 (2017).

10. Chen, X., Shen, X., Li, B., Peng, H. J., Cheng, X. B., Li, B. Q., Zhang, X. Q., Huang, J. Q. & Zhang, Q. Ion-Solvent Complexes Promote Gas Evolution from Electrolytes on a Sodium Metal Anode. *Angewandte Chemie International Edition* **57,** 734–737 (2018).

11. Zhang, X. Q., Chen, X., Cheng, X. B., Li, B. Q., Shen, X., Yan, C., Huang, J. Q. & Zhang, Q. Highly Stable Lithium Metal Batteries Enabled by Regulating the Solvation of Lithium Ions in Nonaqueous Electrolytes. *Angewandte Chemie International Edition* **57,** 5301–5305 (2018).

12. Liu, B., Xu, W., Yan, P., Kim, S. T., Engelhard, M. H., Sun, X., Mei, D., Cho, J., Wang, C.-M. & Zhang, J.-G. Stabilization of Li Metal Anode in DMSO-Based Electrolytes via Optimization of Salt-Solvent Coordination for Li-O$_2$ Batteries. *Advanced Energy Materials* **7,** 1602605 (2017).

13. Schroder, K., Alvarado, J., Yersak, T. A., Li, J., Dudney, N., Webb, L. J., Meng, Y. S. & Stevenson, K. J. The Effect of Fluoroethylene Carbonate as an Additive on the Solid Electrolyte Interphase on Silicon Lithium-Ion Electrodes. *Chemistry of Materials* **27,** 5531–5542 (2015).

14. Cheng, X.-B., Yan, C., Chen, X., Guan, C., Huang, J.-Q., Peng, H.-J., Zhang, R., Yang, S.-T. & Zhang, Q. Implantable Solid Electrolyte Interphase in Lithium-Metal Batteries. *Chem* **2,** 258–270 (2017).

15. Shi, S., Lu, P., Liu, Z., Qi, Y., Hector L. G., J., Li, H. & Harris, S. J. Direct calculation of Li-ion transport in the solid electrolyte interphase. *Journal of the American Chemical Society* **134,** 15476–87 (2012).

16. Shi, S., Qi, Y., Li, H. & Hector, L. G. Defect Thermodynamics and Diffusion Mechanisms in Li$_2$CO$_3$ and Implications for the Solid Electrolyte Interphase in Li-Ion Batteries. *The Journal of Physical Chemistry C* **117,** 8579–8593 (2013).

17. Aurbach, D. The Study of Electrolyte Solutions Based on Ethylene and Diethyl Carbonates for Rechargeable Li Batteries. *Journal of The Electrochemical Society* **142,** 2882–2890 (1995).

18. Xu, K., Lam, Y., Zhang, S. S., Jow, T. R. & Curtis, T. B. Solvation Sheath of Li$^+$ in Nonaqueous Electrolytes and Its Implication of Graphite/Electrolyte Interface Chemistry. *The Journal of Physical Chemistry C* **111,** 7411–7421 (2007).

19. Seo, D. M., Chalasani, D., Parimalam, B. S., Kadam, R., Nie, M. & Lucht, B. L. Reduction Reactions of Carbonate Solvents for Lithium Ion Batteries. *ECS Electrochemistry Letters* **3,** A91–A93 (2014).

20. Philippe, B., Dedryvère, R., Gorgoi, M., Rensmo, H., Gonbeau, D. & Edström, K. Role of the LiPF$_6$ Salt for the Long-Term Stability of Silicon Electrodes in Li-Ion Batteries – A Photoelectron Spectroscopy Study. *Chemistry of Materials* **25,** 394–404 (2013).

21. Parimalam, B. S., MacIntosh, A. D., Kadam, R. & Lucht, B. L. Decomposition Reactions of Anode Solid Electrolyte Interphase (SEI) Components with LiPF$_6$. *The Journal of Physical Chemistry C* **121,** 22733–22738 (2017).

22. Jurng, S., Brown, Z. L., Kim, J. & Lucht, B. L. Effect of electrolyte on the nanostructure of the solid electrolyte interphase (SEI) and performance of lithium metal anodes. *Energy & Environmental Science* **11,** 2600–2608 (2018).

23. Etacheri, V., Marom, R., Elazari, R., Salitra, G. & Aurbach, D. Challenges in the development of advanced Li-ion batteries: a review. *Energy & Environmental Science* **4,** 3243 (2011).

24. Nitta, N., Wu, F., Lee, J. T. & Yushin, G. Li-ion battery materials: present and future. *Materials Today* **18,** 252–264 (2015).

25. Xie, J. & Lu, Y.-C. A retrospective on lithium-ion batteries. *Nature Communications* **11** (2020).

26. An, S. J., Li, J., Daniel, C., Mohanty, D., Nagpure, S. & Wood, D. L. The state of understanding of the lithium-ion-battery graphite solid electrolyte interphase (SEI) and its relationship to formation cycling. *Carbon* **105,** 52–76 (2016).

27. Graetz, J., Ahn, C. C., Yazami, R. & Fultz, B. Highly Reversible Lithium Storage in Nanostructured Silicon. *Electrochemical and Solid-State Letters* **6,** A194 (2003).

28. Schweidler, S., de Biasi, L., Schiele, A., Hartmann, P., Brezesinski, T. & Janek, J. Volume Changes of Graphite Anodes Revisited: A Combined Operando X-ray Diffraction and In Situ Pressure Analysis Study. *The Journal of Physical Chemistry C* **122,** 8829–8835 (2018).

29. Xu, K. Electrolytes and Interphases in Li-Ion Batteries and Beyond. *Chemical Reviews* **114,** 11503–11618 (2014).

30. Xu, C., Lindgren, F., Philippe, B., Gorgoi, M., Björefors, F., Edström, K. & Gustafsson, T. Improved Performance of the Silicon Anode for Li-Ion Batteries: Understanding the Surface Modification Mechanism of Fluoroethylene Carbonate as an Effective Electrolyte Additive. *Chemistry of Materials* **27,** 2591–2599 (2015).

31. Wu, H., Zheng, G., Liu, N., Carney, T. J., Yang, Y. & Cui, Y. Engineering empty space between Si nanoparticles for lithium-ion battery anodes. *Nano Letters* **12,** 904–9 (2012).

32. Jin, Y., Li, S., Kushima, A., Zheng, X., Sun, Y., Xie, J., Sun, J., Xue, W., Zhou, G., Wu, J., Shi, F., Zhang, R., Zhu, Z., So, K., Cui, Y. & Li, J. Self-healing SEI enables full-cell cycling of a silicon-majority anode with a coulombic efficiency exceeding 99.9%. *Energy & Environmental Science* **10,** 580–592 (2017).

33. Nguyen, C. C., Yoon, T., Seo, D. M., Guduru, P. & Lucht, B. L. Systematic Investigation of Binders for Silicon Anodes: Interactions of Binder with Silicon Particles and Electrolytes and Effects of Binders on Solid Electrolyte Interphase Formation. *ACS Applied Materials & Interfaces* **8,** 12211–20 (2016).

34. Nguyen, C. C., Seo, D. M., Chandrasiri, K. & Lucht, B. L. Improved Cycling Performance of a Si Nanoparticle Anode Utilizing Citric Acid as a Surface-Modifying Agent. *Langmuir* **33,** 9254–9261 (2017).

35. Chen, Z., Wang, C., Lopez, J., Lu, Z., Cui, Y. & Bao, Z. High-Areal-Capacity Silicon Electrodes with Low-Cost Silicon Particles Based on Spatial Control of Self-Healing Binder. *Advanced Energy Materials* **5,** 1401826 (2015).

36. Nguyen, C. C. & Lucht, B. L. Comparative Study of Fluoroethylene Carbonate and Vinylene Carbonate for Silicon Anodes in Lithium Ion Batteries. *Journal of the Electrochemical Society* **161,** A1933–A1938 (2014).

37. Philippe, B., Dedryvere, R., Gorgoi, M., Rensmo, H., Gonbeau, D. & Edstrom, K. Improved performances of nanosilicon electrodes using the salt LiFSI: a photoelectron spectroscopy study. *Journal of the American Chemical Society* **135,** 9829–42 (2013).

38. Liu, N., Wu, H., McDowell, M. T., Yao, Y., Wang, C. & Cui, Y. A Yolk-Shell Design for Stabilized and Scalable Li-Ion Battery Alloy Anodes. *Nano Letters* **12,** 3315–3321 (2012).

39. Xu, W., Wang, J., Ding, F., Chen, X., Nasybulin, E., Zhang, Y. & Zhang, J.-G. Lithium metal anodes for rechargeable batteries. *Energy & Environmental Science* **7,** 513–537 (2014).

40. Sun, Y., Liu, N. & Cui, Y. Promises and challenges of nanomaterials for lithium-based rechargeable batteries. *Nature Energy* **1** (2016).

41. Ding, F., Xu, W., Graff, G. L., Zhang, J., Sushko, M. L., Chen, X., Shao, Y., Engelhard, M. H., Nie, Z., Xiao, J., Liu, X., Sushko, P. V., Liu, J. & Zhang, J.-G. Dendrite-Free Lithium Deposition via Self-Healing Electrostatic Shield Mechanism. *Journal of the American Chemical Society* **135,** 4450–4456 (2013).

42. Zhang, X.-Q., Cheng, X.-B., Chen, X., Yan, C. & Zhang, Q. Fluoroethylene Carbonate Additives to Render Uniform Li Deposits in Lithium Metal Batteries. *Advanced Functional Materials* **27,** 1605989 (2017).

43. Qian, J., Henderson, W. A., Xu, W., Bhattacharya, P., Engelhard, M., Borodin, O. & Zhang, J. G. High rate and stable cycling of lithium metal anode. *Nature Communications* **6,** 6362 (2015).

44. Shkrob, I. A., Wishart, J. F. & Abraham, D. P. What Makes Fluoroethylene Carbonate Different? *The Journal of Physical Chemistry C* **119,** 14954–14964 (2015).

45. Qin, K., Holguin, K., Mohammadiroudbari, M., Huang, J., Kim, E. Y. S., Hall, R. & Luo, C. Strategies in Structure and Electrolyte Design for High-Performance Lithium Metal Batteries. *Advanced Functional Materials* **31,** 2009694 (2021).

46. Wenzel, S., Weber, D. A., Leichtweiss, T., Busche, M. R., Sann, J. & Janek, J. Interphase formation and degradation of charge transfer kinetics between a lithium metal anode and highly crystalline $Li_7P_3S_{11}$ solid electrolyte. *Solid State Ionics* **286,** 24–33 (2016).

47. Aono, H., Sugimoto, E., Sadaoka, Y., Imanaka, N. & Adachi, G.-y. Ionic Conductivity of the Lithium Titanium Phosphate ($Li_{1+X}M_X Ti_{2-X}(PO_4)_3$, M=Al, Sc, Y, and La) Systems. *Journal of The Electrochemical Society* **136,** 590–591 (1989).

48. Luo, W., Gong, Y., Zhu, Y., Li, Y., Yao, Y., Zhang, Y., Fu, K., Pastel, G., Lin, C.-F., Mo, Y., Wachsman, E. D. & Hu, L. Reducing Interfacial Resistance between Garnet-Structured Solid-State Electrolyte and Li-Metal Anode by a Germanium Layer. *Advanced Materials* **29,** 1606042 (2017).

49. Huo, H., Chen, Y., Zhao, N., Lin, X., Luo, J., Yang, X., Liu, Y., Guo, X. & Sun, X. In-situ formed Li_2CO_3-free garnet/Li interface by rapid acid treatment for dendrite-free solid-state batteries. *Nano Energy* **61,** 119–125 (2019).

50. Zhao, C.-Z., Zhang, X.-Q., Cheng, X.-B., Zhang, R., Xu, R., Chen, P.-Y., Peng, H.-J., Huang, J.-Q. & Zhang, Q. An anion-immobilized composite electrolyte for dendrite-free lithium metal anodes. *Proceedings of the National Academy of Sciences* **114,** 11069–11074 (2017).

51. Fong, K. D., Self, J., Diederichsen, K. M., Wood, B. M., McCloskey, B. D. & Persson, K. A. Ion Transport and the True Transference Number in Nonaqueous Polyelectrolyte Solutions for Lithium Ion Batteries. *ACS Central Science* **5,** 1250–1260 (2019).

52. Brissot, C., Rosso, M., Chazalviel, J.-N. & Lascaud, S. Dendritic growth mechanisms in lithium/polymer cells. *Journal of Power Sources* **81-82,** 925–929 (1999).

53. Singh, M., Odusanya, O., Wilmes, G. M., Eitouni, H. B., Gomez, E. D., Patel, A. J., Chen, V. L., Park, M. J., Fragouli, P., Iatrou, H., Hadjichristidis, N., Cookson, D. & Balsara, N. P. Effect of Molecular Weight on the Mechanical and Electrical Properties of Block Copolymer Electrolytes. *Macromolecules* **40,** 4578–4585 (2007).

54. Bouchet, R., Maria, S., Meziane, R., Aboulaich, A., Lienafa, L., Bonnet, J.-P., Phan, T. N. T., Bertin, D., Gigmes, D., Devaux, D., Denoyel, R. & Armand, M. Single-ion BAB triblock copolymers as highly efficient electrolytes for lithium-metal batteries. *Nature Materials* **12,** 452–457 (2013).

55. Stone, G. M., Mullin, S. A., Teran, A. A., Hallinan, D. T., Minor, A. M., Hexemer, A. & Balsara, N. P. Resolution of the Modulus versus Adhesion Dilemma in Solid Polymer Electrolytes for Rechargeable Lithium Metal Batteries. *Journal of The Electrochemical Society* **159,** A222–A227 (2012).

56. Zhou, W., Wang, Z., Pu, Y., Li, Y., Xin, S., Li, X., Chen, J. & Goodenough, J. B. Double-Layer Polymer Electrolyte for High-Voltage All-Solid-State Rechargeable Batteries. *Advanced Materials* **31,** 1805574 (2019).

57. Duan, H., Fan, M., Chen, W.-P., Li, J.-Y., Wang, P.-F., Wang, W.-P., Shi, J.-L., Yin, Y.-X., Wan, L.-J. & Guo, Y.-G. Extended Electrochemical Window of Solid Electrolytes via Heterogeneous Multilayered Structure for High-Voltage Lithium Metal Batteries. *Advanced Materials* **31,** 1807789 (2019).

58. Cheng, Q., Li, A., Li, N., Li, S., Zangiabadi, A., Li, T.-D., Huang, W., Li, A. C., Jin, T., Song, Q., Xu, W., Ni, N., Zhai, H., Dontigny, M., Zaghib, K., Chuan, X., Su, D., Yan, K. & Yang, Y. Stabilizing Solid Electrolyte-Anode Interface in Li-Metal Batteries by Boron Nitride-Based Nanocomposite Coating. *Joule* **3,** 1510–1522 (2019).

59. Liu, W., Liu, N., Sun, J., Hsu, P.-C., Li, Y., Lee, H.-W. & Cui, Y. Ionic Conductivity Enhancement of Polymer Electrolytes with Ceramic Nanowire Fillers. *Nano Letters* **15,** 2740–2745 (2015).

60. Zhou, W., Wang, S., Li, Y., Xin, S., Manthiram, A. & Goodenough, J. B. Plating a Dendrite-Free Lithium Anode with a Polymer/Ceramic/Polymer Sandwich Electrolyte. *Journal of the American Chemical Society* **138,** 9385–9388 (2016).

61. Xu, W., Pei, X., Diercks, C. S., Lyu, H., Ji, Z. & Yaghi, O. M. A Metal–Organic Framework of Organic Vertices and Polyoxometalate Linkers as a Solid-State Electrolyte. *Journal of the American Chemical Society* **141,** 17522–17526 (2019).

62. Miner, E. M. & Dincă, M. Metal- and covalent-organic frameworks as solid-state electrolytes for metal-ion batteries. *Philosophical Transactions of the Royal Society A: Mathematical, Physical and Engineering Sciences* **377,** 20180225 (2019).

63. Dzubak, A. L., Lin, L. C., Kim, J., Swisher, J. A., Poloni, R., Maximoff, S. N., Smit, B. & Gagliardi, L. Ab initio carbon capture in open-site metal–organic frameworks. *Nature Chemistry* **4,** 810–6 (2012).

64. Park, S. S., Tulchinsky, Y. & Dincă, M. Single-Ion Li$^+$, Na$^+$, and Mg^{2+} Solid Electrolytes Supported by a Mesoporous Anionic Cu–Azolate Metal–Organic Framework. *Journal of the American Chemical Society* **139,** 13260–13263 (2017).

65. Wiers, B. M., Foo, M.-L., Balsara, N. P. & Long, J. R. A Solid Lithium Electrolyte via Addition of Lithium Isopropoxide to a Metal–Organic Framework with Open Metal Sites. *Journal of the American Chemical Society* **133,** 14522–14525 (2011).

66. Borodin, O. & Smith, G. D. Quantum chemistry and molecular dynamics simulation study of dimethyl carbonate: ethylene carbonate electrolytes doped with LiPF$_6$. *The Journal of Physical Chemistry B* **113,** 1763–76 (2009).

67. Lee, K. K., Park, K., Lee, H., Noh, Y., Kossowska, D., Kwak, K. & Cho, M. Ultrafast fluxional exchange dynamics in electrolyte solvation sheath of lithium ion battery. *Nature Communications* **8,** 14658 (2017).

68. Frenkel, D. & Smit, B. in *Understanding Molecular Simulation (Second Edition)* (eds Frenkel, D. & Smit, B.) Second Edition, 63–107 (Academic Press, San Diego, 2002).

69. Frenkel, D. & Smit, B. in *Understanding Molecular Simulation (Second Edition)* (eds Frenkel, D. & Smit, B.) Second Edition, 23–61 (Academic Press, San Diego, 2002).

70. Frenkel, D. & Smit, B. in *Understanding Molecular Simulation (Second Edition)* (eds Frenkel, D. & Smit, B.) Second Edition, 291–320 (Academic Press, San Diego, 2002).

71. Onsager, L. Reciprocal Relations in Irreversible Processes. I. *Physical Review* **37,** 405–426 (1931).

72. Fong, K. D., Bergstrom, H. K., McCloskey, B. D. & Mandadapu, K. K. Transport phenomena in electrolyte solutions: Nonequilibrium thermodynamics and statistical mechanics. *AIChE Journal* **66,** e17091 (2020).

73. Einstein, A. Über die von der molekularkinetischen Theorie der Wärme geforderte Bewegung von in ruhenden Flüssigkeiten suspendierten Teilchen. *Annalen der Physik* **322,** 549–560 (1905).

74. Pesko, D. M., Timachova, K., Bhattacharya, R., Smith, M. C., Villaluenga, I., Newman, J. & Balsara, N. P. Negative Transference Numbers in Poly(ethylene oxide)-Based Electrolytes. *Journal of The Electrochemical Society* **164,** E3569–E3575 (2017).

75. Fong, K. D., Self, J., McCloskey, B. D. & Persson, K. A. Onsager Transport Coefficients and Transference Numbers in Polyelectrolyte Solutions and Polymerized Ionic Liquids. *Macromolecules* **53,** 9503–9512 (2020).

76. Frenkel, D. & Smit, B. in *Understanding Molecular Simulation (Second Edition)* (eds Frenkel, D. & Smit, B.) Second Edition, 139–163 (Academic Press, San Diego, 2002).

77. Schneider, T. & Stoll, E. Molecular-dynamics study of a three-dimensional one-component model for distortive phase transitions. *Physical Review B* **17,** 1302–1322 (1978).

78. Nosé, S. A unified formulation of the constant temperature molecular dynamics methods. *The Journal of Chemical Physics* **81,** 511–519 (1984).

79. Hoover, W. G. Canonical dynamics: Equilibrium phase-space distributions. *Physical Review A* **31,** 1695–1697 (1985).

80. Jorgensen, W. L., Maxwell, D. S. & Tirado-Rives, J. Development and Testing of the OPLS All-Atom Force Field on Conformational Energetics and Properties of Organic Liquids. *Journal of the American Chemical Society* **118,** 11225–11236 (1996).

81. Kaminski, G. A., Friesner, R. A., Tirado-Rives, J. & Jorgensen, W. L. Evaluation and Reparametrization of the OPLS-AA Force Field for Proteins via Comparison with Accurate Quantum Chemical Calculations on Peptides†. *The Journal of Physical Chemistry B* **105,** 6474–6487 (2001).

82. Borodin, O. in *Electrolytes for Lithium and Lithium-Ion Batteries* (eds Jow, T. R., Xu, K., Borodin, O. & Ue, M.) 371–401 (Springer New York, New York, NY, 2014).

83. Ding, W., Lei, X. & Ouyang, C. Coordination of lithium ion with ethylene carbonate electrolyte solvent: A computational study. *International Journal of Quantum Chemistry* **116,** 97–102 (2016).

84. Cui, W., Lansac, Y., Lee, H., Hong, S.-T. & Jang, Y. H. Lithium ion solvation by ethylene carbonates in lithium-ion battery electrolytes, revisited by density functional theory with the hybrid solvation model and free energy correction in solution. *Physical Chemistry Chemical Physics* **18,** 23607–23612 (2016).

85. Xia, J., Petibon, R., Xiong, D., Ma, L. & Dahn, J. Enabling linear alkyl carbonate electrolytes for high voltage Li-ion cells. *Journal of Power Sources* **328,** 124–135 (2016).

86. Horn, P. R., Mao, Y. & Head-Gordon, M. Probing non-covalent interactions with a second generation energy decomposition analysis using absolutely localized molecular orbitals. *Physical Chemistry Chemical Physics* **18,** 23067–23079 (2016).

87. Mao, Y., Loipersberger, M., Kron, K. J., Derrick, J. S., Chang, C. J., Sharada, S. M. & Head-Gordon, M. Consistent inclusion of continuum solvation in energy decomposition analysis: theory and application to molecular CO_2 reduction catalysts. *Chemical Science* **12,** 1398–1414 (2021).

88. Mao, Y., Levine, D. S., Loipersberger, M., Horn, P. R. & Head-Gordon, M. Probing radical–molecule interactions with a second generation energy decomposition analysis of DFT calculations using absolutely localized molecular orbitals. *Physical Chemistry Chemical Physics* **22,** 12867–12885 (2020).

89. Sina, M., Alvarado, J., Shobukawa, H., Alexander, C., Manichev, V., Feldman, L., Gustafsson, T., Stevenson, K. J. & Meng, Y. S. Direct Visualization of the Solid Electrolyte Interphase and Its Effects on Silicon Electrochemical Performance. *Advanced Materials Interfaces* **3,** 1600438 (2016).

90. Shi, F., Ross, P. N., Somorjai, G. A. & Komvopoulos, K. The Chemistry of Electrolyte Reduction on Silicon Electrodes Revealed by in Situ ATR-FTIR Spectroscopy. *The Journal of Physical Chemistry C* **121,** 14476–14483 (2017).

91. Schroder, K. W., Celio, H., Webb, L. J. & Stevenson, K. J. Examining Solid Electrolyte Interphase Formation on Crystalline Silicon Electrodes: Influence of Electrochemical Preparation and Ambient Exposure Conditions. *The Journal of Physical Chemistry C* **116,** 19737–19747 (2012).

92. Breitung, B., Baumann, P., Sommer, H., Janek, J. & Brezesinski, T. In situ and operando atomic force microscopy of high-capacity nano-silicon based electrodes for lithium-ion batteries. *Nanoscale* **8,** 14048–56 (2016).

93. Yoon, I., Abraham, D. P., Lucht, B. L., Bower, A. F. & Guduru, P. R. In Situ Measurement of Solid Electrolyte Interphase Evolution on Silicon Anodes Using Atomic Force Microscopy. *Advanced Energy Materials* **6,** 1600099 (2016).

94. Young, B. T., Heskett, D. R., Nguyen, C. C., Nie, M., Woicik, J. C. & Lucht, B. L. Hard X-ray Photoelectron Spectroscopy (HAXPES) Investigation of the Silicon Solid Electrolyte Interphase (SEI) in Lithium-Ion Batteries. *ACS Applied Materials & Interfaces* **7,** 20004–11 (2015).

95. Jin, Y., Kneusels, N. H., Magusin, P., Kim, G., Castillo-Martinez, E., Marbella, L. E., Kerber, R. N., Howe, D. J., Paul, S., Liu, T. & Grey, C. P. Identifying the Structural Basis for the Increased Stability of the Solid Electrolyte Interphase Formed on Silicon with the Additive Fluoroethylene Carbonate. *Journal of the American Chemical Society* **139,** 14992–15004 (2017).

96. Schiele, A., Breitung, B., Hatsukade, T., Berkes, B. B., Hartmann, P., Janek, J. & Brezesinski, T. The Critical Role of Fluoroethylene Carbonate in the Gassing of Silicon Anodes for Lithium-Ion Batteries. *ACS Energy Letters* **2,** 2228–2233 (2017).

97. Zhang, Y., Su, M., Yu, X., Zhou, Y., Wang, J., Cao, R., Xu, W., Wang, C., Baer, D. R., Borodin, O., Xu, K., Wang, Y., Wang, X. L., Xu, Z., Wang, F. & Zhu, Z. Investigation of Ion-Solvent Interactions in Nonaqueous Electrolytes Using in Situ Liquid SIMS. *Analytical Chemistry* **90,** 3341–3348 (2018).

98. Stetson, C., Yoon, T., Coyle, J., Nemeth, W., Young, M., Norman, A., Pylypenko, S., Ban, C., Jiang, C.-S., Al-Jassim, M. & Burrell, A. Three-dimensional electronic resistivity mapping of solid electrolyte interphase on Si anode materials. *Nano Energy* **55,** 477–485 (2019).

99. Shobukawa, H., Alvarado, J., Yang, Y. & Meng, Y. S. Electrochemical performance and interfacial investigation on Si composite anode for lithium ion batteries in full cell. *Journal of Power Sources* **359,** 173–181 (2017).

100. Markevich, E., Salitra, G. & Aurbach, D. Fluoroethylene Carbonate as an Important Component for the Formation of an Effective Solid Electrolyte Interphase on Anodes and Cathodes for Advanced Li-Ion Batteries. *ACS Energy Letters* **2,** 1337–1345 (2017).

101. Shi, S., Gao, J., Liu, Y., Zhao, Y., Wu, Q., Ju, W., Ouyang, C. & Xiao, R. Multiscale computation methods: Their applications in lithium-ion battery research and development. *Chinese Physics B* **25** (2016).

102. Michan, A. L., Parimalam, B. S., Leskes, M., Kerber, R. N., Yoon, T., Grey, C. P. & Lucht, B. L. Fluoroethylene Carbonate and Vinylene Carbonate Reduction: Understanding Lithium-Ion Battery Electrolyte Additives and Solid Electrolyte Interphase Formation. *Chemistry of Materials* **28,** 8149–8159 (2016).

103. Parimalam, B. S. & Lucht, B. L. Reduction Reactions of Electrolyte Salts for Lithium Ion Batteries: LiPF$_6$, LiBF$_4$, LiDFOB, LiBOB, and LiTFSI. *Journal of The Electrochemical Society* **165,** A251–A255 (2018).

104. Malliakas, C. D., Leung, K., Pupek, K. Z., Shkrob, I. A. & Abraham, D. P. Spontaneous aggregation of lithium ion coordination polymers in fluorinated electrolytes for high-voltage batteries. *Physical Chemistry Chemical Physics* **18,** 10846–9 (2016).

105. Perez-Beltran, S., Ramírez-Caballero, G. E. & Balbuena, P. B. First-Principles Calculations of Lithiation of a Hydroxylated Surface of Amorphous Silicon Dioxide. *The Journal of Physical Chemistry C* **119,** 16424–16431 (2015).

106. Soto, F. A., Ma, Y., Martinez de la Hoz, J. M., Seminario, J. M. & Balbuena, P. B. Formation and Growth Mechanisms of Solid-Electrolyte Interphase Layers in Rechargeable Batteries. *Chemistry of Materials* **27,** 7990–8000 (2015).

107. Soto, F. A., Martinez de la Hoz, J. M., Seminario, J. M. & Balbuena, P. B. Modeling solid-electrolyte interfacial phenomena in silicon anodes. *Current Opinion in Chemical Engineering* **13,** 179–185 (2016).

108. Delp, S. A., Borodin, O., Olguin, M., Eisner, C. G., Allen, J. L. & Jow, T. R. Importance of Reduction and Oxidation Stability of High Voltage Electrolytes and Additives. *Electrochimica Acta* **209,** 498–510 (2016).

109. Martinez de la Hoz, J. M., Soto, F. A. & Balbuena, P. B. Effect of the Electrolyte Composition on SEI Reactions at Si Anodes of Li-Ion Batteries. *The Journal of Physical Chemistry C* **119,** 7060–7068 (2015).

110. Martinez de la Hoz, J. M., Leung, K. & Balbuena, P. B. Reduction mechanisms of ethylene carbonate on si anodes of lithium-ion batteries: effects of degree of lithiation and nature of exposed surface. *ACS Applied Materials & Interfaces* **5,** 13457–65 (2013).

111. Martinez de la Hoz, J. M. & Balbuena, P. B. Reduction mechanisms of additives on Si anodes of Li-ion batteries. *Physical Chemistry Chemical Physics* **16,** 17091–8 (2014).

112. Leung, K., Rempe, S. B., Foster, M. E., Ma, Y., Martinez del la Hoz, J. M., Sai, N. & Balbuena, P. B. Modeling Electrochemical Decomposition of Fluoroethylene Carbonate on Silicon Anode Surfaces in Lithium Ion Batteries. *Journal of the Electrochemical Society* **161,** A213–A221 (2013).

113. Perez-Beltran, S., Ramírez-Caballero, G. E. & Balbuena, P. B. Ethylene Carbonate Reduction on Lithiated Surfaces of Hydroxylated Amorphous Silicon Dioxide. *Journal of The Electrochemical Society* **163,** A2197–A2202 (2016).

114. Leung, K. Two-electron reduction of ethylene carbonate: A quantum chemistry re-examination of mechanisms. *Chemical Physics Letters* **568-569,** 1–8 (2013).

115. Burkhardt, S. E. Impact of Chemical Follow-up Reactions for Lithium Ion Electrolytes: Generation of Nucleophilic Species, Solid Electrolyte Interphase, and Gas Formation. *Journal of The Electrochemical Society* **164,** A684–A690 (2017).

116. Soto, F. A. & Balbuena, P. B. Elucidating Oligomer-Surface and Oligomer-Oligomer Interactions at a Lithiated Silicon Surface. *Electrochimica Acta* **220,** 312–321 (2016).

117. Benitez, L., Cristancho, D., Seminario, J. M., Martinez de la Hoz, J. M. & Balbuena, P. B. Electron transfer through solid-electrolyte-interphase layers formed on Si anodes of Li-ion batteries. *Electrochimica Acta* **140,** 250–257 (2014).

118. Borodin, O., Ren, X., Vatamanu, J., von Wald Cresce, A., Knap, J. & Xu, K. Modeling Insight into Battery Electrolyte Electrochemical Stability and Interfacial Structure. *Accounts of Chemical Research* **50,** 2886–2894 (2017).

119. Ma, Y. & Balbuena, P. B. DFT Study of Reduction Mechanisms of Ethylene Carbonate and Fluoroethylene Carbonate on Li^+-Adsorbed Si Clusters. *Journal of the Electrochemical Society* **161,** E3097–E3109 (2014).

120. Wang, A., Kadam, S., Li, H., Shi, S. & Qi, Y. Review on modeling of the anode solid electrolyte interphase (SEI) for lithium-ion batteries. *npj Computational Materials* **4** (2018).

121. Takenaka, N., Sakai, H., Suzuki, Y., Uppula, P. & Nagaoka, M. A Computational Chemical Insight into Microscopic Additive Effect on Solid Electrolyte Interphase Film Formation in Sodium-Ion Batteries: Suppression of Unstable Film Growth by Intact Fluoroethylene Carbonate. *The Journal of Physical Chemistry C* **119,** 18046–18055 (2015).

122. Okuno, Y., Ushirogata, K., Sodeyama, K. & Tateyama, Y. Decomposition of the fluoroethylene carbonate additive and the glue effect of lithium fluoride products for the solid electrolyte interphase: an ab initio study. *Physical Chemistry Chemical Physics* **18,** 8643–53 (2016).

123. Plimpton, S. Fast Parallel Algorithms for Short-Range Molecular-Dynamics. *Journal of Computational Physics* **117,** 1–19 (1995).

124. Martinez, L., Andrade, R., Birgin, E. G. & Martinez, J. M. PACKMOL: a package for building initial configurations for molecular dynamics simulations. *Journal of Computational Chemistry* **30,** 2157–64 (2009).

125. Seo, D. M., Allen, J. L., Gardner, L. A., Han, S. D., Boyle, P. D. & Henderson, W. A. Electrolyte Solvation and Ionic Association: Cyclic Carbonate and Ester-LiTFSI and -$LiPF_6$ Mixtures. *ECS Transactions* **50,** 375–380 (2013).

126. Ding, M. S., Li, Q., Li, X., Xu, W. & Xu, K. Effects of Solvent Composition on Liquid Range, Glass Transition, and Conductivity of Electrolytes of a (Li, Cs)PF_6 Salt in EC-PC-EMC Solvents. *The Journal of Physical Chemistry C* **121,** 11178–11183 (2017).

127. Lopes, J. N. C. & Padua, A. A. H. Molecular force field for ionic liquids composed of triflate or bistriflylimide anions. *Journal of Physical Chemistry B* **108,** 16893–16898 (2004).

128. Jensen, K. P. & Jorgensen, W. L. Halide, Ammonium, and Alkali Metal Ion Parameters for Modeling Aqueous Solutions. *Journal of Chemical Theory and Computation* **2,** 1499–509 (2006).

129. Becke, A. D. Density-functional thermochemistry. III. The role of exact exchange. *The Journal of Chemical Physics* **98,** 5648–5652 (1993).

130. Computer Program. 2016.

131. Bayly, C. I., Cieplak, P., Cornell, W. D. & Kollman, P. A. A Well-Behaved Electrostatic Potential Based Method Using Charge Restraints for Deriving Atomic Charges - the Resp Model. *Journal of Physical Chemistry* **97,** 10269–10280 (1993).

132. Rajput, N. N., Murugesan, V., Shin, Y., Han, K. S., Lau, K. C., Chen, J., Liu, J., Curtiss, L. A., Mueller, K. T. & Persson, K. A. Elucidating the Solvation Structure and Dynamics of Lithium Polysulfides Resulting from Competitive Salt and Solvent Interactions. *Chemistry of Materials* **29,** 3375–3379 (2017).

133. Borodin, O., Olguin, M., Ganesh, P., Kent, P. R., Allen, J. L. & Henderson, W. A. Competitive lithium solvation of linear and cyclic carbonates from quantum chemistry. *Physical Chemistry Chemical Physics* **18,** 164–75 (2016).

134. Hagiyama, K., Suzuki, K., Ohtake, M., Shimada, M., Nanbu, N., Takehara, M., Ue, M. & Sasaki, Y. Physical Properties of Substituted 1,3-Dioxolan-2-ones. *Chemistry Letters* **37,** 210–211 (2008).

135. Ravikumar, B., Mynam, M. & Rai, B. Effect of Salt Concentration on Properties of Lithium Ion Battery Electrolytes: A Molecular Dynamics Study. *The Journal of Physical Chemistry C* **122,** 8173–8181 (2018).

136. Yoon, T., Chapman, N., Seo, D. M. & Lucht, B. L. Lithium Salt Effects on Silicon Electrode Performance and Solid Electrolyte Interphase (SEI) Structure, Role of Solution Structure on SEI Formation. *Journal of The Electrochemical Society* **164,** A2082–A2088 (2017).

137. Chapman, N., Borodin, O., Yoon, T., Nguyen, C. C. & Lucht, B. L. Spectroscopic and Density Functional Theory Characterization of Common Lithium Salt Solvates in Carbonate Electrolytes for Lithium Batteries. *The Journal of Physical Chemistry C* **121,** 2135–2148 (2017).

138. Tenney, C. M. & Cygan, R. T. Analysis of Molecular Clusters in Simulations of Lithium-Ion Battery Electrolytes. *The Journal of Physical Chemistry C* **117,** 24673–24684 (2013).

139. Hayamizu, K. Temperature Dependence of Self-Diffusion Coefficients of Ions and Solvents in Ethylene Carbonate, Propylene Carbonate, and Diethyl Carbonate Single Solutions and Ethylene Carbonate + Diethyl Carbonate Binary Solutions of LiPF$_6$ Studied by NMR. *Journal of Chemical & Engineering Data* **57,** 2012–2017 (2012).

140. Wang, J., Wolf, R. M., Caldwell, J. W., Kollman, P. A. & Case, D. A. Development and testing of a general amber force field. *Journal of Computational Chemistry* **25,** 1157–74 (2004).

141. Burlatsky, S., Darling, R. M., Novikov, D., Atrazhev, V. V., Sultanov, V. I., Astakhova, T. Y., Su, L. & Brushett, F. Molecular Dynamics Modeling of the Conductivity of Lithiated Nafion Containing Nonaqueous Solvents. *Journal of The Electrochemical Society* **163,** A2232–A2239 (2016).

142. Chen, X., Hou, T., Persson, K. A. & Zhang, Q. Combining theory and experiment in lithium–sulfur batteries: Current progress and future perspectives. *Materials Today* **22,** 142–158 (2019).

143. Fortunato, B., Mirone, P. & Fini, G. Infrared and Raman spectra and vibrational assignment of ethylene carbonate. *Spectrochimica Acta Part A: Molecular Spectroscopy* **27,** 1917–1927 (1971).

144. Allen, J. L., Borodin, O., Seo, D. M. & Henderson, W. A. Combined quantum chemical/Raman spectroscopic analyses of Li^+ cation solvation: Cyclic carbonate solvents— Ethylene carbonate and propylene carbonate. *Journal of Power Sources* **267,** 821–830 (2014).

145. Horowitz, Y., Han, H. L., Soto, F. A., Ralston, W. T., Balbuena, P. B. & Somorjai, G. A. Fluoroethylene Carbonate as a Directing Agent in Amorphous Silicon Anodes: Electrolyte Interface Structure Probed by Sum Frequency Vibrational Spectroscopy and Ab Initio Molecular Dynamics. *Nano Letters* **18,** 1145–1151 (2018).

146. Horowitz, Y., Steinruck, H. G., Han, H. L., Cao, C., Abate, I., Tsao, Y., Toney, M. F. & Somorjai, G. A. Fluoroethylene Carbonate Induces Ordered Electrolyte Interface on Silicon and Sapphire Surfaces as Revealed by Sum Frequency Generation Vibrational Spectroscopy and X-ray Reflectivity. *Nano Letters* **18,** 2105–2111 (2018).

147. Soetens, J. C., Millot, C. & Maigret, B. Molecular dynamics simulation of $Li^+BF_4^-$ in ethylene carbonate, propylene carbonate, and dimethyl carbonate solvents. *Journal of Physical Chemistry A* **102,** 1055–1061 (1998).

148. Skarmoutsos, I., Ponnuchamy, V., Vetere, V. & Mossa, S. Li^+ Solvation in Pure, Binary, and Ternary Mixtures of Organic Carbonate Electrolytes. *The Journal of Physical Chemistry C* **119,** 4502–4515 (2015).

149. Liang, C., Kwak, K. & Cho, M. Revealing the Solvation Structure and Dynamics of Carbonate Electrolytes in Lithium-Ion Batteries by Two-Dimensional Infrared Spectrum Modeling. *The Journal of Physical Chemistry Letters* **8,** 5779–5784 (2017).

150. Seo, D. M., Reininger, S., Kutcher, M., Redmond, K., Euler, W. B. & Lucht, B. L. Role of Mixed Solvation and Ion Pairing in the Solution Structure of Lithium Ion Battery Electrolytes. *The Journal of Physical Chemistry C* **119,** 14038–14046 (2015).

151. Bogle, X., Vazquez, R., Greenbaum, S., Cresce, A. & Xu, K. Understanding Li^+-Solvent Interaction in Nonaqueous Carbonate Electrolytes with ^{17}O NMR. *The Journal of Physical Chemistry Letters* **4,** 1664–8 (2013).

152. Ganesh, P., Jiang, D. E. & Kent, P. R. Accurate static and dynamic properties of liquid electrolytes for Li-ion batteries from ab initio molecular dynamics. *The Journal of Physical Chemistry B* **115,** 3085–90 (2011).

153. Chaudhari, M. I., Nair, J. R., Pratt, L. R., Soto, F. A., Balbuena, P. B. & Rempe, S. B. Scaling Atomic Partial Charges of Carbonate Solvents for Lithium Ion Solvation and Diffusion. *Journal of Chemical Theory and Computation* **12,** 5709–5718 (2016).

154. Jorn, R., Kumar, R., Abraham, D. P. & Voth, G. A. Atomistic Modeling of the Electrode–Electrolyte Interface in Li-Ion Energy Storage Systems: Electrolyte Structuring. *The Journal of Physical Chemistry C* **117,** 3747–3761 (2013).

155. Xia, J., Petibon, R., Xiao, A., Lamanna, W. M. & Dahn, J. R. Some Fluorinated Carbonates as Electrolyte Additives for Li(Ni$_{0.4}$Mn$_{0.4}$Co$_{0.2}$)O$_2$/Graphite Pouch Cells. *Journal of The Electrochemical Society* **163,** A1637–A1645 (2016).

156. Von Wald Cresce, A., Borodin, O. & Xu, K. Correlating Li$^+$ Solvation Sheath Structure with Interphasial Chemistry on Graphite. *The Journal of Physical Chemistry C* **116,** 26111–26117 (2012).

157. Xia, J., Petibon, R., Xiong, D., Ma, L. & Dahn, J. R. Enabling linear alkyl carbonate electrolytes for high voltage Li-ion cells. *Journal of Power Sources* **328,** 124–135 (2016).

158. Leung, K. Predicting the voltage dependence of interfacial electrochemical processes at lithium-intercalated graphite edge planes. *Physical Chemistry Chemical Physics* **17,** 1637–43 (2015).

159. Etacheri, V., Haik, O., Goffer, Y., Roberts, G. A., Stefan, I. C., Fasching, R. & Aurbach, D. Effect of fluoroethylene carbonate (FEC) on the performance and surface chemistry of Si-nanowire Li-ion battery anodes. *Langmuir* **28,** 965–76 (2012).

160. Markevich, E., Fridman, K., Sharabi, R., Elazari, R., Salitra, G., Gottlieb, H. E., Gershinsky, G., Garsuch, A., Semrau, G., Schmidt, M. A. & Aurbach, D. Amorphous Columnar Silicon Anodes for Advanced High Voltage Lithium Ion Full Cells: Dominant Factors Governing Cycling Performance. *Journal of The Electrochemical Society* **160,** A1824–A1833 (2013).

161. Kim, K., Park, I., Ha, S.-Y., Kim, Y., Woo, M.-H., Jeong, M.-H., Shin, W. C., Ue, M., Hong, S. Y. & Choi, N.-S. Understanding the thermal instability of fluoroethylene carbonate in LiPF$_6$-based electrolytes for lithium ion batteries. *Electrochimica Acta* **225,** 358–368 (2017).

162. Sodeyama, K., Yamada, Y., Aikawa, K., Yamada, A. & Tateyama, Y. Sacrificial Anion Reduction Mechanism for Electrochemical Stability Improvement in Highly Concentrated Li-Salt Electrolyte. *The Journal of Physical Chemistry C* **118,** 14091–14097 (2014).

163. Yohannes, Y. B., Lin, S. D. & Wu, N.-L. In Situ DRIFTS Analysis of Solid Electrolyte Interphase of Si-Based Anode with and without Fluoroethylene Carbonate Additive. *Journal of The Electrochemical Society* **164,** A3641–A3648 (2017).

164. Horowitz, Y., Han, H. L., Ralston, W. T., de Araujo, J. R., Kreidler, E., Brooks, C. & Somorjai, G. A. Fluorinated End-Groups in Electrolytes Induce Ordered Electrolyte/Anode Interface Even at Open-Circuit Potential as Revealed by Sum Frequency Generation Vibrational Spectroscopy. *Advanced Energy Materials* **7,** 1602060 (2017).

165. Pekarek, R. T., Affolter, A., Baranowski, L. L., Coyle, J., Hou, T., Sivonxay, E., Smith, B. A., McAuliffe, R. D., Persson, K. A., Key, B., Apblett, C., Veith, G. M. & Neale, N. R. Intrinsic chemical reactivity of solid-electrolyte interphase components in silicon–lithium alloy anode batteries probed by FTIR spectroscopy. *Journal of Materials Chemistry A* **8,** 7897–7906 (2020).

166. Giorgini, M. G., Futamatagawa, K., Torii, H., Musso, M. & Cerini, S. Solvation Structure around the Li^+ Ion in Mixed Cyclic/Linear Carbonate Solutions Unveiled by the Raman Noncoincidence Effect. *The Journal of Physical Chemistry Letters* **6,** 3296–3302 (2015).

167. Hou, T., Yang, G., Rajput, N. N., Self, J., Park, S.-W., Nanda, J. & Persson, K. A. The influence of FEC on the solvation structure and reduction reaction of $LiPF_6$/EC electrolytes and its implication for solid electrolyte interphase formation. *Nano Energy* **64** (2019).

168. Su, C. C., He, M., Amine, R., Chen, Z. & Amine, K. The Relationship between the Relative Solvating Power of Electrolytes and Shuttling Effect of Lithium Polysulfides in Lithium-Sulfur Batteries. *Angewandte Chemie International Edition* **57,** 12033–12036 (2018).

169. Zhang, X. & Kuroda, D. G. An ab initio molecular dynamics study of the solvation structure and ultrafast dynamics of lithium salts in organic carbonates: A comparison between linear and cyclic carbonates. *The Journal of Chemical Physics* **150,** 184501 (2019).

170. Tang, Z. K., Tse, J. S. & Liu, L. M. Unusual Li-Ion Transfer Mechanism in Liquid Electrolytes: A First-Principles Study. *The Journal of Physical Chemistry Letters* **7,** 4795–4801 (2016).

171. Vatamanu, J., Borodin, O. & Smith, G. D. Molecular Dynamics Simulation Studies of the Structure of a Mixed Carbonate/$LiPF_6$ Electrolyte near Graphite Surface as a Function of Electrode Potential. *The Journal of Physical Chemistry C* **116,** 1114–1121 (2011).

172. Boyer, M. J., Vilciauskas, L. & Hwang, G. S. Structure and $LiPF_6$ ion transport in a mixed carbonate/$LiPF_6$ electrolyte near graphite electrode surfaces: a molecular dynamics study. *Physical Chemistry Chemical Physics* **18,** 27868–27876 (2016).

173. Shim, Y. Computer simulation study of the solvation of lithium ions in ternary mixed carbonate electrolytes: free energetics, dynamics, and ion transport. *Physical Chemistry Chemical Physics* **20,** 28649–28657 (2018).

174. France-Lanord, A. & Grossman, J. C. Correlations from Ion Pairing and the Nernst-Einstein Equation. *Physical Review Letters* **122,** 136001 (2019).

175. Liu, H. & Maginn, E. A molecular dynamics investigation of the structural and dynamic properties of the ionic liquid 1-n-butyl-3-methylimidazolium bis(trifluoromethanesulfonyl)imide. *The Journal of Chemical Physics* **135,** 124507 (2011).

176. Borodin, O., Gorecki, W., Smith, G. D. & Armand, M. Molecular dynamics simulation and pulsed-field gradient NMR studies of bis(fluorosulfonyl)imide (FSI) and bis[(trifluoromethyl)sulfonyl]imide (TFSI)-based ionic liquids. *The Journal of Physical Chemistry B* **114,** 6786–98 (2010).

177. Borodin, O., Smith, G. D. & Fan, P. Molecular dynamics simulations of lithium alkyl carbonates. *The Journal of Physical Chemistry B* **110,** 22773–9 (2006).

178. Cheng, X. B., Zhang, R., Zhao, C. Z., Wei, F., Zhang, J. G. & Zhang, Q. A Review of Solid Electrolyte Interphases on Lithium Metal Anode. *Advanced Science* **3,** 1500213 (2016).

179. Zhuang, G. R. V., Xu, K., Yang, H., Jow, T. R. & Ross, P. N. Lithium ethylene dicarbonate identified as the primary product of chemical and electrochemical reduction of EC in 1.2 m $LiPF_6$/EC : EMC electrolyte. *Journal of Physical Chemistry B* **109,** 17567–17573 (2005).

180. Wang, Y., Nakamura, S., Ue, M. & Balbuena, P. B. Theoretical Studies To Understand Surface Chemistry on Carbon Anodes for Lithium-Ion Batteries: Reduction Mechanisms of Ethylene Carbonate. *Journal of the American Chemical Society* **123,** 11708–11718 (2001).

181. Yang, C. R., Wang, Y. Y. & Wan, C. C. Composition analysis of the passive film on the carbon electrode of a lithium-ion battery with an EC-based electrolyte. *Journal of Power Sources* **72,** 66–70 (1998).

182. Michaud-Agrawal, N., Denning, E. J., Woolf, T. B. & Beckstein, O. MDAnalysis: a toolkit for the analysis of molecular dynamics simulations. *Journal of Computational Chemistry* **32,** 2319–27 (2011).

183. Grimme, S., Antony, J., Ehrlich, S. & Krieg, H. A consistent and accurate ab initio parametrization of density functional dispersion correction (DFT-D) for the 94 elements H-Pu. *The Journal of Chemical Physics* **132,** 154104 (2010).

184. Grimme, S., Ehrlich, S. & Goerigk, L. Effect of the damping function in dispersion corrected density functional theory. *Journal of Computational Chemistry* **32,** 1456–65 (2011).

185. Goerigk, L. & Grimme, S. Efficient and Accurate Double-Hybrid-Meta-GGA Density Functionals-Evaluation with the Extended GMTKN30 Database for General Main Group Thermochemistry, Kinetics, and Noncovalent Interactions. *Journal of Chemical Theory and Computation* **7,** 291–309 (2011).

186. Grimme, S. Semiempirical hybrid density functional with perturbative second-order correlation. *The Journal of Chemical Physics* **124,** 034108 (2006).

187. Tomasi, J., Mennucci, B. & Cances, E. The IEF version of the PCM solvation method: an overview of a new method addressed to study molecular solutes at the QM ab initio level. *Journal of Molecular Structure-Theochem* **464,** 211–226 (1999).

188. Tomasi, J., Mennucci, B. & Cammi, R. Quantum mechanical continuum solvation models. *Chemical Reviews* **105,** 2999–3093 (2005).

189. Grimme, S. Supramolecular binding thermodynamics by dispersion-corrected density functional theory. *Chemistry—A European Journal* **18,** 9955–64 (2012).

190. Luchini, G., Alegre-Requena, J. V., Funes-Ardoiz, I. & Paton, R. S. GoodVibes: automated thermochemistry for heterogeneous computational chemistry data. *F1000Research* **9** (2020).

191. Shao, Y. *et al.* Advances in molecular quantum chemistry contained in the Q-Chem 4 program package. *Molecular Physics* **113,** 184–215 (2014).

192. Hagos, T. T., Thirumalraj, B., Huang, C. J., Abrha, L. H., Hagos, T. M., Berhe, G. B., Bezabh, H. K., Cherng, J., Chiu, S. F., Su, W. N. & Hwang, B. J. Locally Concentrated $LiPF_6$ in a Carbonate-Based Electrolyte with Fluoroethylene Carbonate as a Diluent for Anode-Free Lithium Metal Batteries. *ACS Applied Materials & Interfaces* **11,** 9955–9963 (2019).

193. Leontyev, I. & Stuchebrukhov, A. Accounting for electronic polarization in non-polarizable force fields. *Physical Chemistry Chemical Physics* **13,** 2613–26 (2011).

194. Chaban, V. Polarizability versus mobility: atomistic force field for ionic liquids. *Physical Chemistry Chemical Physics* **13,** 16055–62 (2011).

195. Ringsby, A. J., Fong, K. D., Self, J., Bergstrom, H. K., McCloskey, B. D. & Persson, K. A. Transport Phenomena in Low Temperature Lithium-Ion Battery Electrolytes. *Journal of the Electrochemical Society* **168,** 080501 (2021).

196. Gudla, H., Zhang, C. & Brandell, D. Effects of Solvent Polarity on Li-ion Diffusion in Polymer Electrolytes: An All-Atom Molecular Dynamics Study with Charge Scaling. *The Journal of Physical Chemistry B* **124,** 8124–8131 (2020).

197. Xia, L., Tang, B., Yao, L., Wang, K., Cheris, A., Pan, Y., Lee, S., Xia, Y., Chen, G. Z. & Liu, Z. Oxidation Decomposition Mechanism of Fluoroethylene Carbonate-Based Electrolytes for High-Voltage Lithium Ion Batteries: A DFT Calculation and Experimental Study. *ChemistrySelect* **2,** 7353–7361 (2017).

198. Liao, L., Cheng, X., Ma, Y., Zuo, P., Fang, W., Yin, G. & Gao, Y. Fluoroethylene carbonate as electrolyte additive to improve low temperature performance of $LiFePO_4$ electrode. *Electrochimica Acta* **87,** 466–472 (2013).

199. Ma, L., Glazier, S. L., Petibon, R., Xia, J., Peters, J. M., Liu, Q., Allen, J., Doig, R. N. C. & Dahn, J. R. A Guide to Ethylene Carbonate-Free Electrolyte Making for Li-Ion Cells. *Journal of The Electrochemical Society* **164,** A5008–A5018 (2016).

200. Horowitz, Y., Han, H. L., Ross, P. N. & Somorjai, G. A. In Situ Potentiodynamic Analysis of the Electrolyte/Silicon Electrodes Interface Reactions–A Sum Frequency Generation Vibrational Spectroscopy Study. *Journal of the American Chemical Society* **138,** 726–9 (2016).

201. Kamphaus, E. P., Angarita-Gomez, S., Qin, X., Shao, M., Engelhard, M., Mueller, K. T., Murugesan, V. & Balbuena, P. B. Role of Inorganic Surface Layer on Solid Electrolyte Interphase Evolution at Li-Metal Anodes. *ACS Applied Materials & Interfaces* **11,** 31467–31476 (2019).

202. Liu, Z., Qi, Y., Lin, Y. X., Chen, L., Lu, P. & Chen, L. Q. Interfacial Study on Solid Electrolyte Interphase at Li Metal Anode: Implication for Li Dendrite Growth. *Journal of The Electrochemical Society* **163,** A592–A598 (2016).

203. Nanda, J., Yang, G., Hou, T. Z., Voylov, D. N., Li, X., Ruther, R. E., Naguib, M., Persson, K., Veith, G. M. & Sokolov, A. P. Unraveling the Nanoscale Heterogeneity of Solid Electrolyte Interphase Using Tip-Enhanced Raman Spectroscopy. *Joule* **3,** 2001–2019 (2019).

204. Aurbach, D., Markovsky, B., Shechter, A., EinEli, Y. & Cohen, H. A comparative study of synthetic graphite and Li electrodes in electrolyte solutions based on ethylene carbonate dimethyl carbonate mixtures. *Journal of the Electrochemical Society* **143,** 3809–3820 (1996).

205. Browning, K. L., Sacci, R. L., Doucet, M., Browning, J. F., Kim, J. R. & Veith, G. M. The Study of the Binder Poly(acrylic acid) and Its Role in Concomitant Solid-Electrolyte Interphase Formation on Si Anodes. *ACS Applied Materials & Interfaces* **12,** 10018–10030 (2020).

206. Schnabel, M., Arca, E., Ha, Y., Stetson, C., Teeter, G., Han, S.-D. & Stradins, P. Enhanced Interfacial Stability of Si Anodes for Li-Ion Batteries via Surface SiO_2 Coating. *ACS Applied Energy Materials* **3,** 8842–8849 (2020).

207. Li, Z., Stetson, C., Teeter, G., Norman, A., Ha, Y., Tremolet de Villers, B. J., Huey, Z., Walker, P., Han, S.-D., DeCaluwe, S. C., Jiang, C.-S., Burrell, A. K. & Zakutayev, A. Improving Interface Stability of Si Anodes by Mg Coating in Li-Ion Batteries. *ACS Applied Energy Materials* **3,** 11534–11539 (2020).

208. Ha, Y., Stetson, C., Harvey, S. P., Teeter, G., Tremolet de Villers, B. J., Jiang, C. S., Schnabel, M., Stradins, P., Burrell, A. & Han, S. D. Effect of Water Concentration in $LiPF_6$-Based Electrolytes on the Formation, Evolution, and Properties of the Solid Electrolyte Interphase on Si Anodes. *ACS Applied Materials & Interfaces* **12,** 49563–49573 (2020).

209. Cui, X., Tang, F., Zhang, Y., Li, C., Zhao, D., Zhou, F., Li, S. & Feng, H. Influences of trace water on electrochemical performances for lithium hexafluoro phosphate- and lithium Bis(oxalato)borate-based electrolytes. *Electrochimica Acta* **273,** 191–199 (2018).

210. Furukawa, H., Cordova, K. E., O'Keeffe, M. & Yaghi, O. M. The chemistry and applications of metal–organic frameworks. *Science* **341,** 1230444 (2013).

211. Hou, T., Fong, K., Wang, J. & Persson, K. The Solvation Structure, Transport Properties and Reduction Behavior of Carbonate-Based Electrolytes of Lithium-Ion Batteries. *Chemical Science,* DOI: 10.1039/D1SC04265C (2021).

212. Pillai, R. S., Jobic, H., Koza, M. M., Nouar, F., Serre, C., Maurin, G. & Ramsahye, N. A. Diffusion of Carbon Dioxide and Nitrogen in the Small-Pore Titanium Bis(phosphonate) Metal–Organic Framework MIL-91 (Ti): A Combination of Quasielastic Neutron Scattering Measurements and Molecular Dynamics Simulations. *ChemPhysChem* **18,** 2739–2746 (2017).

213. Giacobbe, C., Lavigna, E., Maspero, A. & Galli, S. Elucidating the CO_2 adsorption mechanisms in the triangular channels of the bis(pyrazolate) MOF $Fe_2(BPEB)_3$ by in situ synchrotron X-ray diffraction and molecular dynamics simulations. *Journal of Materials Chemistry A* **5,** 16964–16975 (2017).

214. Rappe, A. K., Casewit, C. J., Colwell, K. S., Goddard, W. A. & Skiff, W. M. UFF, a full periodic table force field for molecular mechanics and molecular dynamics simulations. *Journal of the American Chemical Society* **114,** 10024–10035 (1992).

215. Frenkel, D. & Smit, B. *Understanding Molecular Simulation (Second Edition)* (Academic Press, San Diego, 2002).

216. Woon, D. E. & Dunning, T. H. Gaussian basis sets for use in correlated molecular calculations. III. The atoms aluminum through argon. *The Journal of Chemical Physics* **98,** 1358–1371 (1993).

217. Kendall, R. A., Dunning, T. H. & Harrison, R. J. Electron affinities of the first-row atoms revisited. Systematic basis sets and wave functions. *The Journal of Chemical Physics* **96,** 6796–6806 (1992).

218. Hay, P. J. & Wadt, W. R. Ab initio effective core potentials for molecular calculations. Potentials for K to Au including the outermost core orbitals. *The Journal of Chemical Physics* **82,** 299–310 (1985).

219. Roy, L. E., Hay, P. J. & Martin, R. L. Revised Basis Sets for the LANL Effective Core Potentials. *Journal of Chemical Theory and Computation* **4,** 1029–31 (2008).

220. Mehrer, H. *Diffusion in Solids: Fundamentals, Methods, Materials, Diffusion-Controlled Processes* (Springer-Verlag, Berlin Heidelberg, 2007).

221. Borodin, O., Self, J., Persson, K. A., Wang, C. & Xu, K. Uncharted Waters: Super-Concentrated Electrolytes. *Joule* **4,** 69–100 (2020).

222. Self, J., Fong, K. D. & Persson, K. A. Transport in Superconcentrated $LiPF_6$ and $LiBF_4$/Propylene Carbonate Electrolytes. *ACS Energy Letters* **4,** 2843–2849 (2019).

223. Yaghi, O. M. A tale of two entanglements. *Nature Materials* **6,** 92–93 (2007).

224. Shekhah, O., Wang, H., Paradinas, M., Ocal, C., Schüpbach, B., Terfort, A., Zacher, D., Fischer, R. A. & Wöll, C. Controlling interpenetration in metal–organic frameworks by liquid-phase epitaxy. *Nature Materials* **8,** 481–484 (2009).

225. Rosen, A. S., Mian, M. R., Islamoglu, T., Chen, H., Farha, O. K., Notestein, J. M. & Snurr, R. Q. Tuning the Redox Activity of Metal–Organic Frameworks for Enhanced, Selective O_2 Binding: Design Rules and Ambient Temperature O_2 Chemisorption in a Cobalt–Triazolate Framework. *Journal of the American Chemical Society* **142,** 4317–4328 (2020).

226. Rosen, A. S., Iyer, S. M., Ray, D., Yao, Z., Aspuru-Guzik, A., Gagliardi, L., Notestein, J. M. & Snurr, R. Q. Machine learning the quantum-chemical properties of metal–organic frameworks for accelerated materials discovery. *Matter* **4,** 1578–1597 (2021).

Appendix A

Supplementary Materials for The Influence of Electrolyte Additives in Unary Cyclic Carbonate Electrolytes

a

b
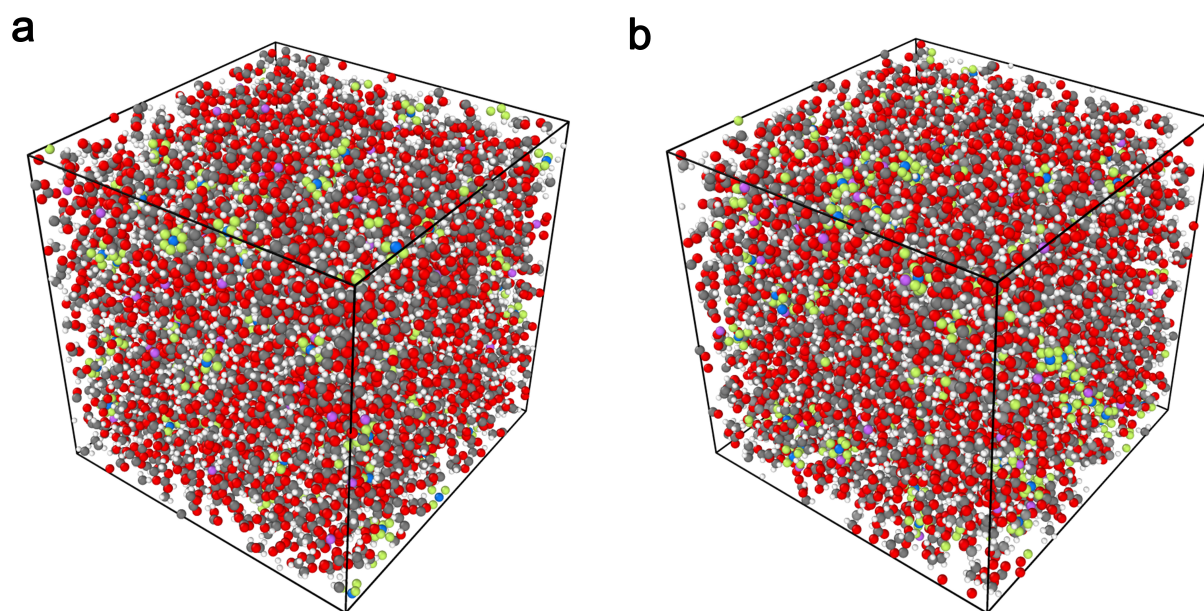
Figure A.1 The MD simulation box of (a) 1.0 M $LiPF_6$ in EC and (b) 1.0 M $LiPF_6$ in EC with 10% FEC
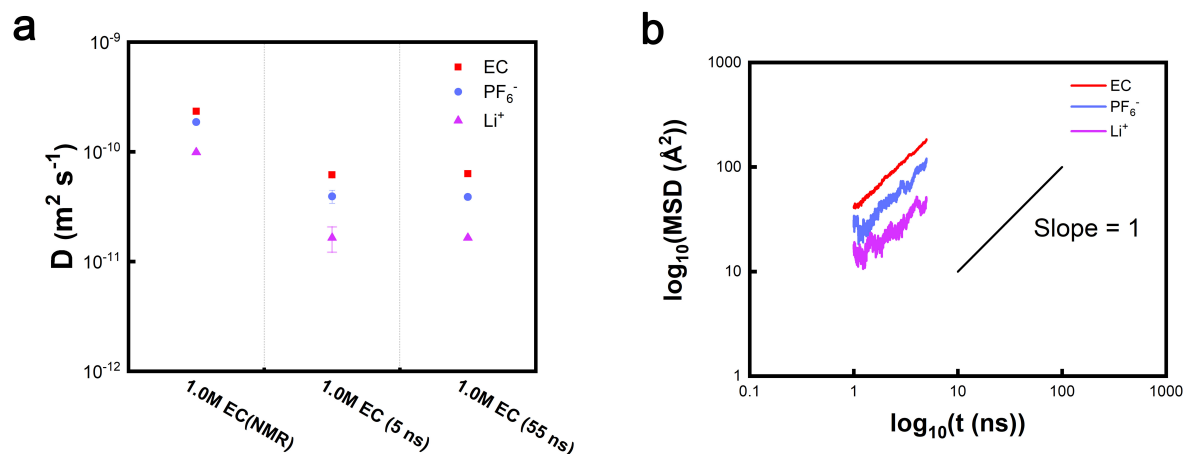
Figure A.2 (a) Self-diffusion coefficients of 1.0 M LiPF$_6$ in EC computed from 5 ns and 55 ns MD simulations as compared with NMR experiments (1.0 M LiPF$_6$ in EC) from Hayamizu et al. [137] The error bars of the 5 ns production run represent the standard deviation of the data collected every 1 ns. (b) Log-log scale plots of mean squared displacement (MSD) of EC, PF$_6^-$, and Li$^+$ in 1.0 M LiPF$_6$ in EC show the slope of 1 indicating diffusive regime within 5 ns.

We obtained 55 ns trajectories for 1.0 M LiPF$_6$ in EC solution. Figure A.2a shows the comparison of diffusion coefficient obtained from 5 ns and 55 ns trajectory with the diffusion coefficients obtained from NMR experiments. The difference between simulation and experiment is within one order of magnitude, which is within acceptable agreement considering the non-polarizable force field used in this work.[1] The Nernst–Einstein relation was used to measure the diffusion coefficient from the mean squared displacement of atoms. The resulting coefficient is fitted from a least squares minimization for a straight line for a time period in the diffusion regime and then averaged over two independent realizations of the same system. Single particle dynamics obtained from mean square displacement (MSD) can be divided into three regimes (1) ballistic at short timescales when the ions have not interacted much with their neighbors (MSD $\propto t^2$) (2) subdiffusive at intermediate times where ions rattle inside a cage formed by their neighbors (MSD $\propto t^\alpha$, $0 < \alpha < 1$), and when the ions escape from these cages, they reach the diffusive or Fickian regime at increased timescales (MSD $\propto t$). In this work we only captured the behavior in the diffusive regime.[2] Figure S2b shows the log-log plot of MSD obtained from 5 ns production run. It can be seen that the MSD is proportional to t with slope = 1, suggesting that the diffusion coefficients reported in Figure 3.3 in the main text is obtained from the diffusive regime.

---

[1]Rajput N.N., Murugesan V., Shin Y., Han K.S., Lau K.C., Chen J., Liu J., Curtiss L.A., Mueller K.T. & Persson K.A. Elucidating the Solvation Structure and Dynamics of Lithium Polysulfides Resulting from Competitive Salt and Solvent Interactions. *Chemistry of Materials* **29**, 3375-3379 (2017).

[2]Del Pópolo M.G. & Voth G.A. On the Structure and Dynamics of Ionic Liquids. *The Journal of Physical Chemistry B* **108**, 1744-1752 (2004).
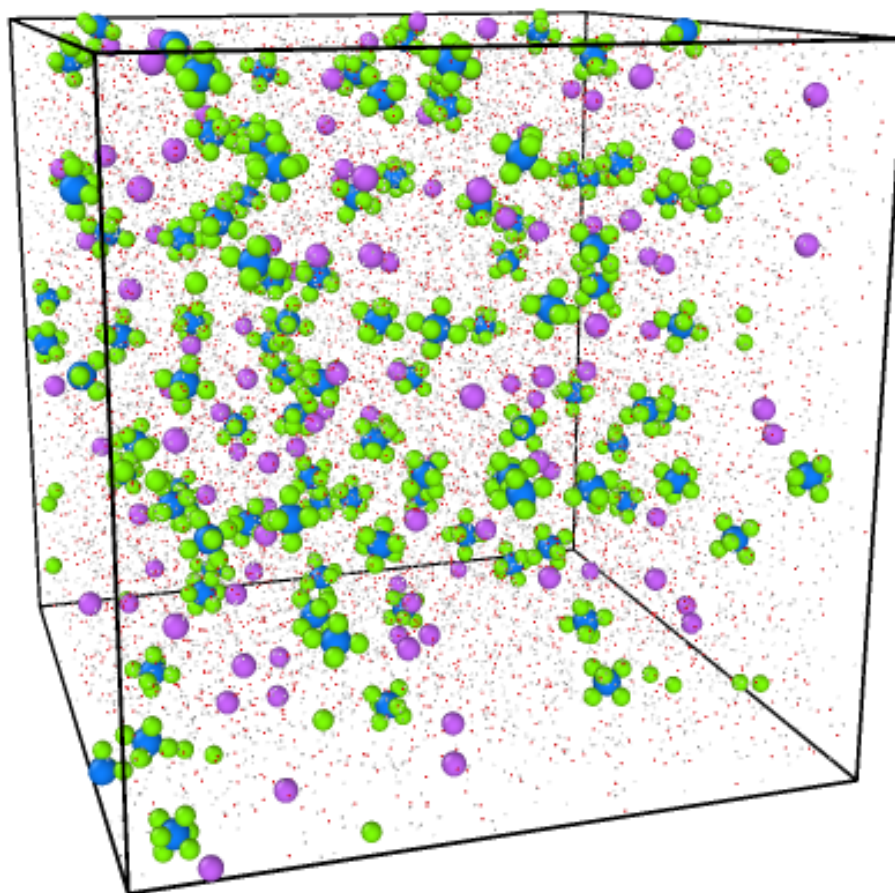
Figure A.3 The snapshot of the simulation box of 1.0 M LiPF$_6$ in EC at 10 ns.
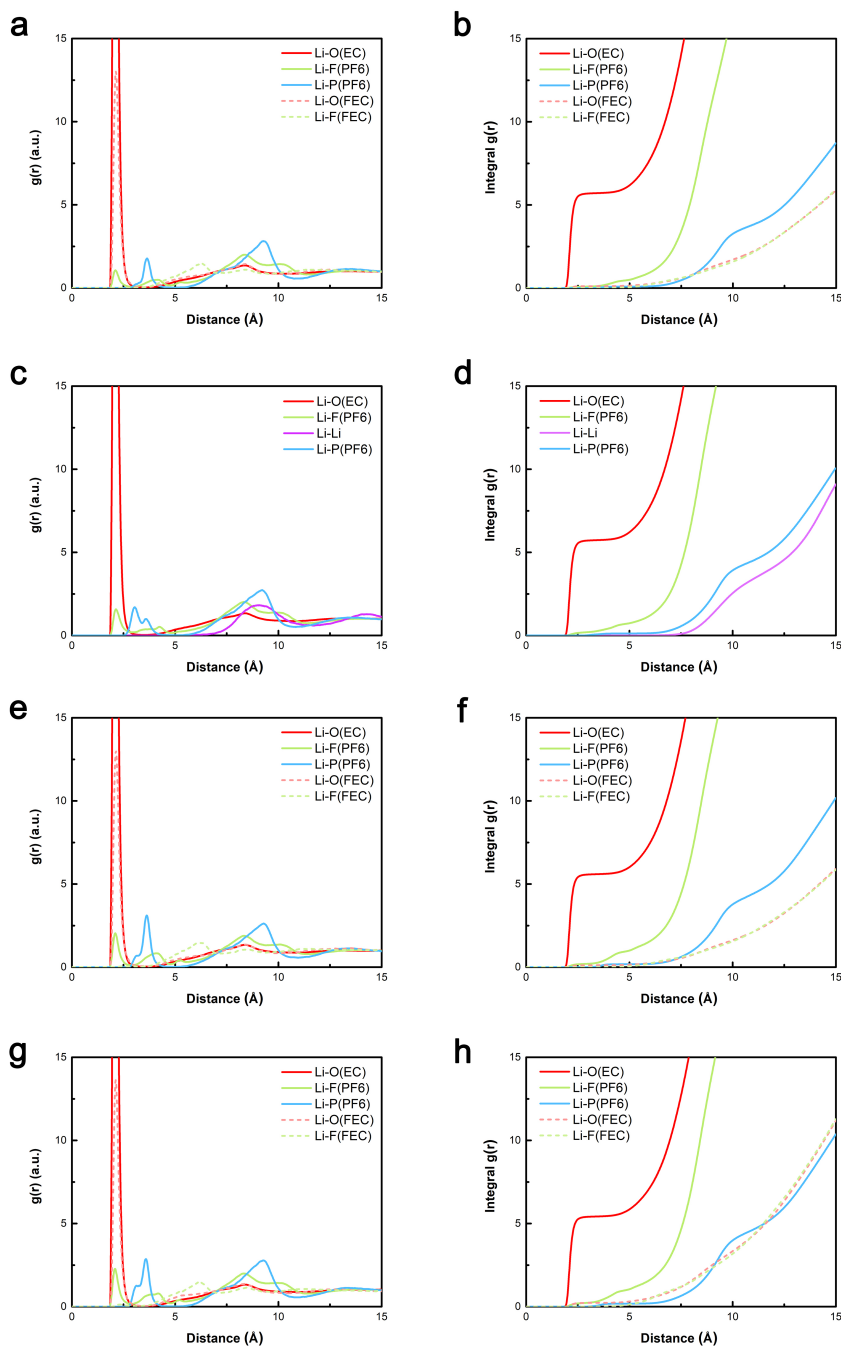
Figure A.4 Radial distribution function g(r) and the corresponding integrals (a, b) 1.0 M LiPF$_6$ in EC with 5% FEC, (c, d) 1.2 M LiPF$_6$ in EC, (e, f) 1.2 M LiPF$_6$ in EC with 5% FEC, and (g, h) 1.2 M LiPF$_6$ in EC with 10% FEC.

Table A.1 The most probable distance (D) and peak height for Li-X pairs (X = O(EC), F(PF$_6$$^-$), O(FEC)) in their corresponding RDFs.

Electrolyte	Li–O(EC)		Li–F(PF$_6$$^-$)		Li–O(FEC)	
	D (Å)	Peak height	D (Å)	Peak height	D (Å)	Peak height
1.0M EC	2.08	42.48	2.11	0.96		
1.0M EC w/ 5%FEC	2.09	43.97	2.11	1.07	2.12	13.90
1.0M EC w/ 10%FEC	2.08	45.68	2.08	2.24	2.12	12.90
1.2M EC	2.08	42.77	2.09	1.62		
1.2M EC w/ 5%FEC	2.08	43.89	2.14	2.11	2.12	14.03
1.2M EC w/ 10%FEC	2.08	45.66	2.09	2.44	2.11	14.57

Table A.2 The coordination number of Li-X pairs (X = O(EC), F(PF$_6$$^-$), Li, P(PF$_6$$^-$)), and total coordination number

Temperature (K)	Coordination number			
	O(EC)	P(PF$_6$$^-$)	F(PF$_6$$^-$)	Total
298	5.84	0.06	0.07	5.90
330	5.74	0.09	0.15	5.83
350	5.57	0.17	0.33	5.74
400	5.23	0.25	0.45	5.48
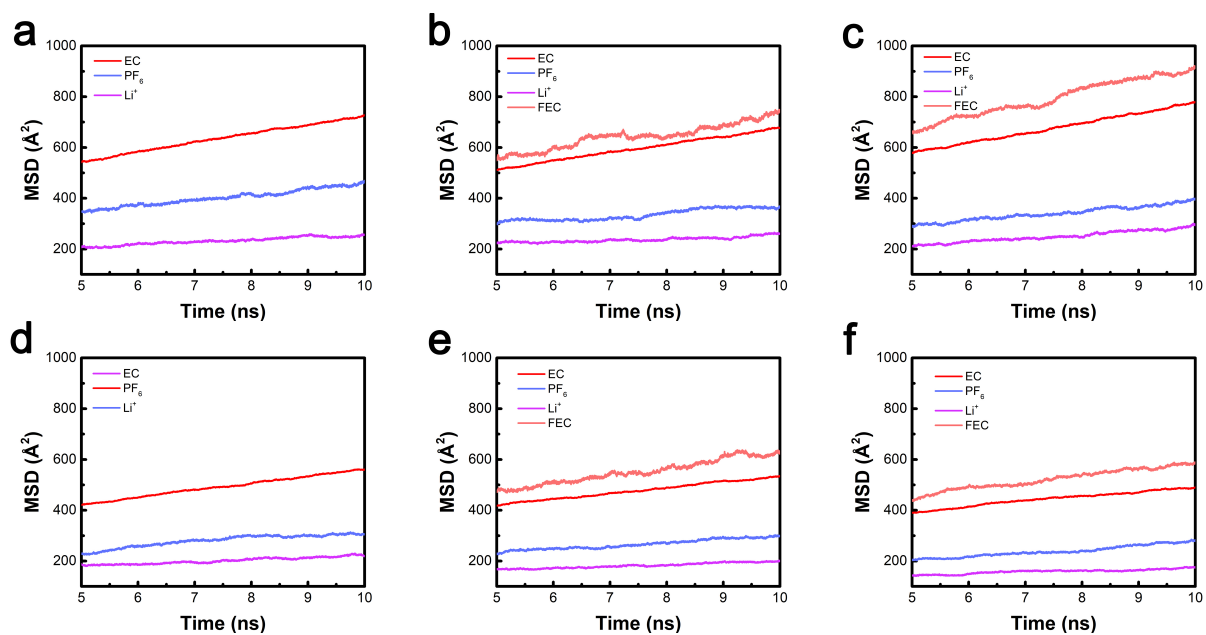
Figure A.5 The mean squared displacement (MSD) of the electrolyte components in (a) 1.0 M $LiPF_6$ in pure EC, (b) 1.0 M $LiPF_6$ in EC with 5% FEC, (c) 1.0 M $LiPF_6$ in EC with 10% FEC, (d) 1.2 M $LiPF_6$ in pure EC, (e) 1.2 M $LiPF_6$ in EC with 5% FEC, and (f) 1.2 M $LiPF_6$ in EC with 10% FEC.
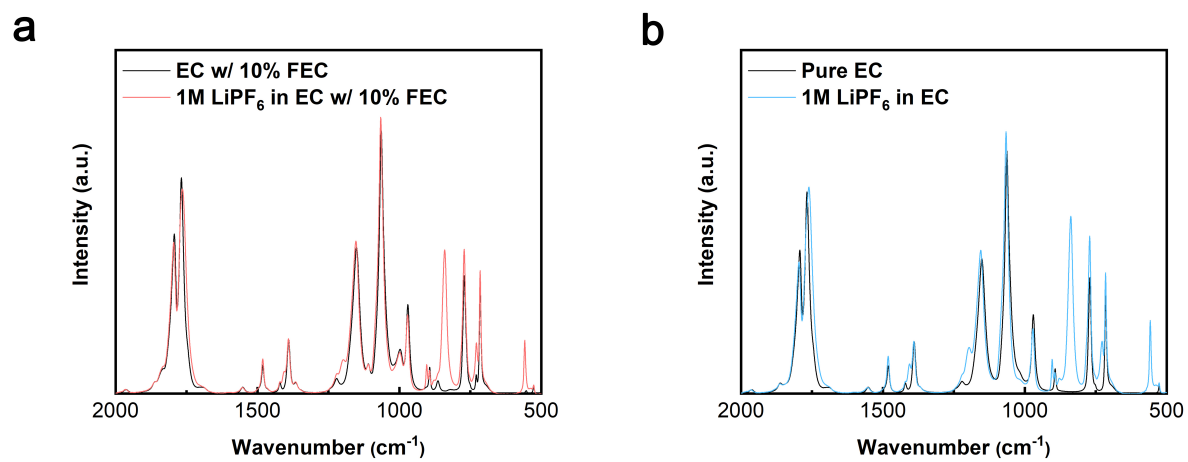
Figure A.6 The full IR spectra obtained from experiments for (a) EC electrolyte and (b) EC electrolyte with 10% FEC, with and without $LiPF_6$ salt.
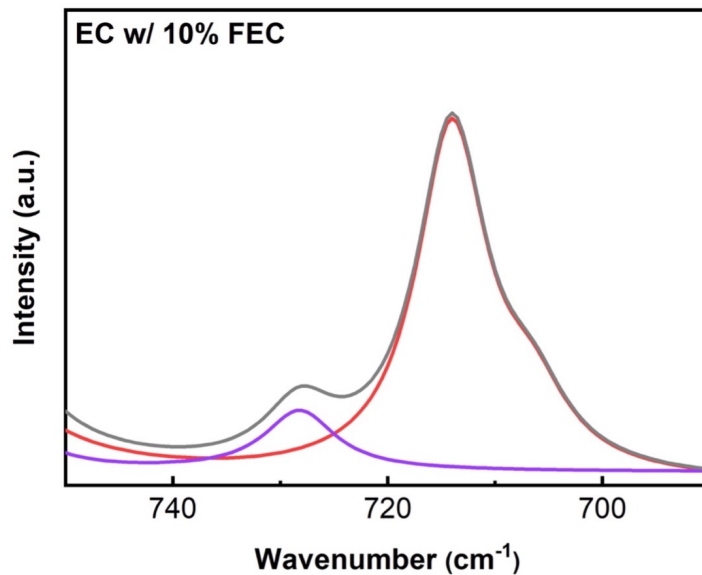
Figure A.7 Calculated FTIR spectra of the C=O breathing band of EC electrolyte with 10% FEC.
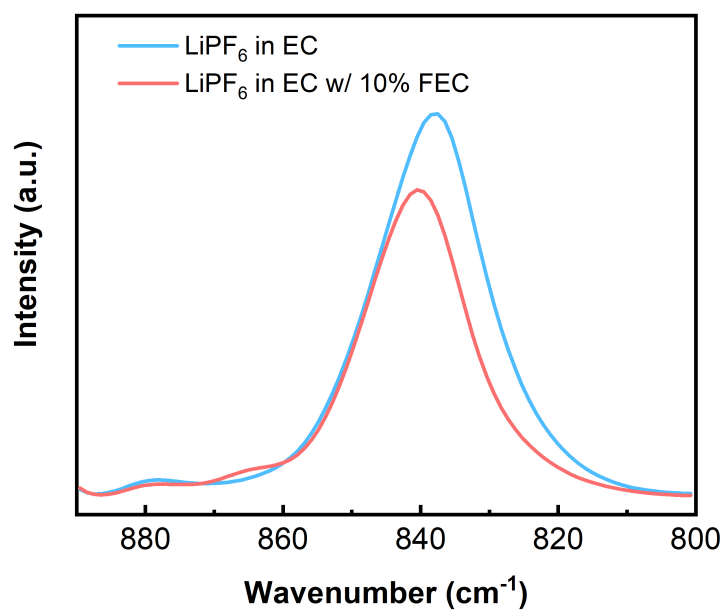
Figure A.8 Measured FTIR spectra of P–F stretching band of 1.0 M LiPF$_6$ in EC, and 1.0 M LiPF$_6$ in EC with 10% FEC.
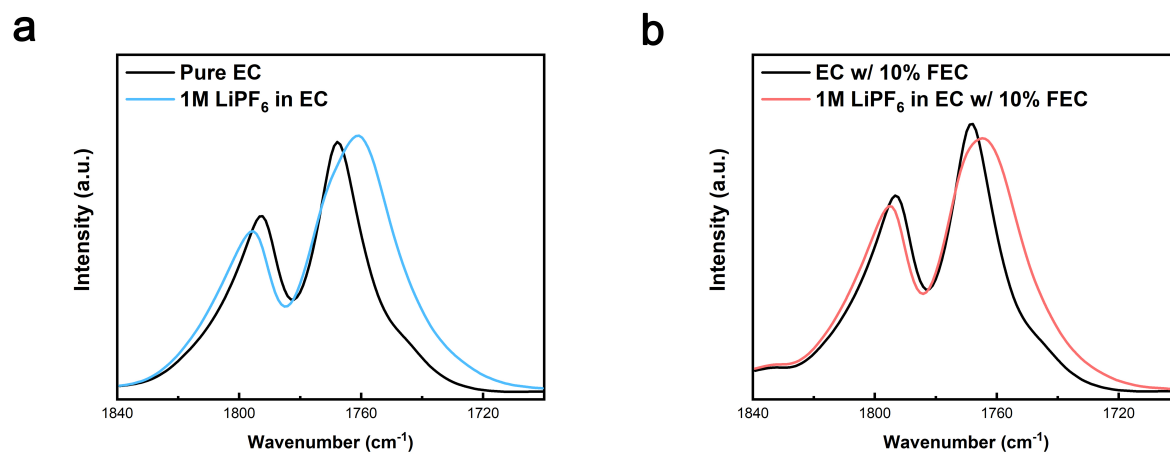
Figure A.9 Measured FTIR spectra of the C=O bond stretching band of (a) EC electrolyte, and (b) EC electrolyte with 10% FEC.
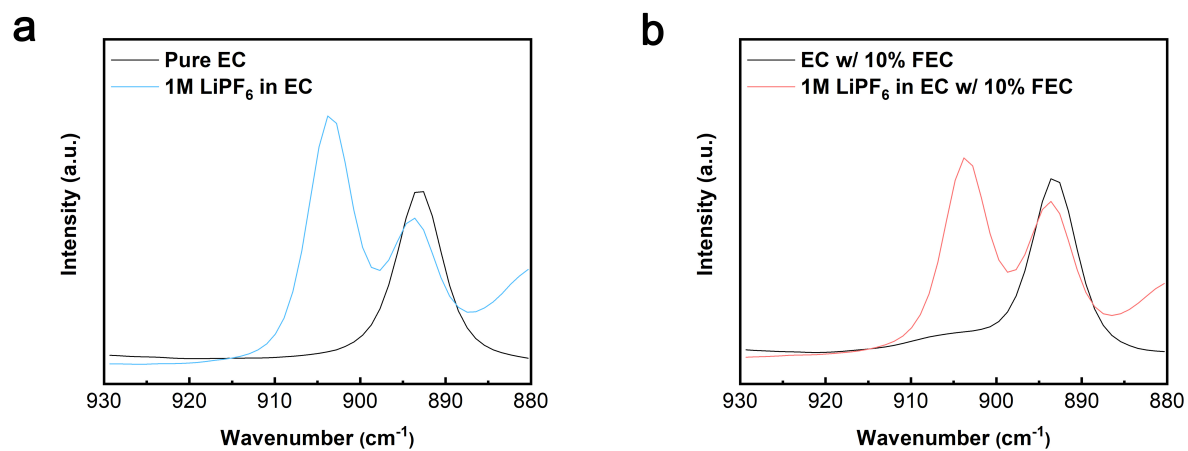
Figure A.10 Figure S10. Measured FTIR spectra of ring breathing band of (a) EC electrolyte, and (b) EC electrolyte with 10% FEC.

Appendix B

Supplementary Materials for The Modeling of Binary/Ternary Mixed-Carbonate Electrolytes
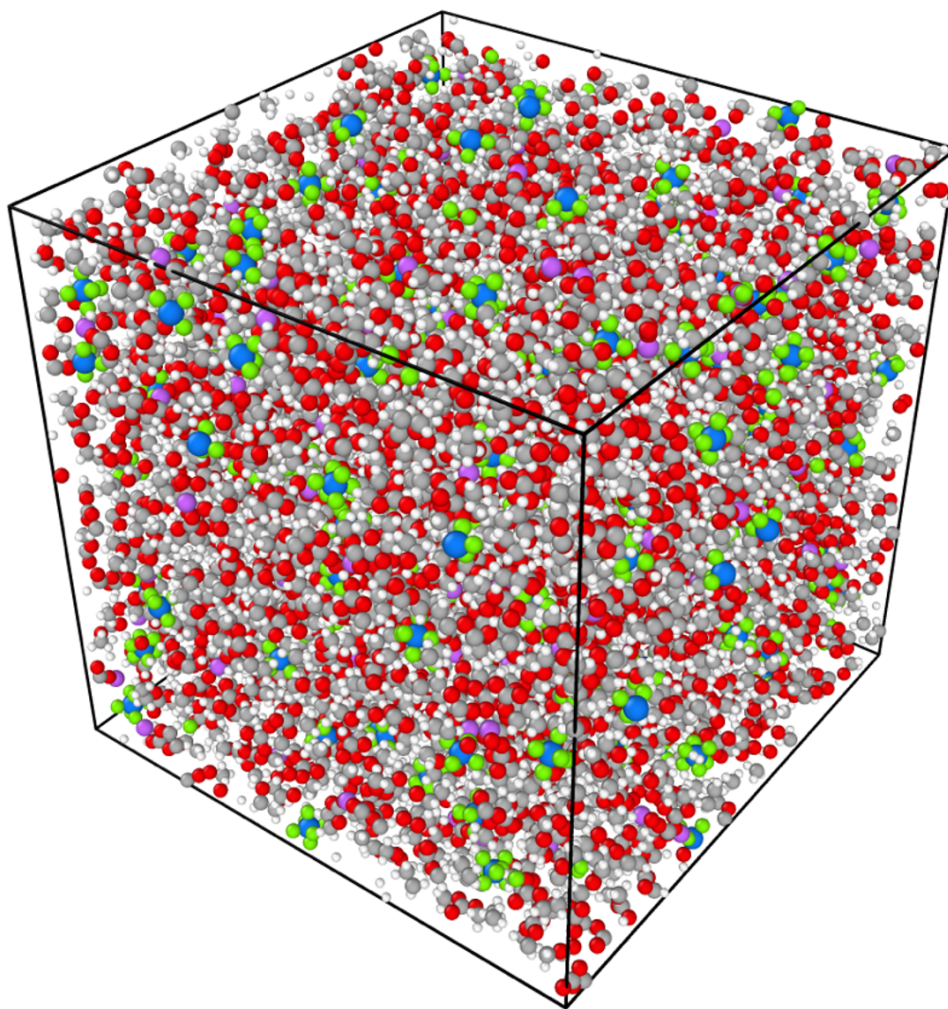
The MD simulation box

Figure B.1 The MD simulation box of the Gen2 electrolyte.

Detailed solvation structure population

Table B.1 The detailed population of species in the four electrolytes.

Electrolyte	SSIP	CIP	AGG
EC-base	90.1%± 1.0%	9.2%± 0.9%	0.7% ± 0.4%
ECF	87.5%± 0.9%	11.2%± 1.0%	1.3% ± 0.4%
Gen2	35.6%± 0.9%	33.3%± 1.3%	31.1%± 0.8%
GenF	38.4%± 2.1%	32.9%± 0.8%	28.7%± 1.9%

Table B.2 The detailed solvent-specific solvation numbers of the four electrolytes.

| Electrolyte	Solvent/salt	SSIP	CIP	AGG
EC	$LiPF_6$	0 (by definition)	1 (by definition)	1.487±0.068
	EC	5.897±0.003	4.715±0.013	4.216±0.099
ECF	$LiPF_6$	0 (by definition)	1 (by definition)	1.461±0.063
	EC	5.653±0.018	4.535±0.038	4.002±0.100
	FEC	0.234±0.016	0.177±0.025	0.152±0.061
Gen2	$LiPF_6$	0 (by definition)	1 (by definition)	1.416±0.019
	EC	2.642±0.027	1.492±0.020	1.199±0.017
	EMC	3.028±0.030	2.970±0.028	2.838±0.022
GenF	$LiPF_6$	0 (by definition)	1 (by definition)	1.443±0.020
	EC	2.381±0.056	1.407±0.018	1.115±0.023
	EMC	2.966±0.034	2.884±0.016	2.751±0.016
	FEC	0.331±0.022	0.201±0.032	0.140±0.015
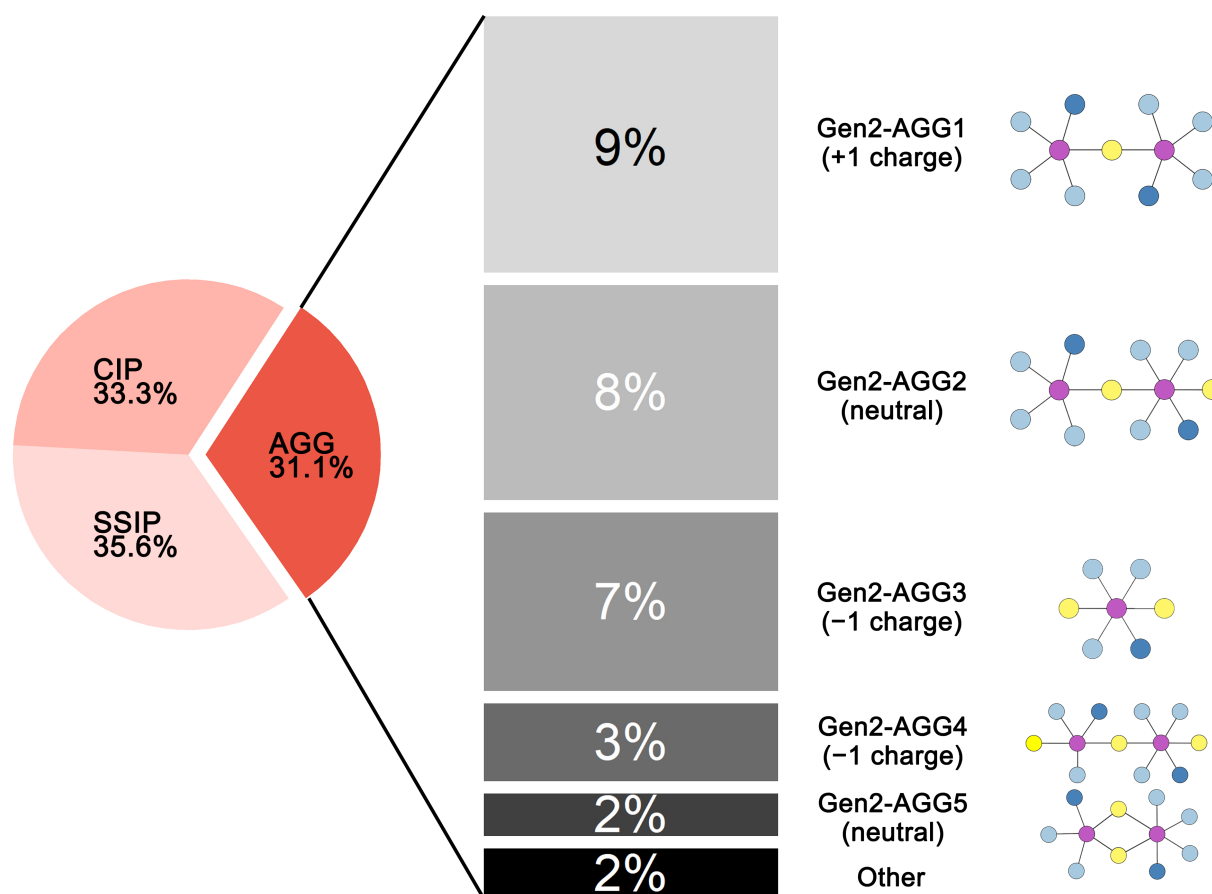
Figure B.2 AGG species in the Gen2 electrolyte. Among the 31.4% of the AGG species, 9% are AGG1 (positive triple ions) with two Li^+ and one PF_6^-. Meanwhile, the AGG2 structure with neutral charge and the AGG3 (negative triple ions) structure account for 8% and 7%, respectively. The remaining 7% consists of AGG4, AGG5, and other larger structures. Subsequently, while the EC electrolyte has a much higher SSIP ratio than the Gen2 electrolyte, more than half of the AGG species in the Gen2 electrolyte narrow the gap of the proportion of ionically conductive solvation species.

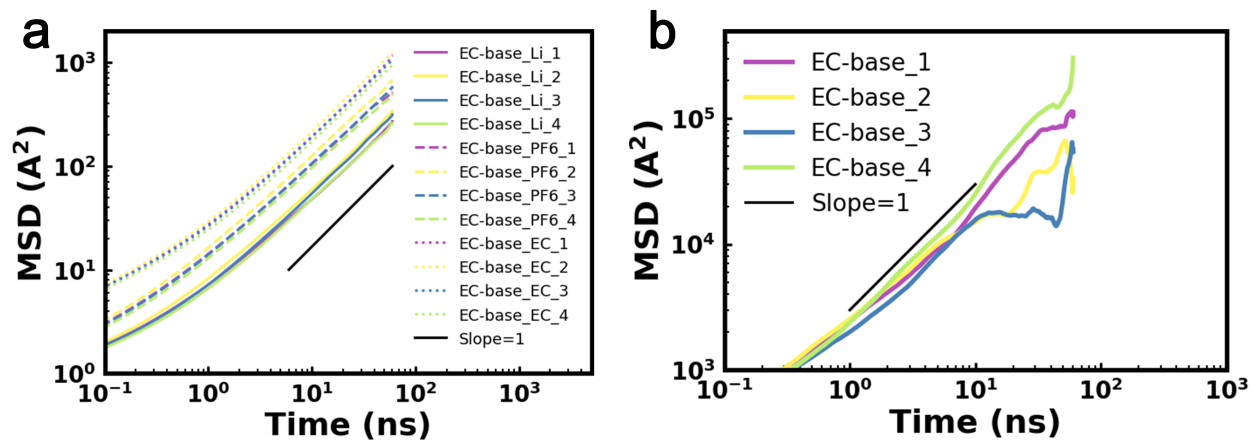## The linear diffusion behavior

Figure B.3 The linear diffusion behavior of four duplicate runs of the EC-base electrolyte required to calculate (a) self-diffusion coefficients, and (b) ionic conductivity. A slope of one (corresponding to linear data on a log-log plot) is indicated on each plot. The effective "mean square displacement" on the y-axis of panel (b) is the quantity in angular brackets in equation 2.25.
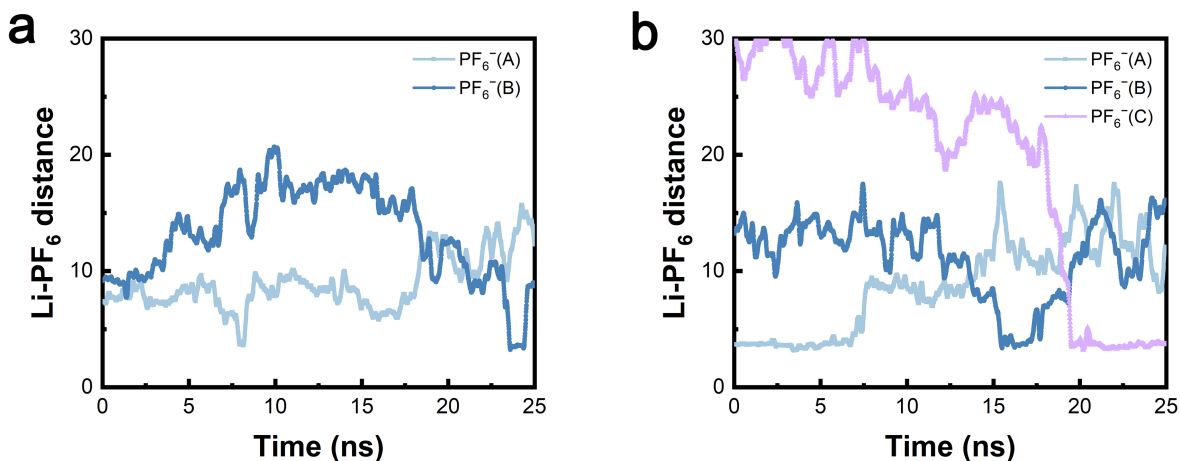
Sample trajectories

Figure B.4 Sample trajectory of Li-PF$_6$ coordination distance as a function of time in (a) EC-base electrolyte, and (b) Gen2 electrolyte. A cutoff distance of 5 Å is used to differentiate CIP and SSIP.

Figure B.4 presents the Li-PF$_6$ coordination distance as a function of time in the EC-base and Gen2 electrolyte. The two sets of trajectories are sampled from one Li$^+$ over a long period (25 ns) of MD simulations. The Li$^+$-PF$_6^-$ pair in the Gen2 electrolyte coordinates with each other for a longer period of time.

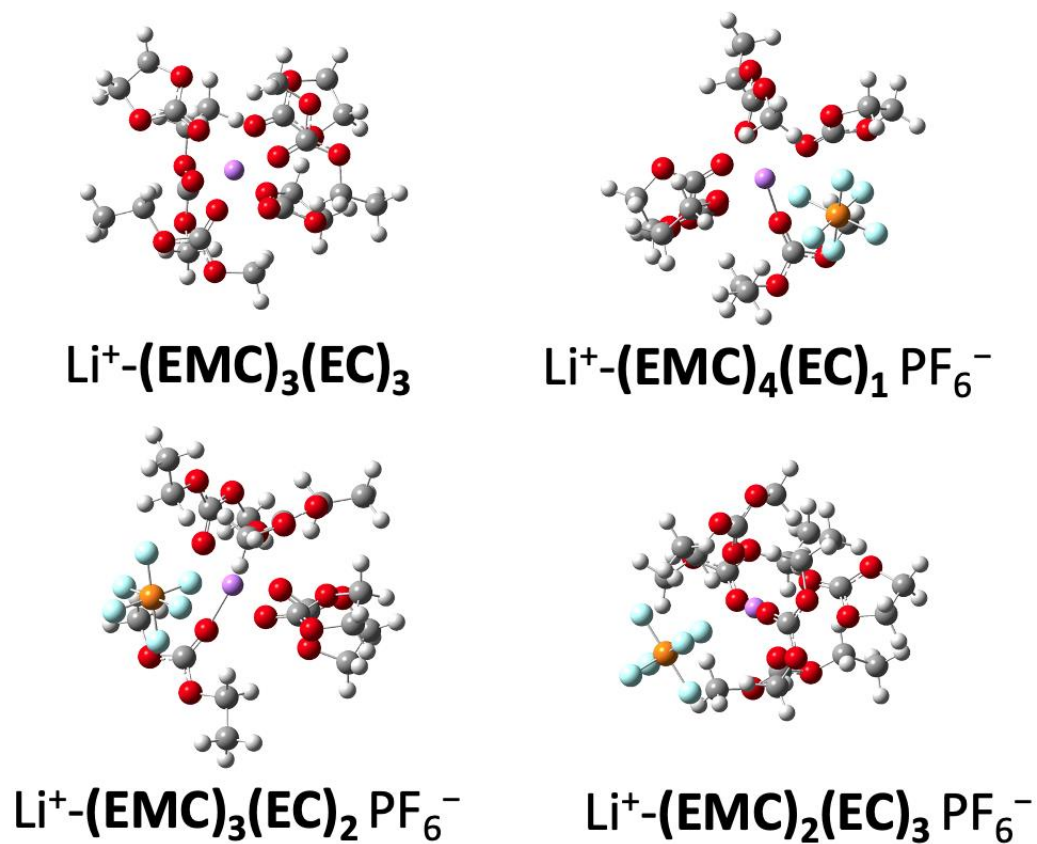## Optimized solvation structures

Figure B.5 The optimized structures for calculating the anion–solvent exchange free energy. The red, grey, white, cyan, orange, and purple balls denote oxygen, carbon, hydrogen, fluorine, phosphorus, and lithium, respectively.
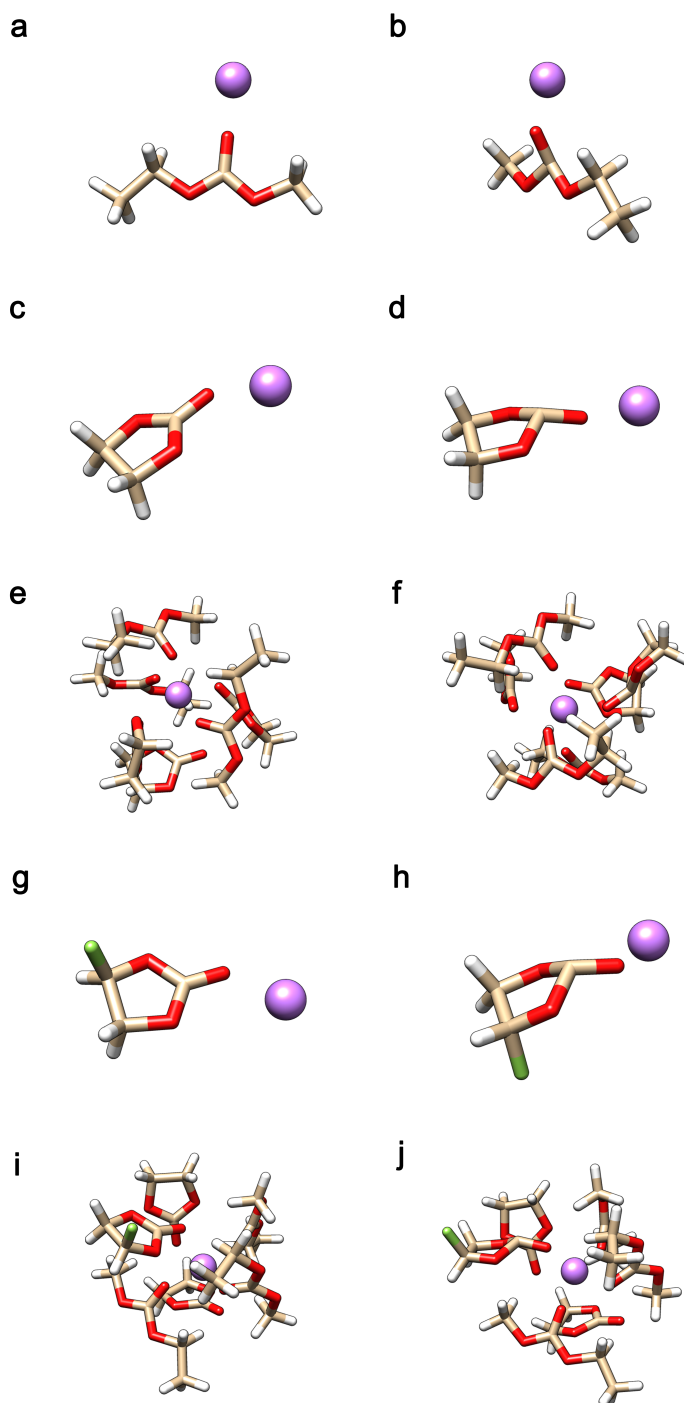
Figure B.6 Optimized geometries before and after reduction of (a-b) Li^+–EMC, (c-d) Li^+–EC, (e-f) Li^+–$(EC)_3(EMC)_3$, (g-h) Li^+–FEC, and (i-j) Li^+–$(EC)_2(EMC)_3(FEC)$. The red, cream, white, green, and purple colors denote oxygen, carbon, hydrogen, fluorine, and lithium, respectively.
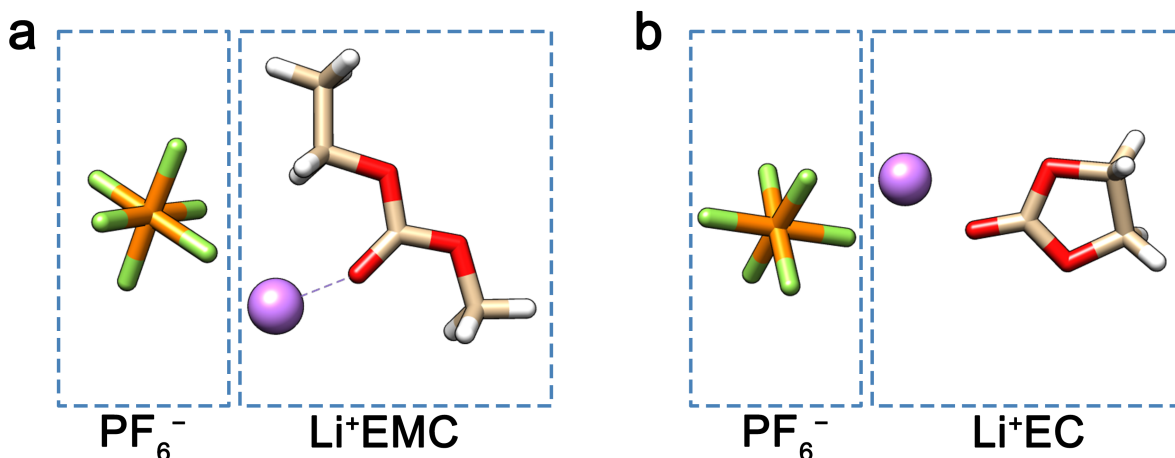
Binding energy decomposition

Figure B.7 Two groups of clusters (a) $[Li^+EC]\ldots PF_6^-$ (E_{b1}), and (b) $[Li^+EMC]\ldots[PF_6^-]$ (E_{b2}), for the binding energy decomposition using ALMO-EDA(solv). The red, cream, white, green, orange, and purple colors denote oxygen, carbon, hydrogen, fluorine, phosphorus, and lithium, respectively.

The ALMO-EDA(solv) was performed on the binding energy of $[Li^+EC]\ldots PF_6^-$ (E_{b1}) and $[Li^+EMC]\ldots[PF_6^-]$ (E_{b2}), respectively (ellipsis denotes the binding of two clusters), as shown in Figure B.7, B.8. The electrostatic energy dominates the attractive terms in both E_{b1} and E_{b2}, which is consistent with the fact that ion coordination is governed by the electrostatic interaction. The difference between E_{b1} and E_{b2} ($\Delta E_b = E_{b2} - E_{b1}$) is computed to be -10.7 kJ mol^{-1}, which agrees well with the difference in the anion–solvent exchange free energy as shown in the main text, Table 4.1. We note that the electrostatic energy contributes 63% of the attractive terms in ΔE_b, providing a direct measurement of the energy difference of the electrostatic characterizations of EC and EMC.
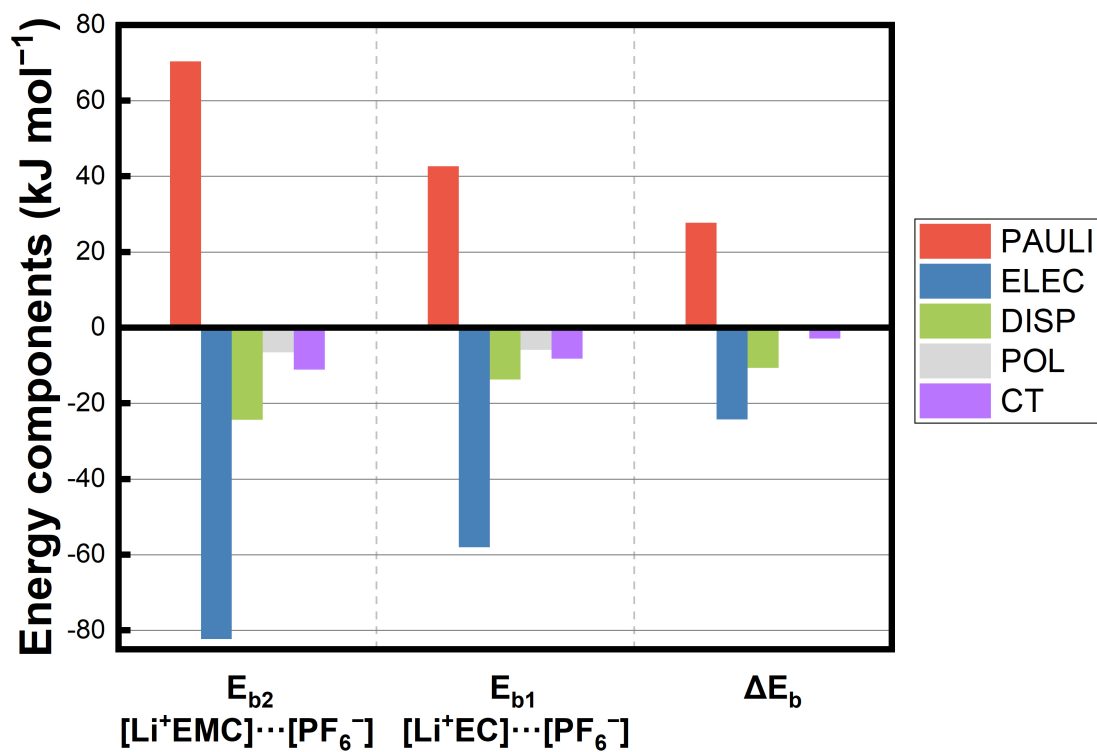
Figure B.8 The binding energy decomposition analysis (EDA) of $[Li^+EC]\ldots PF_6^-$ (E_{b1}), $[Li^+EMC]\ldots[PF_6^-]$ (E_{b2}) and their difference into contributions from permanent electrostatics (ELEC), Pauli repulsion (PAULI), dispersion (DISP), polarization (POL), and charge transfer (CT).

Experimental measurements raw data

Table B.3 The amount of the salt and solvents used for preparing the four electrolytes for ionic conductivity measurement.

Electrolyte	LiPF$_6$ mass	EC mass	EMC volume	FEC volume
EC-base	2 g	13.80 g	-	-
ECF	2 g	12.42 g	-	1.14 ml
Gen2	2 g	3.52 g	8.17 ml	-
GenF	2 g	3.17 g	7.40 ml	0.87 ml

Table B.4 Measured ionic conductivities at room temperature and corresponding corrected values at 25 ˚C.

Electrolyte	Measurement 1 (mS cm^{-1})	Measurement 2 (mS cm^{-1})	Corrected value at 25 ˚C (mS cm^{-1})
EC-base	9.964 (34.7 ˚C)	9.539 (30.8 ˚C)	8.91
ECF	8.847 (31.7 ˚C)	8.703 (29.8 ˚C)	8.33
Gen2	10.62 (33.3 ˚C)	10.38 (30.9 ˚C)	9.79
GenF	10.75 (32.3 ˚C)	10.55 (29.9 ˚C)	10.14

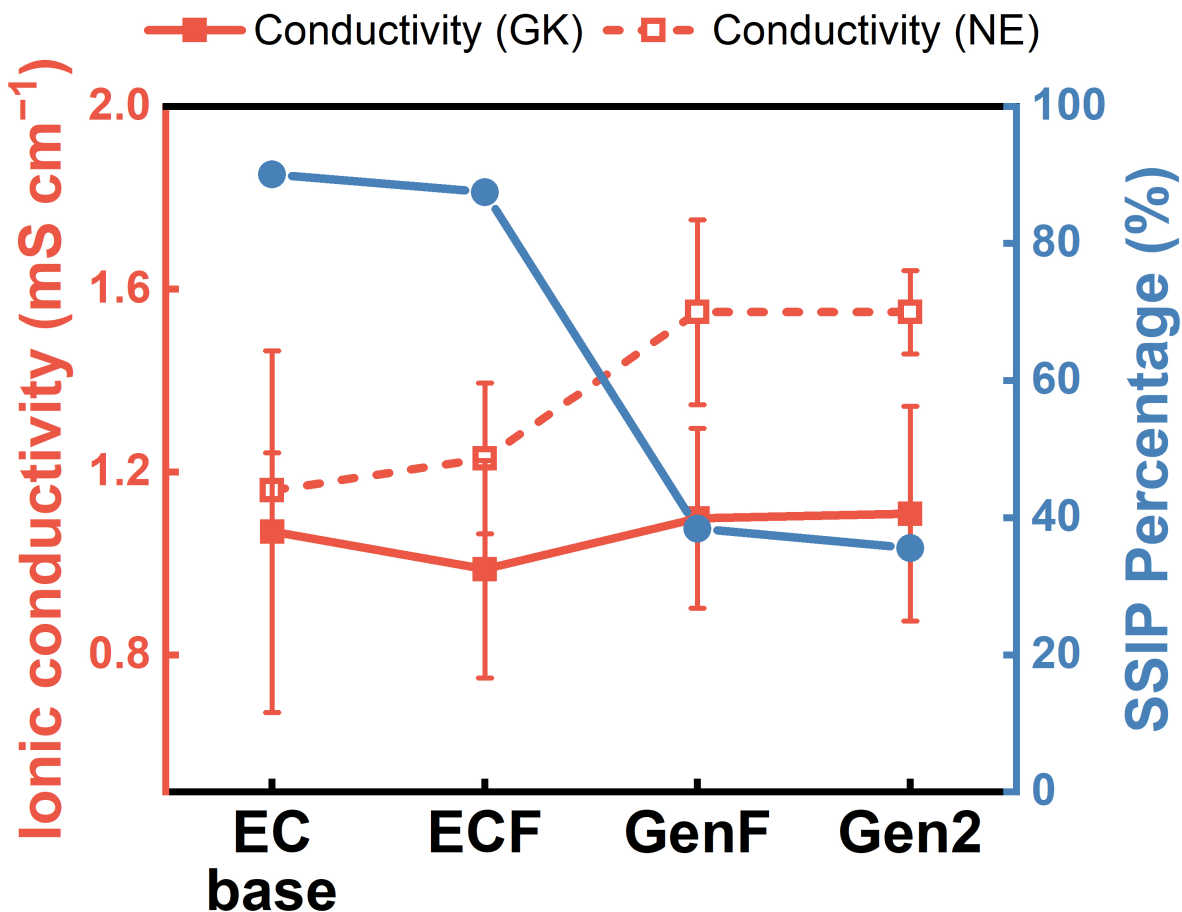## Ionic conductivity calculation using the conventional method

Figure B.9 The calculated ionic conductivities of the EC-base, ECF, Gen2, and GenF electrolytes using Green–Kubo relations (GK) and Nernst–Einstein equation (NE), and the corresponding ratios of solvent separated ion pair (SSIP).

The conventional approach is to assume that the anions and cations are mostly dissociated in the electrolyte, and therefore, the conductivity can be calculated using the Nernst–Einstein equation (NE) from the diffusivity of Li^+:

$$\sigma_{NE} = \frac{F^2}{RT}(c_+ z_+^2 D_+ + c_- z_-^2 D_-), \tag{B.1}$$

where σ_{NE} is the ionic conductivity, F is the Faraday constant, R is the gas constant, T is temperature, c_+ and c_- are the bulk molar concentrations of the cation and anion, z_+ and z_- are the charge of the cation and anion, and D_+ and D_- are the self-diffusivities of the cation and anion. Here, we compare the conductivity calculated using Green–Kubo

relations (σ_{GK}, used in this work) and Nernst–Einstein equation (σ_{NE}, conventional) of the four electrolyte systems. The electrolytes are in the descending order of the corresponding percentage of solvent separated ion pair (SSIP), which reflects the degree of salt dissociation in the electrolytes. As the SSIP percentage decreases, the deviation between σ_{NE} and σ_{GK} becomes larger. For the EC-base electrolyte, where most cations are dissociated with anions to form SSIP, σ_{NE} is only 9% higher than σ_{GK}. In contrast, in the Gen2 electrolyte, where only 35.6% of Li^+ ions are fully dissociated, σ_{NE} overestimates the conductivity by more than 40%. This observation indicates that for highly associated mixed carbonate electrolytes, a rigorous calculation using Green–Kubo relations is important for obtaining a correct trend of the ionic conductivity.

Validation of the force field

To further validate the OPLS-AA force field for the specific systems that we investigated in our MD simulations. Here, using the EC solvent as an example, we benchmarked the force field parameters against two key properties, the enthalpy of vaporization and the zero-frequency permittivity, which are both experimentally available. The enthalpy of vaporization can be calculated by

$$\Delta H_{vap} = \Delta H_{gas} - \Delta H_{liquid} = E_{total}^{gas} - E_{total}^{liquid} + RT \tag{B.2}$$

where, E_{total}^{liquid} is the total potential energy or internal energy of the liquid. It was obtained from NPT simulation of the bulk liquid. An average pressure of 1 bar was applied. E_{total}^{gas} is the internal energy of the gas phase. E_{total}^{gas} was obtained by doing NVT simulation of single molecule in vacuum. PV-work term was calculated using the RT term by assuming noninteracting ideal state for the gas phase. A value of 62.39 kJ mol^{-1} (313 K) for enthalpy of vaporization was obtained using simulations, which is close to the experimental value of 60.3 kJ mol^{-1} (383 K). The zero-frequency permittivity can be calculated via the fluctuation dissipation theorem (FDT) according to the following relationship

$$\epsilon_r = 1 + \frac{\langle M^2 \rangle - \langle M \rangle^2}{3VT\epsilon_0 k_B} \tag{B.3}$$

where M is the dipole moment of the system and ϵ_0 is the permittivity of free space. A value of ϵ_0 88.1 (313 K) was obtained for EC, which agrees well with the experimental value of 89.8 (298 K).

Therefore, we have shown that the OPLS-AA force field utilized in this work can effectively reproduce the key experimental properties of the bulk solvents.

The validity of the force field is further assessed by comparing the electrostatic potential contour maps of EC and EMC obtained from quantum chemistry and the fitted RESP charges. Using the fitted RESP charges, the electrostatic potential at point i can be calculated by:

$$V_i = \sum_j \frac{kq_j}{\varepsilon r_{ij}} \tag{B.4}$$

where Vi is the electrostatic potential at point i, qj is the partial charge of each atom in the molecule, k is the Coulomb constant, rij is the distance between point i and atom j, ϵ is the dielectric constant of the electrolyte where a value of 20.493 is used to match the quantum chemical calculation.

Comparing Figure B.10 with main text Figure 4.3a, b, the electrostatic potential calculated from the quantum chemistry and partial charges of the MD force field are almost identical. This observation illustrates that our fitted RESP partial charges can effectively reproduce the actual electrostatic potential as obtained from quantum chemistry. In addition, the result further validates the OPLS-AA force field utilized in our MD simulation.
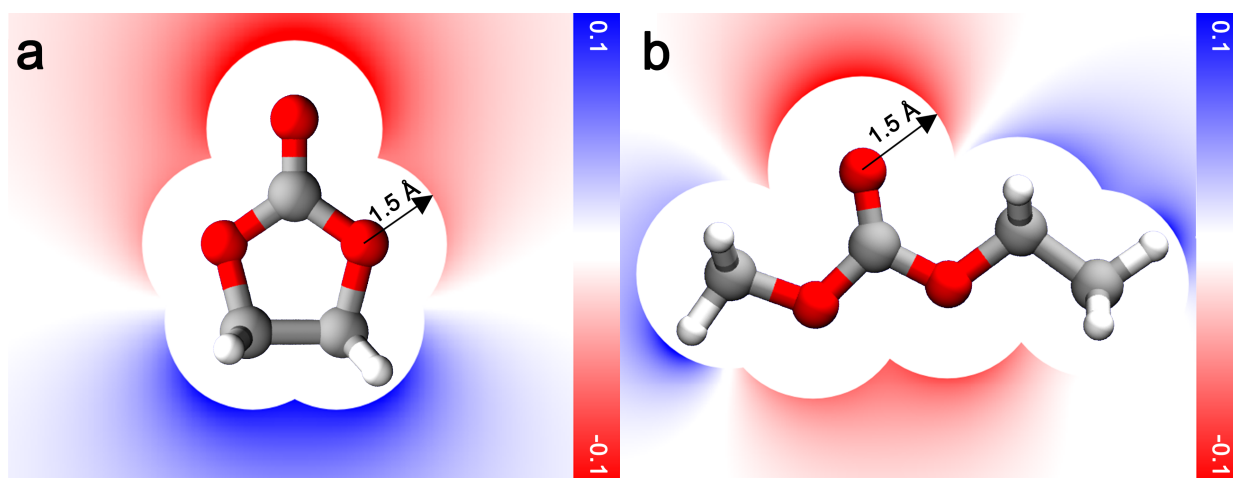
Figure B.10 The electrostatic potential contour maps of (a) EC, (b) EMC calculated from the fitted RESP charges in the chosen molecular dynamics force field. The electrostatic potential is truncated with a cutoff distance of 1.5 Å to avoid infinite potential values at point charge centers. The slice is across the carbonyl plane. Red, blue, and white colors represent the least positive (or most negative), most positive and intermediate electrostatic potential, respectively. The color bar shows the values of the electrostatic potential in volts. The connections between atoms represent chemical bonding or Li^+ coordination.

Appendix C

Supplementary Materials for The Modeling of Novel Solid-State Electrolytes Based on Metal–Organic Frameworks
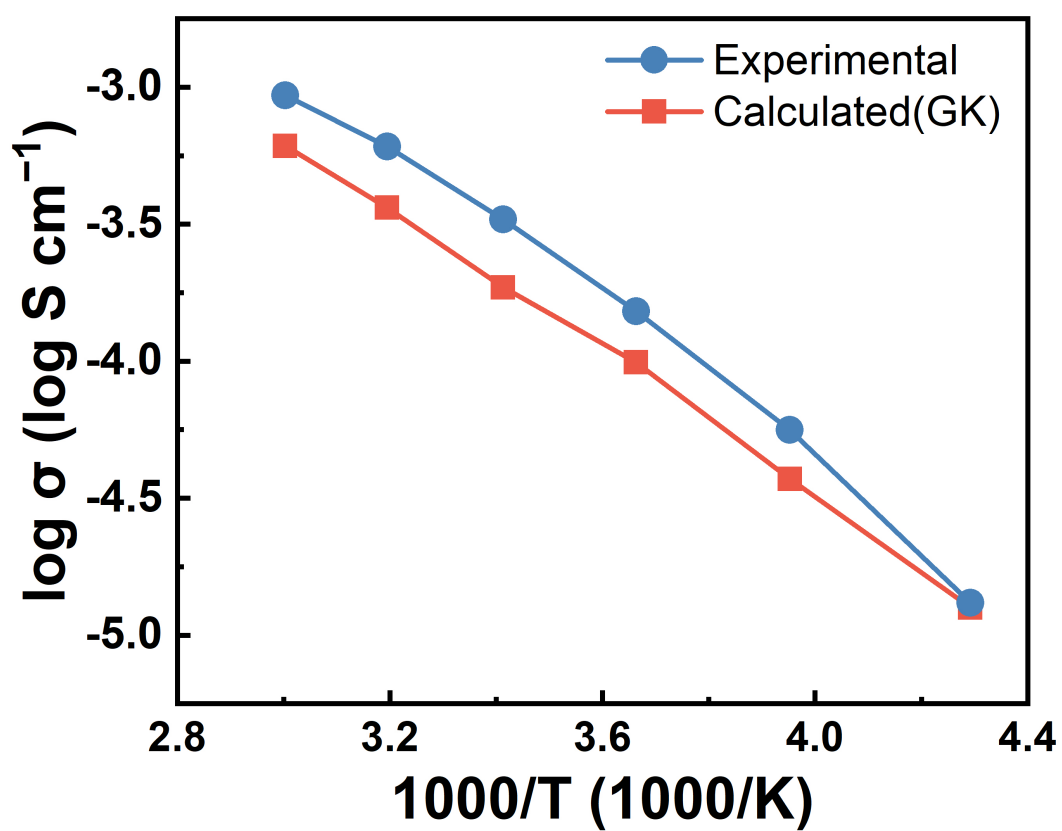
Figure C.1 Experimental and calculated ionic conductivity as a function of temperature from −40 to 60 °C at 10 °C intervals.
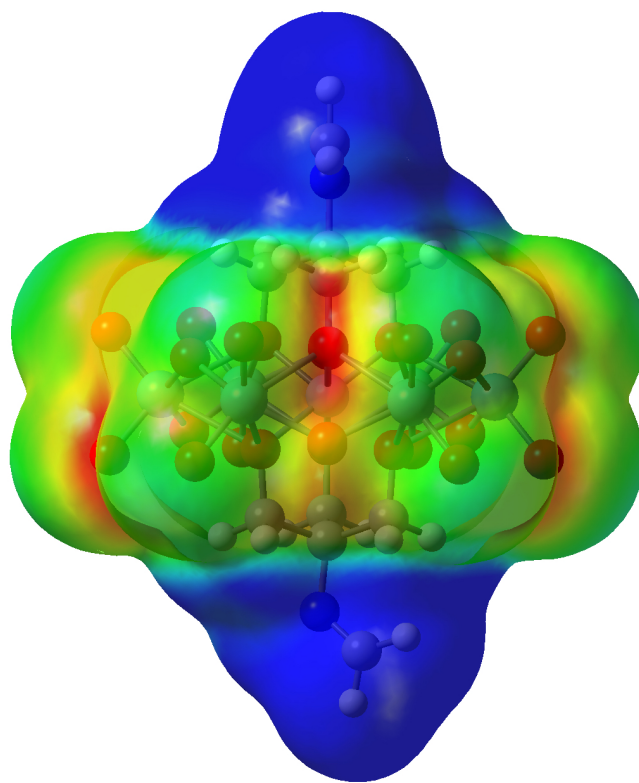
Figure C.2 Front view of the electrostatic potential (ESP) surface of the MOF-688(Al) POM cluster. The color bar is the same as the main text Figure 5.3.
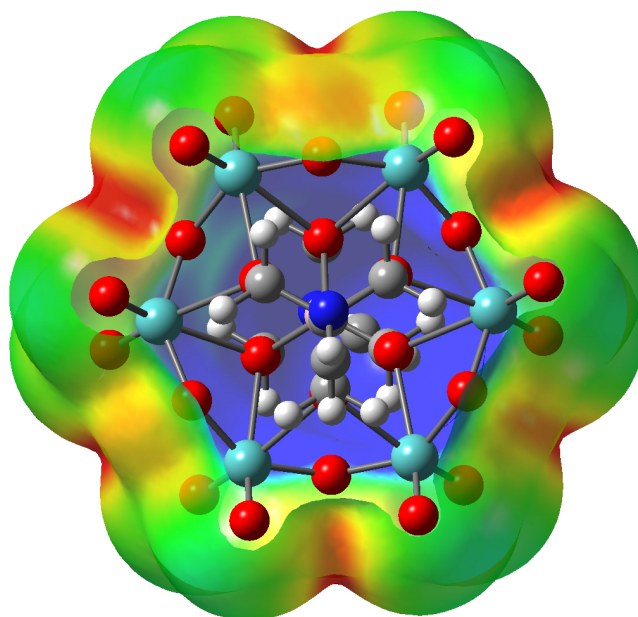
Figure C.3 Top view of the electrostatic potential (ESP) surface of the MOF-688(Al) POM cluster. The color bar is the same as the main text Figure 5.3.